The Antares Neutrino Telescope:

Performance Studies and Analysis of First Data

ISBN 978-90-6488-029-2

The Antares Neutrino Telescope:

Performance Studies and Analysis of First Data

ACADEMISCH PROEFSCHRIFT

TER VERKRIJGING VAN DE GRAAD VAN DOCTOR
AAN DE UNIVERSITEIT VAN AMSTERDAM
OP GEZAG VAN DE RECTOR MAGNIFICUS
PROF. DR. D. C. VAN DEN BOOM
TEN OVERSTAAN VAN EEN DOOR HET COLLEGE VOOR PROMOTIES
INGESTELDE COMMISSIE, IN HET OPENBAAR TE VERDEDIGEN
IN DE AGNIETENKAPEL
OP WOENSDAG 19 MAART 2008, TE 12:00 UUR

door

Ronald Bruijn

geboren te Zaandam

Promotores: Prof. Dr. P.M. Kooijman
Prof. Dr. M. de Jong

Faculteit der Natuurwetenschappen, Wiskunde en Informatica

Voor mijn ouders

Contents

Introduction

Antares [1], BAIKAL [2], AMANDA [3] and ICECUBE [4] are experiments in the emerging field of *neutrino astronomy*. Neutrino astronomy, as part of a larger discipline called *astroparticle physics*, complements the astronomy based on the observation of electro-magnetic radiation emitted by astrophysical sources.

The first part of the *Antares neutrino telescope* became operational on the 2^{nd} of March 2006. At the time of this writing 80 % of the detector is operational. The work described in this thesis is based on the data taken in 2006. The prospects of the complete detector will be presented as well.

The complementarity of neutrinos for observational astronomy stems from their properties. Neutrinos are neutral, weakly interacting particles. The small interaction cross section of neutrinos with matter prevents their absorption on the way to Earth. High-energy photons (gamma-rays) can be absorbed by interactions with the infra-red, microwave and radio background photons, which limits the depth of view. As neutrinos are neutral, they are not deflected by galactic or extra-galactic magnetic fields. Hence, they point straight back to their source, which is essential for astronomy.

The first and only direct observation of neutrinos with a cosmic origin is the detection of neutrinos from Supernova 1987a by the Kamiokande [5] and IMB [6] detectors. Detection of neutrinos from the Sun, the atmosphere, nuclear reactors and particle accelerators have led to a determination of the neutrino oscillation parameters. Oscillations of neutrinos occur between three flavor eigenstates, namely : electron-, muon-, and tau-neutrinos.

One of the main questions in astroparticle physics is the origin and nature of high-energy cosmic rays. It has long been known that energetic charged particles bombard the Earth and produce particle showers in the atmosphere. While the energy spectrum of the cosmic rays can be measured up to very high energies ($\sim 10^{20}$ eV), their origin remains unclear. Recently, the Pierre Auger collaboration reported a correlation between high-energy cosmic rays and active galactic nuclei [7]. As the cosmic rays are charged, they are deflected by the (extra-) galactic magnetic fields. In addition, protons with energies exceeding $\sim 10^{19}$ eV interact with the cosmic microwave background. This effect, known as the Greisen-Zatsepin-Kuzmin cutoff [8], limits the range of high energy protons to the order of 100 Mpc. Assuming that a fraction of the high-energy protons interact with the ambient matter or photon fields, pions and hence neutrinos will be

created. Potential sources of high-energy neutrinos include supernova remnants, active galactic nuclei, gamma-ray bursts and microquasars. Detection of neutrinos from such sources will shed light on the physical processes involved in their creation.

While the small interaction cross section of neutrinos allows them to come from far away, it is also a draw-back, as their detection requires a large target mass. The Antares collaboration is building a detector by instrumenting a large volume (0.05 km^3) of sea water. An array of 900 photo-multiplier tubes is being installed at the bottom of the Mediterranean Sea at a depth of about 2.5 kilometers. The photo-multiplier tubes are used to detect the light emitted by the products of an occasional neutrino interaction. The photo-multiplier tubes are mounted on 12 vertical strings, each having an instrumented length of about 350 m. On the 2^{nd} of March 2006, the first of these lines was connected via an electro-optical cable to the shore station, which is located in the town of La-Seyne-sur-Mer, France.

The detection of neutrinos is based on the detection of muons which are created in the charged-current interactions of muon-neutrinos. These muons, at sufficiently high-energies, retain information on the direction of the incident neutrino and can traverse several kilometers of sea water. Along their trajectory, the muons emit Cherenkov light. From the measured arrival time of the Cherenkov light, the direction of the muon can be determined. This process is referred to as muon track reconstruction. A new muon track reconstruction algorithm has been developed, which is described in this thesis. It is designed to have a minimal dependence on the models describing the processes leading to the detection of photons. This makes it especially suitable for the start of detector operations. It has been used to produce the first results of Antares. The algorithm has been extended by adding a final stage which is based on a detailed modelling of the arrival times of the photons from the muons. This allows the study of the final performance of the detector. This study is based on simulations.

The main background for the Antares detector comes from two sources. First, there is a flux of muons that originate from the interactions of cosmic rays in the Earths atmosphere. Despite the depth, some can reach the detector and cause a detectable signal. These muons must be distinguished from the neutrino induced muons. Second, the decay of radioactive ^{40}K and the biological activity in the sea water cause a significant rate in each photo-multiplier tube. Various ways to reduce these backgrounds have been developed. The performance of the complete detector in the presence of these backgrounds has been studied.

Outline

This thesis is organized in the following way.

In chapter 1 a brief overview of the field of neutrino astronomy is given. Sev-

eral potential neutrino sources are presented.

In chapter 2 the detection principle of the Antares neutrino telescope is explained, followed by a description of the design of the detector, its data acquisition and calibration systems. In addition, an overview of the various backgrounds is given. Finally, the software tools which are used to simulate the processes that lead to a detectable signal and the response of the detector are presented.

In chapter 3, a new method to determine the direction of the muon track is described. The performance of this method is evaluated for different background conditions.

In chapter 4 the results of the analysis of the data of the first detector line of the Antares telescope are presented. A simulation is used to estimate the detector efficiency. The effects on the muon reconstruction due to the presence of electromagnetic showers along the tracks will be discussed. The precision with which the zenith angle of muon tracks can be determined is quantified using data. The dependence of the atmospheric muon flux on the depth has been determined.

In chapter 5, the performance of the complete detector is evaluated for various background conditions. The detection efficiency and the pointing accuracy of the Antares detector are determined.

Chapter 6 contains a summary and conclusion.

Chapter 1

High-energy neutrino astronomy

High-energy neutrino astronomy is largely motivated by the observation of very high-energy particles and photons from the cosmos. The charged particles are deflected by the galactic and extra-galactic magnetic fields. As a consequence, the measured directions of particles are no longer correlated with their origin. Interactions of high-energy photons and protons with background photons limit the distances they can travel through space and thus introduce an observational horizon. Neutrinos can be created through interactions of high-energy protons inside or in the vicinity of the astrophysical source. As neutrinos are neutral and interact only weakly with matter, they offer a possibility to study these sources.

In this chapter, a brief overview of the field of neutrino astronomy is given, along with an introduction of potential neutrino sources. For more detailed discussions, the reader is referred to [9] and [10].

1.1 Neutral particles

In contrast to charged particles, neutral particles are not deflected by galactic and extra-galactic magnetic fields. This makes neutral particles excellent probes for distant objects as they will point back to their source. In case of photons, this feature has been used for a long time in optical, and more recently, in X-Ray and γ ray astronomy.

The neutrino production process which is relevant in the context of cosmic accelerators is based on pion (π) production and decay. The main decay mode ($> 99.98\%$) of charged pions leads to muons (μ) and muon neutrinos (ν_μ).

$$\pi^+ \rightarrow \mu^+ + \nu_\mu \tag{1.1}$$

$$\pi^- \rightarrow \mu^- + \bar{\nu}_\mu \tag{1.2}$$

where the $\bar{\nu}$ denotes the anti-neutrino. The muon decays to an electron (e), a muon- and an electron-neutrino with almost 100 % probability.

$$\mu^+ \rightarrow e^+ + \bar{\nu}_\mu + \nu_e \tag{1.3}$$

$$\mu^- \rightarrow e^- + \nu_\mu + \bar{\nu}_e \tag{1.4}$$

Pions can be created through inelastic collisions of high-energy protons (or nuclei) with ambient matter

$$p + p \rightarrow \pi^\pm + X \tag{1.5}$$

$$p + p \rightarrow \pi^0 + X \tag{1.6}$$

The neutral pion (π^0) decays with approximately 100 % probability to two photons

$$\pi^0 \rightarrow \gamma + \gamma \tag{1.7}$$

For astrophysical objects which are surrounded by a dense photon gas, pions can also be produced by

$$p + \gamma \rightarrow \pi^\pm + X \tag{1.8}$$

$$p + \gamma \rightarrow \pi^0 + X \tag{1.9}$$

In summary, neutrinos can be produced hadronically. Photons, however, can also be produced electro-magnetically. Electrons and positrons can produce photons either by synchrotron radiation or inverse Compton scattering.

1.2 Observations

1.2.1 Cosmic Rays

Almost a century ago, Victor Hess (1883-1964) performed experiments with electrometers suspended in balloons. His studies of ionising radiation at different altitudes led to the conclusion that these 'cosmic rays' must have an extra-terrestrial origin. Since then, the phenomenon has been studied by a broad range of different instruments. The list of instruments includes satellite detectors and very large air shower arrays. Although the phenomenon has been known for almost 100 years, the origin of these particles remains unclear. A known feature of cosmic rays is the large observed range of energies. This is shown in figure 1.1. It can be seen from figure 1.1 that the flux of particles depends on the energy. Above 10 GeV, the cosmic ray flux as function of energy can be roughly described by a power law formula

$$dN/dE \propto E^{-\gamma} \tag{1.10}$$

were N is the number of observed events, E the energy of the primary particle and γ is the spectral index. The spectral index is about 2.7. Above 10^{15} eV, the spectral index steepens to about 3.1, introducing a feature called the 'knee'. At even higher energies, around 10^{19} eV, the spectrum shows a feature called the 'ankle'. At lower energies (< 200 GeV) which are accessible to direct measurements

by mass spectrometers, the composition is dominated by hydrogen and helium nuclei. It has been suggested that beyond the knee, the composition changes from protons to heavier elements [11]. The 'knee' and a composition change can be explained by a cut-off energy in the generation of cosmic rays which depends on charge or mass [12]. Protons with energies exceeding 10^{18} eV have a gyroradius larger than the thickness of the Galactic disc [13]. These particles are thus not confined to the Galactic disc. Above about 10^{19} eV, the range of protons and nuclei is limited by interactions with the cosmic microwave background [8]. This is known as the Greizen-Zatsepin-Kuzmin (GZK) cut-off. The interaction lengths of protons at these energies are shown in figure 1.2.

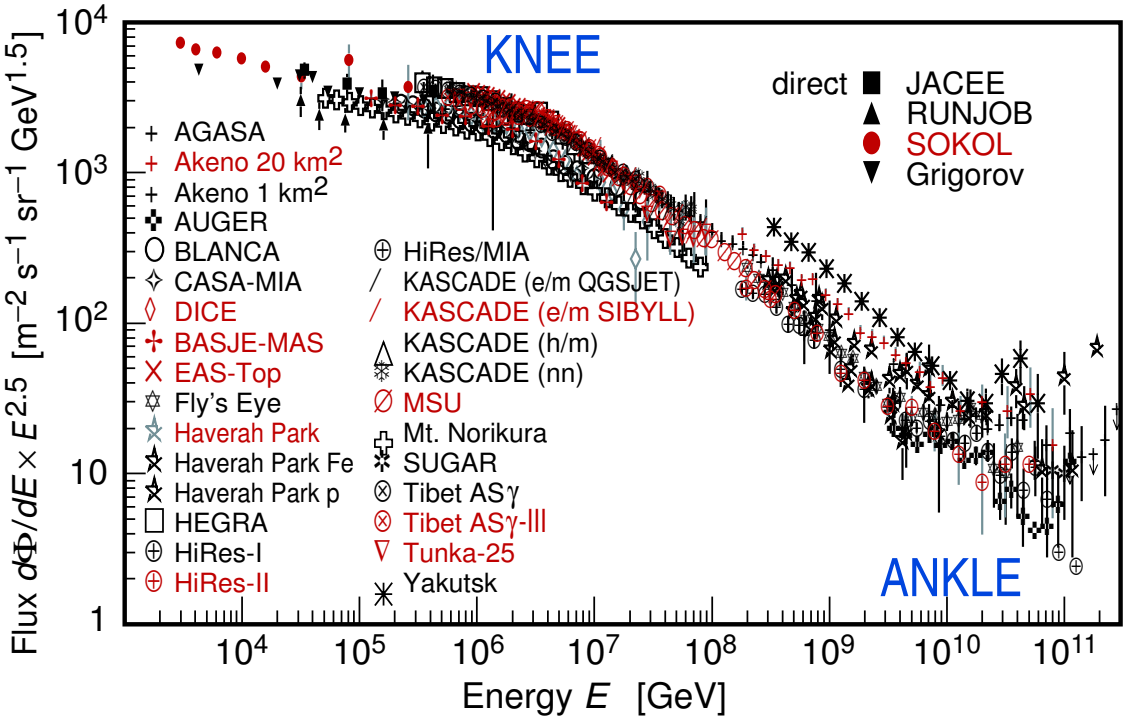

Figure 1.1: *The all-particle cosmic ray spectrum. Figure taken from [14].*

The existence of high-energy cosmic-rays suggests a possible source of high-energy neutrinos through pion-production. A likely acceleration mechanism for charged particles is the so-called *shock acceleration* (see for example [15]). Shock acceleration can occur at the boundary of two colliding plasmas. The shock acceleration predicts a spectrum with a power-law dependence and a typical exponent of about -2, in reasonable agreement with the observed energy spectrum of cosmic rays.

1.2.2 Gamma rays

The observations of high-energy gamma-rays started in the 1960's. At that time, it became possible to operate detectors outside the Earth's atmosphere aboard satellites. This allowed the detection of gamma-rays (MeV photons) which are not observable from the ground, as they are absorbed in the atmosphere. The EGRET instrument on board the Compton Gamma-Ray Observatory satellite was used to produce a sky map containing 271 sources of MeV gamma-rays (see figure 1.3). Higher-energy gamma-rays ($\sim$TeV) can be observed by ground based instruments which detect the cascades initiated by the energetic gamma-rays interacting with the atmosphere. However, high-energy gamma rays interact with the infra-red, microwave and radio background photons. As a consequence, the distance which high-energy gamma rays can travel through the Universe is limited. This effect is illustrated in figure 1.2.

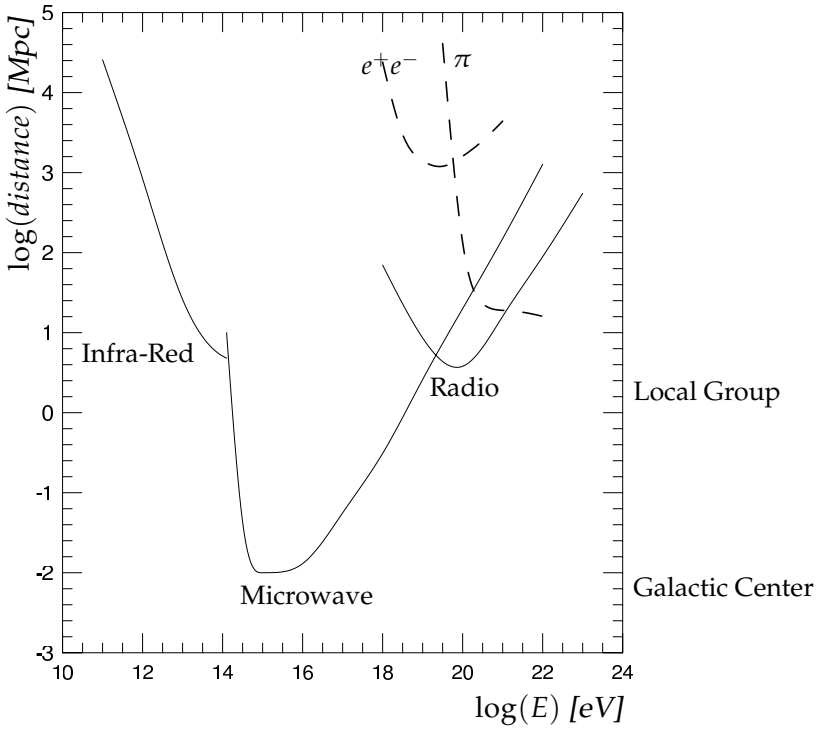

Figure 1.2: *Interaction lengths for high-energy photons (solid lines) and protons (dashed lines) with background photons as function of energy. Figure adapted from [16].*

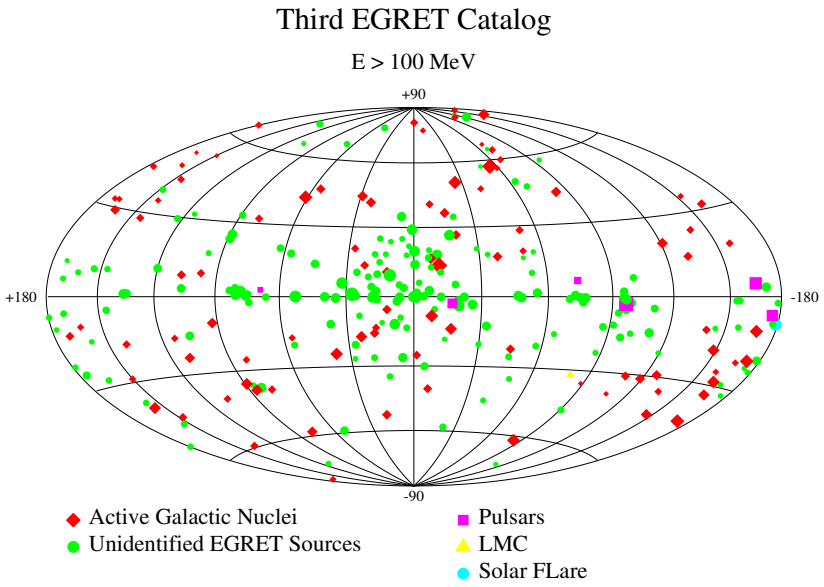

Figure 1.3: *The third EGRET catalog, showing sources of gamma rays with energies from 100 MeV to 30 GeV [17] in Galactic coordinates.*

1.3 Neutrino sources

In this section, some potential astrophysical sources of high energy neutrinos are discussed. The subject of neutrinos created by cosmic ray interactions in the atmosphere, will be covered in the following chapter.

The matter and photons in the interstellar space can be a target for the cosmic rays. Cosmic rays interacting with matter in the Galactic disc are a source of diffuse gamma-rays. These interactions can also produce neutrinos [18]. Very high-energy cosmic rays can also interact with background photons (microwave, infra-red, optical and ultra-violet). This can lead to a diffuse flux of so-called cosmogenic neutrinos [19].

Several potential neutrino sources are of interest. These include relativistic jets. Such a jet could provide an acceleration mechanism for protons through shock acceleration (either internal or external shocks). An observed high-energy gamma-ray flux could be an indication of hadronic interactions based on the assumption of neutral pion decay. Consequently, one expects neutrinos from the associated charged pion decays.

Supernova remnants A supernova is a luminous explosion due to the core collapse of a massive star. As a result an expanding shock wave consisting of ejected as well as swept up interstellar matter is created that envelopes the supernova remnant. At this shock wave, particle acceleration can occur. Supernova remnants within our Galaxy are believed to be responsible for the

bulk of the cosmic rays below 1 PeV [20].

Recently, observations of TeV gamma-rays from a supernova remnant were found to favor π^0 decay as the main source of photon production [21],[22].

Active Galactic nuclei Active Galactic nuclei (AGN) are the brightest sources in the Universe. In the standard model of AGN, a very massive black hole ($10^6 - 10^{10}$ solar masses) accretes matter (several solar masses a year). Typically, two jets are observed, emerging at opposite sides of the accretion disc. In these jets, particles can be accelerated. These particle beams can interact with the ambient matter and photons. An AGN appears especially bright when one of the jets is oriented along our line of sight.

Very recently, the Pierre Auger Observatory found a correlation between the arrival directions of cosmic rays with energies above $6 \cdot 10^{19}$ eV and the positions of nearby AGN [7]. They found that out of 15 events with an energy above 60 EeV, 12 were located within 3.1° of AGN at distances less than 75 Mpc from Earth. The hypothesis of an isotropic distribution of these cosmic rays can be rejected with at least 99 % confidence level. This result suggests AGN are potential neutrino sources.

Gamma-ray bursts Gamma-ray bursts (GRBs) are very bright flashes of MeV gamma-rays, with durations varying from less than a second to a few hundred seconds. Various models are proposed. A subset of the GRBs, the 'long' bursts, are believed to be associated with the collapse of massive stars, or supernovae [23].

The observed signal is believed to be caused by a collimated relativistic jet with a high Lorentz factor containing photons, electrons, positrons and baryons. External and internal shocks provide a mechanism for acceleration of charged particles [24],[25].

Microquasars Microquasars are binary systems composed of an accreting massive object such as a black hole or neutron star and a companion star. They display relativistic radio-emitting jets, probably fed by the accretion of matter from the companion star. Microquasars resemble AGN, but at a much smaller scale. Recently, TeV gamma-rays were observed from two microquasars [26],[27] for which an hadronic interpretation of the observations has been published [28],[29].

Pulsar wind nebulae A pulsar wind nebula (PWN) is a nebula believed to be powered by a relativistic wind of particles and magnetic fields from a pulsar. They are often associated with very young supernova remnants. Gamma-rays with TeV energies have been measured from several PWN such as the Crab Nebula and Vela X. Gamma-ray fluxes are usually interpreted as being caused by leptonic acceleration, but hadronic interpretations also exist [30].

The association of a high-energy neutrino point source (or the exclusion of it), to the list of candidates, would be of great scientific benefit. It would allow a better understanding of the mechanism at work in these sources.

In contrast to the scenario of accelerated particles which interact causing neutrinos, there exist 'top-down' theories of neutrino production. In these scenarios, neutrinos are produced as a result of the decay or annihilation of massive particles. A large fraction of the matter content of the Universe is known to be non-luminous (see [14] for a review). A possible explanation is that this 'dark-matter' consists of so-called WIMPS (weakly interacting massive particles). Neutralinos, the lightest super-symmetric particles, are candidates for these WIMPS. Neutralinos can accumulate in massive objects such as the Sun and annihilate, with neutrinos as the only decay products that can escape. These neutrinos could be detected by the Antares detector also [31].

Chapter 2

The Antares neutrino telescope

Neutrino astronomy is dictated by the small interaction cross section of neutrinos and the expected fluxes. On the one hand, the weakly interacting nature of neutrinos makes them excellent probes of distant astrophysical processes. As they are not deflected by magnetic fields they point straight back to their origin, while they have a low probability of being absorbed on their way to Earth. On the other hand, their small interaction probability combined with the expected fluxes require the use of very large detectors and long operation times. To enable the building of a large volume detector, naturally abundant sea-water can be used to detect the luminous interaction products of neutrinos. The neutrino telescope, which is under construction by the Antares collaboration, is based on this principle. In this chapter the Antares neutrino telescope will be presented. The software that is used to simulate both the physics processes that lead to a detectable signal and the detector response to this signal will be described.

2.1 Neutrino interactions

For a neutrino to be detected, it has to produce a detectable signal. Neutrinos interact with matter through the weak force which can be classified in two types. These are the neutral current (NC) interaction, which involves the exchange of a Z boson, or the charged current (CC) interaction, which involves the exchange of a W^+ or W^- boson [32]. These two interaction types can be formulated as

$$\nu_l(\bar{\nu}_l) + N \rightarrow \nu_l(\bar{\nu}_l) + X \ (NC) \tag{2.1}$$

$$\nu_l(\bar{\nu}_l) + N \rightarrow l^-(l^+) + X \ (CC) \tag{2.2}$$

Where $\nu_l(\bar{\nu}_l)$ is the (anti-)neutrino of type l, N the target nucleon, X the hadronic interaction products and l the lepton. At the energies considered in this work, the interaction cross section is predominantly inelastic. The involved lepton flavor can be one of the three types: electron (e), muon (μ) or tau (τ). The cross sections of the charged-current interactions involving muon (anti-) neutrinos are

shown in figure 2.1 as function of neutrino energy. The small values of the cross sections motivate the need for a large interaction volume. The charged particles originating from a neutrino interaction can produce a detectable signal (see section 2.4).

2.2 Detection principle

The Antares neutrino telescope consists of a three-dimensional array of light-sensitive photo-multiplier tubes (PMTs) installed at a large depth in the Mediterranean sea. This array of PMTs can detect photons produced by relativistic charged particles emerging from neutrino interactions in the sea-water or in the rock below the detector.

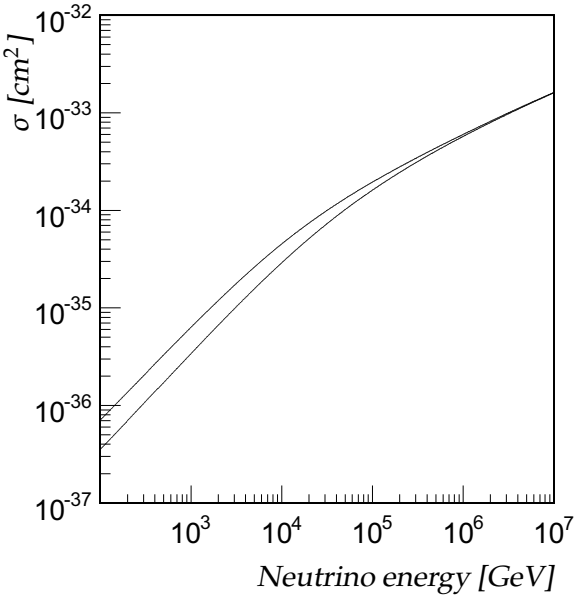

Figure 2.1: *Muon neutrino (top line) and anti-neutrino (bottom line) charged-current cross sections as function of energy, obtained using the CTEQ6D [33] quark density distributions.*

The main experimental signature for the Antares neutrino telescope is the signal produced by muons created in the charged-current interaction of muon-neutrinos. A relativistic muon propagating through the sea water emits Cherenkov light (section 2.4) that can be detected by the PMTs. The muons can travel large distances. In water, a 10 GeV muon can travel several tens of meters before it stops, while a 10^7 GeV muon can traverse some tens of kilometers [14]. The muon created in a muon-neutrino interaction retains the direction of the neutrino to a large extent. This can be expressed as the angle between the incident neutrino and the outgoing muon ($\theta_{\nu-\mu}$). The upper limit on this angle can be approximated by

$$\langle \theta_{\nu-\mu} \rangle \leq \frac{1.5^\circ}{\sqrt{E_\nu [TeV]}} \tag{2.3}$$

where E_ν is the neutrino energy. A muon traveling through rock or water is subject to multiple scattering. The deviation of the muon direction due to this

process (θ_{ms}) after traveling a distance x is given by [14] :

$$\theta_{ms} = \frac{13.6MeV}{E_\mu}\sqrt{x/X_0}\,[1 + 0.0038\ln(x/X_0)] \tag{2.4}$$

where X_0 is the radiation length of the medium. At the energies and distances considered in this work, θ_{ms} is smaller than $\theta_{\nu-\mu}$. The relation between the neutrino and muon directions is essential for the concept of a neutrino telescope. When the direction of the muon can be determined, so can the direction of the incident neutrino. As neutrinos are not deflected by (extra-)galactic magnetic fields, it is possible to trace the muon back to the origin of the neutrino. This is equivalent to optical astronomy where photons point back to their source. In this work, a technique is developed to derive the muon direction from the observed photons. This process is commonly referred to as muon track reconstruction.

2.3 Other signals

The momentum transferred to the hadronic products in the neutrino interaction is in general such that the charged particles also produce a detectable signal. While propagating through the sea water, they can interact with other nuclei and produce additional hadrons which in turn can produce a detectable signal and interact, thus forming a so-called hadronic shower. The decay of neutral pions introduces an electro-magnetic component to the shower. The hadronic cascades continue until all energy has been dissipated. For a nuclear interaction length of about 80 cm, the extension of such a shower in water is limited to several meters. Electrons produced in a charged-current interaction of an electron-neutrino radiate photons through Bremsstrahlung which in turn can be converted to electron-positron pairs. The electrons and positrons undergo Bremsstrahlung. The typical distance between interactions is given by the radiation length. The formed electro-magnetic cascades also have a limited size due to the limited radiation length of water of 36 cm. Therefore neutral-current neutrino interactions and charged-current electron-neutrino interactions should occur close to or within the detector volume to be detectable. When this happens, the detected light can be used to infer properties of the interacting neutrino [34]. The tau-lepton, which can be created in a charged-current interaction of a tau-neutrino, has a lifetime much shorter than that of the muon ($2.91 \cdot 10^{-13}$ seconds compared to $2.19 \cdot 10^{-6}$ seconds). In addition to the shower at the interaction point, a shower can occur when the tau decays. At sufficiently high energies, the tau-lepton can traverse a noticeable distance. Some fraction of the tau-lepton decays produce a muon (17.8%), which can mimic the interaction of a muon neutrino.

2.4 Cherenkov light

The detection of neutrinos happens indirectly through their interaction products. A charged particle traveling through a medium at a velocity exceeding the speed of light in the medium emits Cherenkov radiation [35]. This electro-magnetic radiation is emitted at a characteristic angle θ_c with respect to the direction of the charged particle, thus forming a conical light-front (figure 2.2). The angle θ_c can be expressed as

$$\cos(\theta_c) = 1/\beta n \tag{2.5}$$

where β is the ratio of the velocity of the particle (v) to the speed of light (c) and n is the index of refraction for the medium. At the location of the Antares neutrino telescope, the value of n is about 1.35 [36]. Thus, for relativistic particles ($\beta \approx 1$) the value of θ_c is about 42.2°. The number of Cherenkov photons emitted by a particle with unit charge (e.g. a muon) per unit wavelength ($\delta\lambda$) and per unit track length (δx) is given by

$$\frac{dN}{dxd\lambda} = 2\pi\alpha\frac{1}{\lambda^2}\left(1 - \frac{1}{\beta^2 n^2}\right) \tag{2.6}$$

where λ is the wavelength of the emitted photon and α the fine-structure constant. Considering the typical efficiency of a PMT (300 - 600 nm), the detectable photons emitted per meter number about 35000.

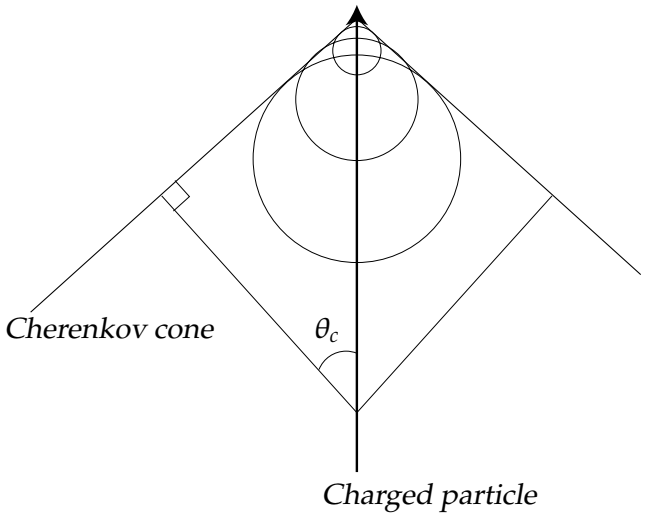

Figure 2.2: *Schematic view of the production of Cherenkov light by a charged particle. According to the principle of Huygens, spherical light waves are produced along the particle trajectory. The light waves interfere because the particle moves faster through the water than the light. As a result a sharp wave front is formed that can be detected with the PMTs.*

Photons traveling through the water are subject to several processes. They can be absorbed and scattered by molecules and particles in the water. Absorption of photons results in an attenuation of the intensity of the light emitted by a source

at a given distance. Scattering of photons affects the original angular distribution of the emitted photons. With increasing distance, the correlation between the angular distribution of the photons and the source position deteriorates. The effects of photon absorption and scattering can be quantified by the absorption length (λ_{abs}) and the scattering length (λ_{scat}) which are both wavelength dependent. The intensity of the light emitted by a muon (I_0) is related to the intensity (I) at distance r from the muon track by

$$I \propto I_0 \frac{1}{r} e^{\frac{-r}{\lambda_{abs}}} \tag{2.7}$$

The factor $1/r$ comes from the geometrical spread of the Cherenkov cone. The scattering length λ_{scat} is the length at which on average a fraction of e^{-1} of the photons is unscattered. In situ measurements of the water properties [37] give values for λ_{abs} and λ_{scat} of about 60 and 260 meters respectively, at a photon wavelength of 473 nm. The group velocity of light in water is relevant for the measured arrival times of the photons [38]. The corresponding index of refraction has been measured and found to be 1.38 [39] for a wavelength of 460 nm. In the simulation and muon track reconstruction, the assumed wavelength of the photons is 460 nm. Dispersion due to the wavelength dependence of the refractive index introduces a delay of up to 2 ns of the arrival time of photons at a distance of 300 meters [39]. This is included in the simulation.

2.5 Muon energy loss

A muon can interact with matter through several processes [14]. When a muon passes through matter, it ionizes or excites the surrounding atoms, transferring in each case a small a mount of energy. A muon can also interact with atoms through radiative processes. In the nuclear electric field of an atom, a muon can radiate a photon. This process is referred to as Bremsstrahlung. When an electron-positron pair is created, the process is referred to as pair-production. A muon can also interact with an atomic nucleus by the exchange of a (virtual) photon. The relative importance of these processes depends on the energy of the muon, and is summarized in figure 2.3. Below approximately 1 TeV, the energy loss is dominated by the ionisation process. Energy loss through ionisation is approximately constant at a level of about 0.2 GeV/m. The radiative processes have an approximately linear dependence on the energy of the muon. Above about 1 TeV, radiative processes dominate the total energy loss. Because of the stochastic nature of the radiative processes, the actual energy loss shows large fluctuations. The fluctuations manifest themselves by electro-magnetic (pair-production and Bremsstrahlung) or hadronic (photo-nuclear) showers. The cross sections of the radiative processes can be expressed as function of the fractional energy loss ν. The cross section for Bremsstrahlung scales with $1/\nu$ while the dependence of

the pair-production cross section varies between ν^{-2} and ν^{-3}. So, hard energy losses are more likely to happen with Bremsstrahlung showers. Particle showers occurring along a muon track show a particular signature in the detector which have to be taken care of when reconstructing muon tracks. The effects of these showers on the muon track reconstruction and further analyses are considered in chapters 3 and 4.

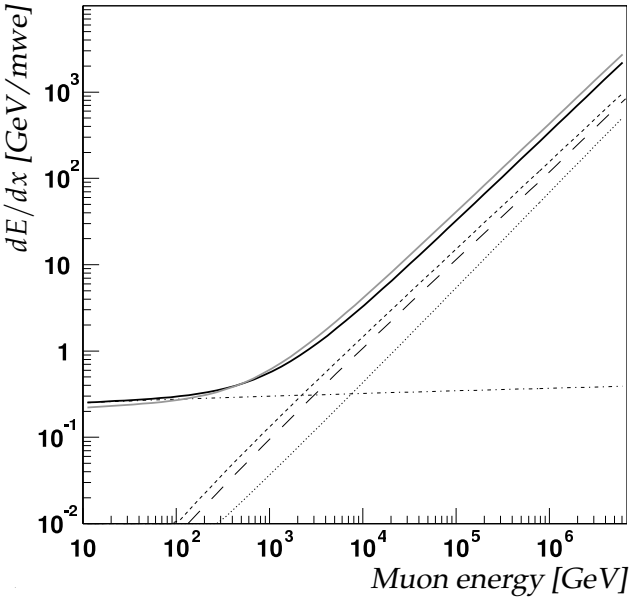

Figure 2.3: *Muon energy loss in GeV per meter water equivalent in water (solid black line) and rock (solid grey line). The separate contributions to the energy loss in water are indicated by the other line types. The short dashed line indicates pair production, the long dashed line Bremsstrahlung, the dotted line nuclear interactions and the dash-dotted line ionisation losses.*

2.6 The Antares neutrino telescope

This section describes the detector hardware design and the read-out system. The telescope is located in the Mediterranean Sea at a depth of 2.475 km at 42°50′ N, 6°10′ E, which is approximately 40 km out of the coast from the city of Toulon, France.

2.6.1 Optical module

The basic light-sensitive element of the Antares detector is a photo-multiplier tube of the type Hamamatsu R7081-20 [40]. It is a hemispherical PMT of 10″ in diameter and has a total sensitive area of about 500 cm^2. The number of amplification stages is 14 and the nominal gain is $5 \cdot 10^7$ at a high voltage of 1760 V. This PMT is sensitive to single photons in the wavelength range between 300 and 600 nm. It has a peak quantum efficiency of about 25 % between 350 and 450 nm. The determination of muon track parameters relies on an accurate measurement of the times at which photons arrive at the PMT. The transit time is the time

between the illumination of the photo-cathode and a subsequent current pulse on the anode. The transit time spread (TTS) is a measure of the fluctuations in transit time in response to single photons. The TTS is defined as the full-width-at-half-maximum (FWHM) of the probability distribution of these fluctuations. The transit time depends on several parameters. Among these parameters are the position and angle of illumination, high-voltage and the intensity of the light. In general the transit time spread is proportional to $1/\sqrt{a_i}$ [41] where a_i is the number of photons. The measurement of the number of photons is usually referred to as the amplitude. The single photon TTS of the PMT is 2.6 ns FWHM. The charge resolution is about 30 % [40]. Every PMT is mounted in a pressure resistant glass sphere with a diameter of 43 cm and a thickness of 15 mm. A gel provides optical and mechanical contact between the PMT and the inner sphere. Shielding from the Earth magnetic field is provided by a μ-metal cage which surrounds the PMT and is partly embedded in the gel. Power to the PMT is supplied by means of an electronics board mounted on the socket of the PMT. This board also transmits the output from the anode and last dynode of the tube. To calibrate the PMT, in particular the transit time, a blue (470 nm) light emitting diode (LED) is attached to the back of the PMT. The back hemisphere of the glass sphere is made opaque by covering it with black paint. A penetrator is used for a cable carrying wires for power, readout and control. The total setup is referred to as an Optical Module (OM). A schematic drawing is shown in figure 2.4.

As the optical modules are the light measuring devices in Antares, it is important to quantify their sensitivity. The limited size of the PMT implies that the optical modules have a varying directional sensitivity. Photons arriving head-on, have a high probability of being detected. On the other side, photons arriving from the rear, hitting the black surface, will not induce a signal. The angular distribution of photons from the different sources covers the complete 4π solid angle. The probability of a photon to be detected depends on several parameters. In addition to the quantum efficiency of the PMT and the absorption coefficients of the gel and glass, the exact path a photon follows through the optical module is of influence. The incident angles and refractive indices determine which path a photon will travel through different materials. Photons arriving at backward angles can be refracted onto the photo-cathode. In order to quantify the angular acceptance of the optical module, measurements and studies have been done. Figure 2.5 shows the relative angular acceptance determined from measurements using atmospheric muons [40] and with a ray-tracing simulation [42]. Also shown is a parameterisation which was based on measurements on a obsolete configuration of the optical module. This parameterisation was used in older versions of the Antares simulation software. As can be seen from figure 2.5, there is an uncertainty in the angular acceptance for the backward regions. This uncertainty will induce a systematic error in the measurements. Currently, new measurements are done in order to reduce this error.

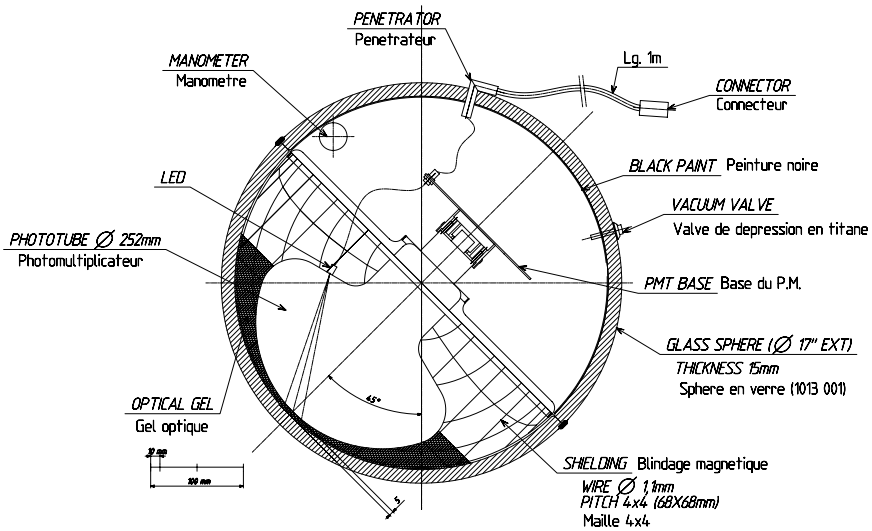

Figure 2.4: *Schematic cross section of the optical module used in the Antares detector.*

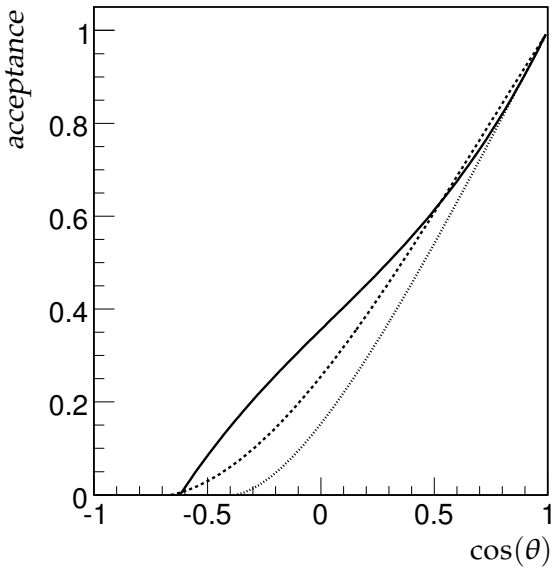

Figure 2.5: *Relative angular acceptance of the Antares optical module as function of the incident angle of the photon (θ). The angle θ is defined with respect to the axis of the PMT and $\cos(\theta) = 1$ corresponds to photons hitting the photo-cathode of the PMT head-on. The solid line is obtained from a ray-tracing simulation [42] and the dashed line from measurements using atmospheric muons [40]. The dotted line was used in older versions of the Antares simulation software.*

2.6.2 Detector layout

The detector layout has been optimized such that the optical modules are distributed in a large (effective) volume and the transport of data, power and control signals is possible. It incorporates equipment for calibration and monitoring of the detector and the environment. An overview of the detector geometry is shown in figure 2.6. Three optical modules are mounted on a titanium frame,

called the optical module frame (OMF), as shown in figure 2.7. The optical modules point downwards at an angle of 45° from vertical, and 120° away from each other. Several other components are mounted on the OMF. A titanium cylinder is used to house the electronics for the read-out of the optical modules and various other instruments for calibration and monitoring. This cylinder is referred to as the local control module (LCM). Some instruments used for calibration of the detector are mounted on some OMFs. A pressure-resistant glass cylinder containing an array of LEDs is used as an optical beacon. These optical beacons are distributed in the detector and are used for the calibration of the PMTs (see section 2.6.4). The OMF with all its components is referred to as a storey. The storeys are linked by an electro-mechanical cable, which has sufficient tensile strength and contains all necessary cables for power and optical fibers for data transport. Five storeys make up a sector. Every sector has its own power supply and communication channel to shore. One of the five storeys in a sector has the functionality in distributing control and data signals to shore. This functionality is implemented in the electronics container. This local control module is referred to as the master local control module (MLCM). Five sectors, thus 25 storeys, are organized in a single vertical line. The storeys are separated by 14.5 meters. The first storey is at about 100 meters from the sea-bottom. A buoyant element at the top keeps the line vertical. A bottom string socket (BSS) is located at the bottom of the line. The BSS consists of a dead-weight to anchor the line to the sea-bottom and a titanium container. This container houses the string control module (SCM) and the string power module (SPM). The SCM consists of electronics for the read-out of several instruments and the distribution of a common clock signal. In addition, the signals from the different sectors are merged into a single communication channel. The SPM distributes power to the different sectors of the line. A laser beacon is mounted on two of the BSSs which is used as an alternative optical beacon (see section 2.6.4). The detector consists of 12 lines, making a total of 900 PMTs. The relative positions of the 12 lines on the sea-floor is shown in figure 2.8. The lines are connected via an interconnecting link cable to a central junction box. The junction box forms the distribution point of power, clock and signals from the shore to the lines. The junction box is connected to shore through a 40 km long main electro-optical cable. The on-shore part of the detector consists of a power feed station and a shore station, where data are received and filtered, a common clock signal is generated and the detector control is housed. The shore station is located in the town of La Seyne-sur-Mer. A dedicated line for the monitoring of the environment is placed in the vicinity of the detector. The detector is installed line by line. Each line is lowered from a ship. A remotely operated submarine vehicle (ROV) is used to connect the line to the junction box with an interconnecting link cable.

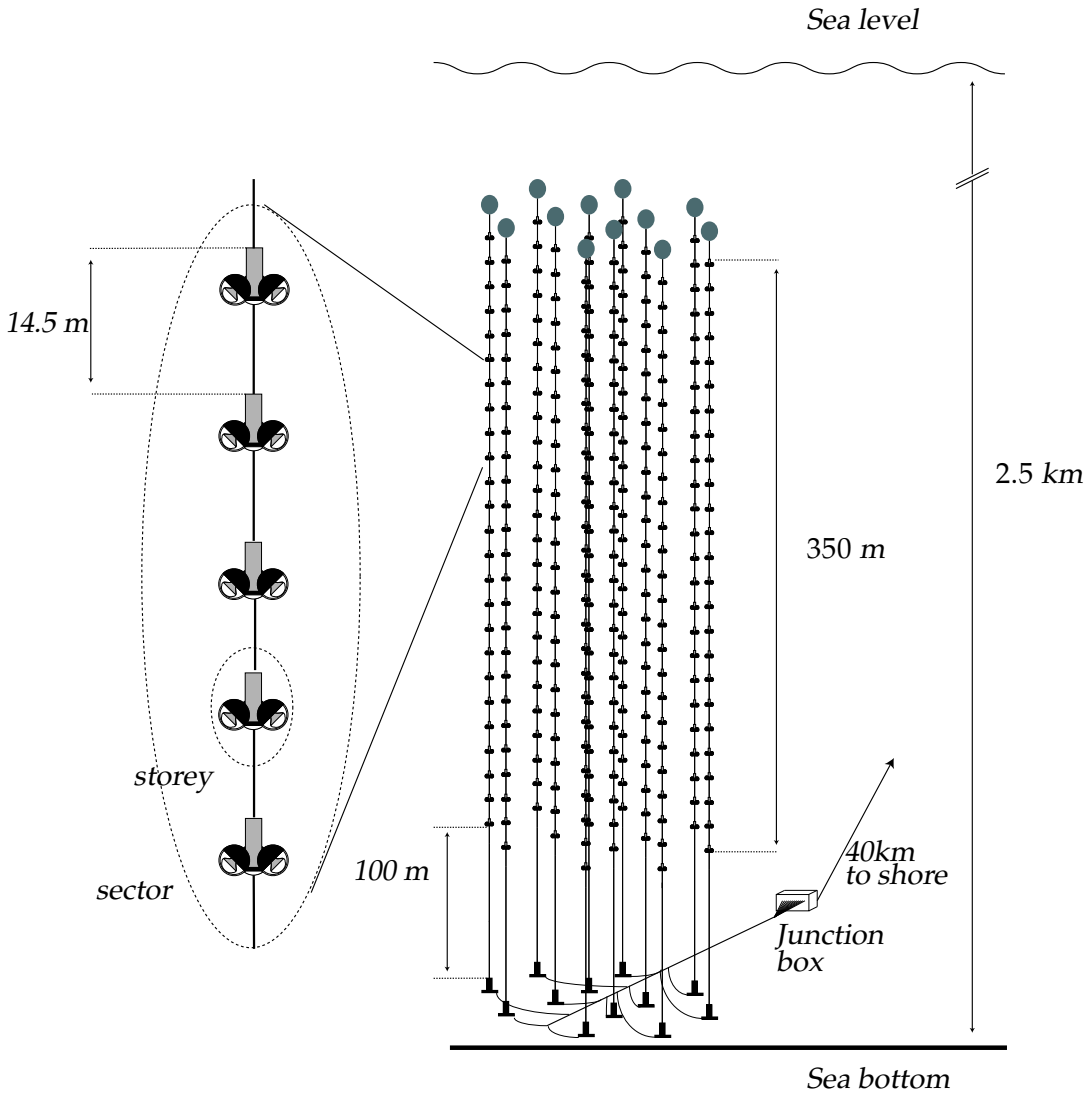

Figure 2.6: *Schematic drawing of the Antares neutrino telescope. The drawing shows the 12 detector lines and one sector consisting of 5 storeys. Each storey has 3 optical modules. The junction box connects the 12 lines to shore through a 40 km long cable.*

2.6.3 Data acquisition

The data acquisition (DAQ) system [44] of the Antares detector includes the digitization of the analogue signal from the PMTs, the transport of the data to shore and the subsequent filtering and storage of the data. The DAQ system is designed around the *all-data-to-shore* concept, which entails the bias-free transport of all photon signals recorded by the optical modules to the shore station where

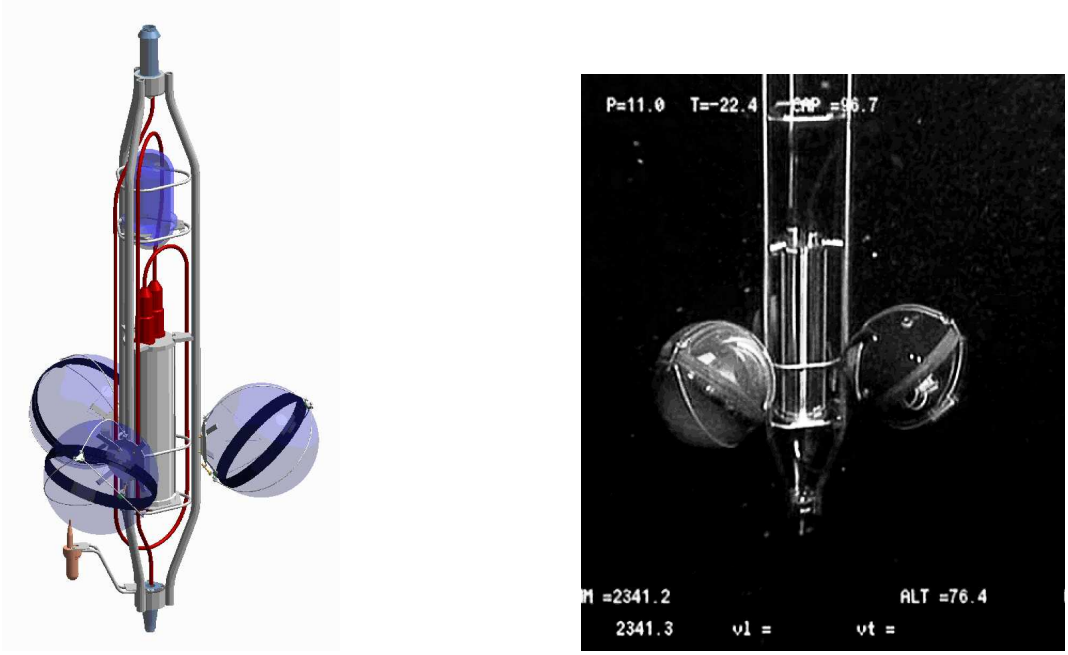

Figure 2.7: *Left : A storey contains three optical modules, a container housing the electronics, and optical beacon and an acoustic transceiver. Right : Photograph of a storey in situ [43].*

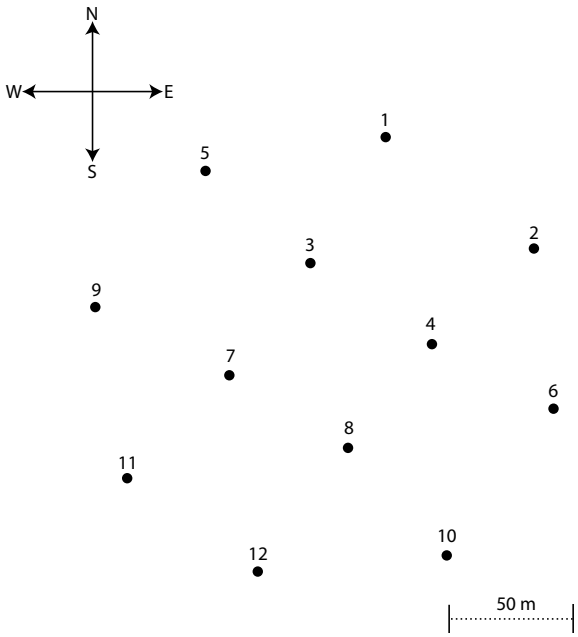

Figure 2.8: *Schematic view of the floor layout of the lines. The numbering scheme of the detector lines is also indicated.*

filtering is performed. A schematic overview of the DAQ system is shown in figure 2.9. The signal from a PMT is read-out and digitized by a custom front-end chip: the analogue ring sampler, ARS [45]. When the signal at the anode of the PMT exceeds a threshold voltage, the charge is integrated by the ARS. The typical threshold value corresponds to 0.3 photo-electrons. The duration of the integration gate is set to 33 ns. The ARS can also function in waveform mode, in which the photo-multiplier signal is sampled and digitized. In this work, the waveform mode is not used. A local clock supplies a reference signal to the ARS which is used to timestamp each PMT signal above threshold. The clock has a frequency of 20 MHz. Sub-nanosecond timing is achieved by time-to-voltage converters (TVCs) which provide interpolation between the clock pulses and are read-out by 8-bit analog-to-digital converters (ADCs). The combined time and charge information of a PMT signal is referred to as a hit. After the integration gate, the ARS has a dead-time of about 200 ns. In order to reduce the effects of the dead-time, each PMT is read-out by two ARS chips. Each pair of ARS chips functions in a token ring scheme. The minimum time between two consecutive hits is 45 ns. The ARS is read-out by a field programmable gate array (FPGA) and buffered in a 64 MB memory. The data are organized in frames covering a time period of 104.858 ms. A central processing unit (CPU), running the VxWorks real time operating system functions as the interface with the on-shore systems. The CPU runs two programs. The first is used for the processing of ARS data (*DAQHarness*). The second program (*SCHarness*) is used to control several devices which are connected via a serial port to the CPU, such as the power supply, compass and tilt-meter. Data from these devices are referred to as slow-control data. The communication to shore is done using the TCP/IP protocol. For this, the CPU has a 100 Mb/s Ethernet interface. The effective throughput of the CPU corresponds to a maximum mean rate of about 300 kHz per optical module. The data are transmitted using optical fibers. The additional functionality of the MLCM consists of merging the bi-directional optical 100 Mb/s Ethernet links from the LCMs into a single 1 Gb/s Ethernet link to shore using two uni-directional optical fibers, one for incoming and one for outgoing data. In the SCM, the signals from the MLCMs are combined in a single pair of optical fibers. The pairs are then routed through the junction box to the shore station.

On shore, the optical signals are decoded and routed through a large 1 Gb/s Ethernet switch. This Ethernet switch connects the off-shore processors to the on-shore computing farm, consisting of commodity PCs. By the use of Ethernet and the TCP/IP protocol, each on- and off-shore processor is addressable by its IP-address. The transfer of data and control signal is thus completely transparent.

The software processes running on- and off-shore are synchronised by an implementation of a finite state machine using the CHSM language [46]. The program *RunControl* [47] manages the state-transitions of the processes and distributes configuration data. All configuration data are stored in a database. The *RunControl* is the main user-interface to the experiment. Data and messages are

distributed following the concept of tagged data by the *Ligier* program, which is an implementation of the *ControlHost* [48] package. The data-taking is organized in data-taking runs. Each data-taking run corresponds to a period of typically 5 hours. The start and stop times of each run are stored in a database by the Run-Control. During a run, the data frames from the LCMs corresponding to the same time period are sent to a single on-shore PC. The frames of a following time period are then sent to a different PC. The set of frames of a single time period are referred to as a timeslice.

When required, the DAQ system can run with a sampling factor. This reduces the incoming data-stream by synchronously processing only every N^{th} timeslice. This reduction already takes place at the level of the (M)LCM where only the N^{th} frame is written to the on-board memory.

Following the all-data-to-shore principle, no filtering of the data, except for a 0.3 photo-electron threshold, is done off-shore. Consequently, a large amount of data (see section 2.7) has to be processed in real-time. This processing is done using the farm of PCs. Each of these PCs have the *DataFilter* program running for this task. The method of extracting the physics signal from the data is described in section 2.8. After filtering, the selected data are sent to a PC running the *DataWriter* program which writes the data to disk. For the storage of data, the ROOT [49] software package is used. Slow-control data-taking is controlled by the *ScDataPolling* program and written to the database by the *DBWriter* program.

Clock

The clocks in the (M)LCMs are synchronised by a common clock signal. This clock signal is generated on-shore and is synchronised with GPS time to an accuracy of 100 ns. The clock signal is converted into an optical signal and distributed through the optical network. By measuring the return time of a calibration signal, the relative phase-offsets of the local clocks can be determined.

2.6.4 Calibration

Position calibration

The Antares detector is not a rigid structure, and the deep-sea environmental conditions are variable. The detector lines are subject to forces caused by sea currents, which make them sway and torque. For the reconstruction it is necessary to determine the relative position of the PMTs. For this, two independent systems are in place [1]. The first is the acoustic positioning system. By measuring the travel times of acoustic pulses, a three-dimensional reconstruction of the detector elements can be made. The pulses are in the 40-60 kHz range and are transmitted by emitters located at the BSS of each line. Along each line, there are

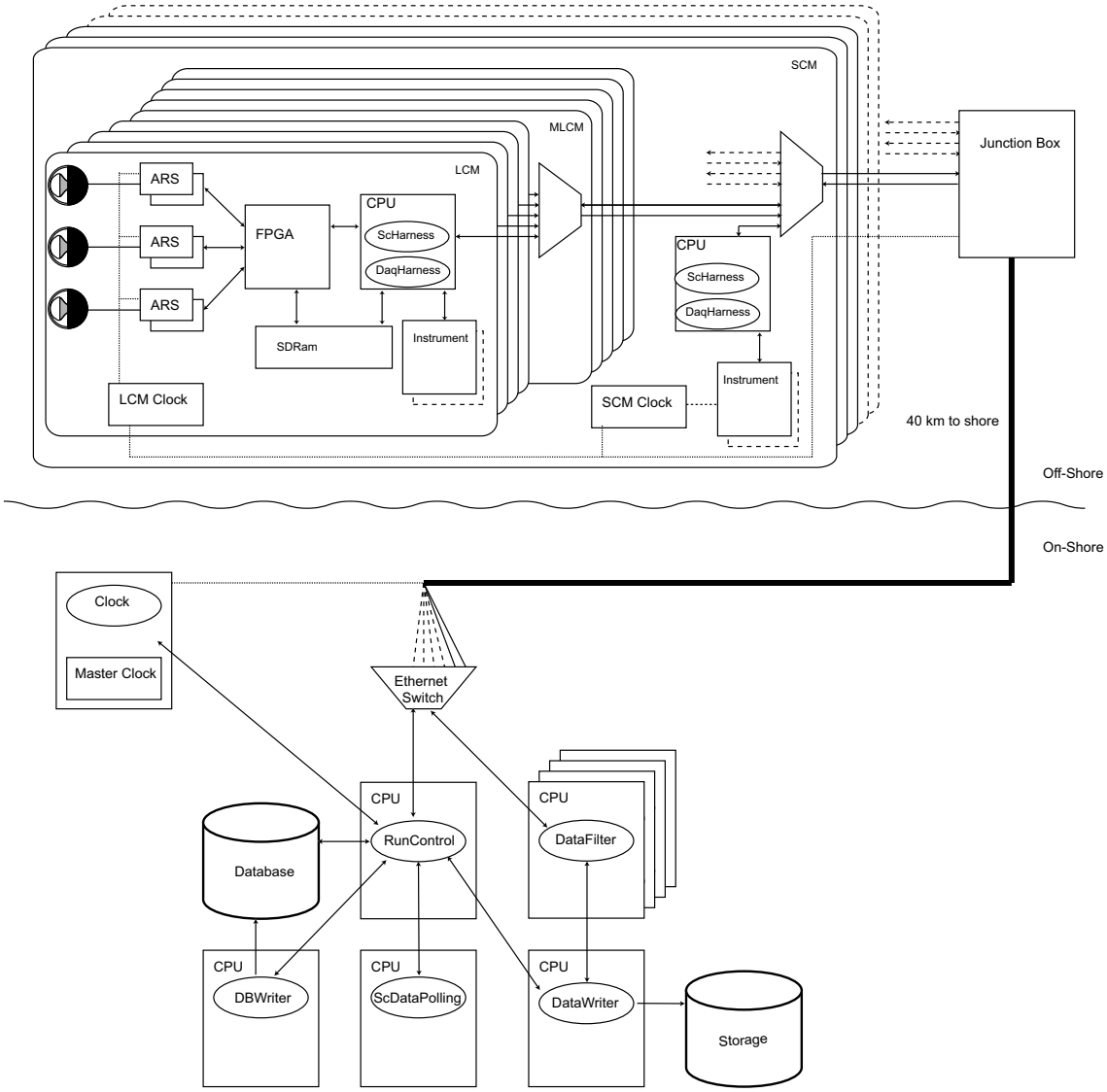

Figure 2.9: *Schematic overview of the Antares DAQ system. Square boxes indicate hardware components and ovals indicate software processes. Lines with arrows indicate the direction of data flow. The dotted line indicates the distribution of the clock signal. The thick black line indicates the 40 km long main electro-optical cable. Cylinders indicate data storage systems.*

five acoustic receivers, called hydrophones. The transmitters are also capable of receiving signals. Four additional autonomous transponders are located around the detector to increase the accuracy of the global alignment. The depth of the BSS is determined with pressure sensors located at the BSS and during connection to the junction box with a pressure sensor on the submarine. The speed of

sound is dependent on pressure, temperature and salinity. Therefore, the detector is equipped with sound velocity meters and with independent pressure, temperature and salinity measuring devices. In addition to the acoustic system, each LCM is equipped with a bi-axial tilt meter and compass. This is used to measure pitch, roll and heading. The positioning system is designed to measure the position of each OM within 10-20 cm [1]. The absolute orientation of the detector is determined with the use of the autonomous transponders, which have a known position, determined during their deployment. The relevant variables are the tilt angles along the North-South and East-West axes and the heading with respect to the North-South axis.

Time calibration

The time resolution of the Antares detector is limited by the PMT transit time spread (see section 2.6.1) and the scattering and chromatic dispersion of Cherenkov light (see section 2.4). The electronics of the Antares telescope is designed to contribute no more than 0.5 ns to the uncertainty in the timing. Thus, the timing calibration should have a precision better than a nanosecond. Several systems are in place to perform calibration measurements. As mentioned in section 2.6.3, the LCMs can echo a calibration pulse sent by the clock system. In this way, the relative offsets of the local clocks can be measured with 0.1 ns accuracy. The internal LED of the OMs (section 2.6.1) is used to measure the relative variation of the TTS of the PMTs. For the measurement of the relative timing between different optical modules and the influence of light propagation, a system of optical beacons is in place [50]. The system consists of two types of pulsed light sources.

First, there are LED beacons mounted on several storeys on a line that can illuminate storeys on neighboring lines. A LED beacon consists of a borosilicate glass cylinder containing a hexagonal structure with on each face 6 LEDs. One of the LEDs on each face points upwards. These LEDs illuminate the storeys above on the same line. The LEDs emit light with a wavelength of 472 nm. The rise time of the light pulse is about 2 ns. The LEDs flash at a typical frequency of a few Hz.

Second, a laser beacon is mounted at the bottom of two lines. The laser beacons illuminate the lower part of the detector. The laser beacon is housed in a cylindrical container. The light is emitted from the top through a diffuser. The laser emits light at a wavelength of 532 nm in a triggered mode.

Tests with the optical beacon system [50] have shown that the timing resolution of the detector electronics is about 0.5 ns, well within the design parameters.

2.7 Signal and background

Although the main aim of the Antares telescope is to detect light caused by the interactions of cosmic neutrinos, it is by far not the only source of light in the

deep-sea. Three sources of detectable light are shown schematically in figure 2.10. Particles, known as cosmic rays, impinging on the atmosphere, can interact and iniate particle cascades, producing air-showers. Charged mesons created in these showers can decay to muons and neutrinos. A fraction of the muons created in the showers overhead can reach the detector site despite its depth. Several muons originating from a single cosmic-ray interaction in the atmosphere can reach the detector simultaneously. Due to the mass column presented by the Earth, the angular distribution of the atmospheric muons is limited to the downward directions. Neutrinos produced by cosmic-ray interactions, however, can traverse the Earth. These neutrinos can interact in the vicinity of the detector and produce a muon or other detectable particles. Muons created in the interactions of atmospheric neutrinos can originate from all directions. The muon fluxes caused by atmospheric neutrinos and atmospheric muons are shown in figure 2.11. Around horizontal directions, the flux of atmospheric neutrinos is enhanced due to the increased path length in the upper atmosphere, favoring the decay of mesons. The signals caused by muons originating from any of the three sources mentioned above are indistinguishable. After muon track reconstruction, the different signals can be distinguished. By selecting tracks with upward going directions, the atmospheric muon bundles can be rejected. However, atmospheric muons can sometimes be mis-reconstructed and classified as upward going. Hence, when looking for cosmic neutrinos, there is a background from both atmospheric muons and neutrinos. Various ways to reduce this background are presented in chapter 5.

Another kind of background that is not related to a passing muon or a neutrino interaction is present in the deep-sea. This background can be expressed as the number of detected photons per optical module per second. A large contribution to this background is due to the decay of ^{40}K. The dominating decay channel is a β decay producing a low-energy (up to 1.3 MeV) electron which then emits Cherenkov light. The contribution to the background depends on the concentration of ^{40}K and the absorption length. The counting rate has been estimated and found to be about 30 kHz [51],[52] and [53]. Another contribution to the counting rate is caused by light emitted by various living organisms in the deep-sea. This is known as bioluminescence [54],[55]. The variation of the counting rate due to bioluminescence shows a few different time scales [53]. A continuous component can be recognized to which the potassium decay, the PMT dark current (about 3 kHz) and bioluminescent bacteria contribute. This contribution is referred to as the baseline rate. It can vary on a timescale of several hours to days between about 50 kHz and several hundred kHz. On top of the baseline rate, bursts of bioluminescent activity occur, lasting from several milliseconds to minutes. These bursts are very local, with counting rates varying from hundreds of kHz to a MHz. These bursts are attributed to macro-organisms. The number of bursts is quantified by the burstfraction, which is the fraction of time that the counting rate exceeds the baseline by 20 % or more.

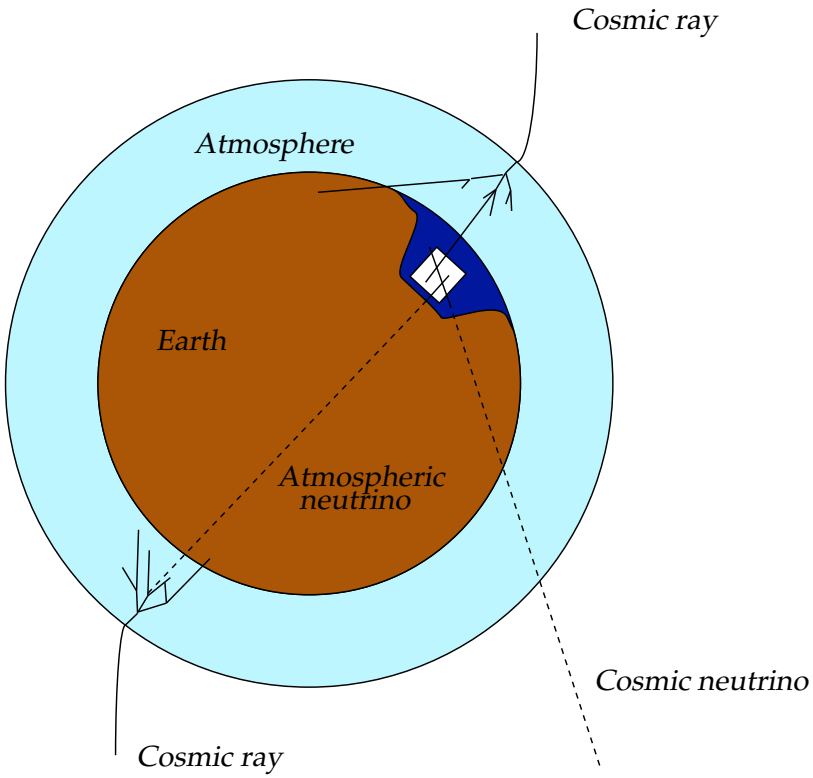

Figure 2.10: *Schematic drawing of the different sources of muons seen in the detector. A cosmic neutrino (dashed, lower right) crosses the Earth and interacts near the detector, creating a detectable muon. A cosmic ray induced muon can reach the detector. A cosmic-ray induced neutrino can cross the Earth and produce a detectable muon as well.*

The background is handled at several levels. The incoming signal of the detector is filtered. In this, the correlated signals expected from muons are separated from the uncorrelated signals of the background. This filtering is described in section 2.8. The influence of the background rate on the determination of muon track parameters is described in chapters 3 and 5. The final background rejection is discussed in chapter 5.

2.8 Trigger

All PMT signals exceeding the 0.3 photo-electron threshold are transferred to shore. These hits are referred to as *L0* hits. The dominant contribution to the data are the hits due to the decay of ^{40}K and bioluminescence. At a rate of 70 kHz per optical module, this results in about 0.5 GB/s transferred to shore. The hits

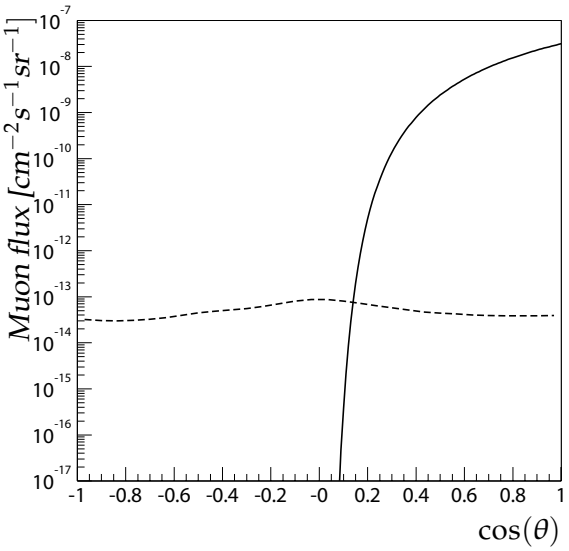

Figure 2.11: *Muon flux at a depth of 2.1 km as a function of zenith angle. The zenith angle indicates the direction from where the muons are coming,* $\cos(\theta) = 1$ *indicates from above the detector. The solid line corresponds to the flux of atmospheric muons. The dashed line corresponds to the flux of muons due to atmospheric neutrinos. Only muons with an energy larger than 100 GeV are included.*

caused by this background are uncorrelated and so constitute a random background. The photons which originate from a single event, e.g. a particle crossing the detector, are causally related. A recorded hit from such an event therefore provides information on possible times and positions of other photons that can be detected. The causal relations can thus be used to filter the data. In general, this is done by finding clusters of correlated hits. A cluster of correlated hits is defined as a set of hits, which are all pair-wise related through a causality criterion. When a sufficiently large cluster of causally related hits in a timeslice is found, the data are saved, otherwise they are discarded. The set of correlated hits is usually referred to as an event. The data contain all hits that triggered the event, together with all hits in a time window from 2 μs before the first hit to 2 μs after the last hit (the so-called snapshot). The event is stored in a data structure called *PhysicsEvent*. The process of finding the event is done in software that runs on the PCs receiving the timeslices. Each of these PCs run the DataFilter program. As all the triggering is done in software there is a large flexibility in the algorithms used to filter the data. Different trigger algorithms can be used for different analyses. Several trigger algorithms can run in parallel on the same data.

In the following, the main trigger algorithm will be described. The trigger exploits the causal relation between hits caused by a relativistic muon crossing the detector. As a first step, the trigger algorithm searches for hits which form a coincidence within a storey, or alternatively single PMT's with a large amplitude. The time window for coincidence is $\pm$20 ns. The selected hits are called *L1* hits. The selection of L1 hits is made to suppress random background. Multiple photons arriving on the same PMT within the integration gate of the ARS will increase the measured charge. The time window of 20 ns accounts for time delays due to the difference in position of the PMTs, dispersion and scattering of the light and uncertainties, at triggering time, in time calibration. The threshold for

a high-amplitude L1 hit is set at 2.5 photo-electrons. Considering muons travel at the speed of light, the largest time difference between two PMTs is associated with the velocity of photons traveling through the water. This speed is equal to the speed of light divided by the index of refraction. So, for two hits i and j to be causally related

$$|t_i - t_j| \leq |\vec{x}_i - \vec{x}_j| \times n_g/c \tag{2.8}$$

Where $t_{i(j)}$ and $\vec{x}_{i(j)}$ are the time and position, respectively, at which hit $i(j)$ is recorded. The speed of light in vacuum is given by c and the group refractive index by n_g. The trigger algorithm looks for the largest subset of L1 hits which are pair-wise causally related according to equation 2.8. The minimum number of causally related L1 hits required to trigger the event is usually set at 5. The causality relation (2.8) is valid for a muon traveling in any direction. By adding information about the (assumed) direction of the muon, the causality criterium can be made more restrictive. In the context of gamma-ray burst studies [47] a *directional* causality criterium was developed. This causality relation will be described in more detail in chapter 3. The standard trigger uses this directional causality relation to reduce the rate of triggers due to random background. When a sufficient number of causally related hits are found, the algorithm applies the directional causality relation to the hits. This is done for about 200 different directions spread isotropically over the full solid angle. The number of directions matches the field of view of the directional trigger. When for a given direction a sufficiently large cluster of hits is found, the event is written to disk. Besides storing triggered events, all incoming data is summarized. A *SummaryTimeSlice* is generated for each timeslice which contains the number of L0 hits that were recorded by each optical module. The SummaryTimeSlices are stored together with the PhysicsEvents.

Several trigger algorithms can run in parallel. These include a dedicated trigger for gamma-ray bursts [47], a dedicated trigger for magnetic monopoles [56] and a source tracking trigger.

The trigger greatly reduces the data-stream. The trigger rate due to random background depends on the rate per optical module. For background rates of 70, 100 and 200 kHz per optical module the respective trigger rates are about 0.01, 0.1 and 30 Hz, corresponding to data rates between about 0.03 and 180 kB/s. The dominating trigger rate with low background is due to the atmospheric muons passing the detector resulting in a rate of about 3 Hz. At trigger level, no distinction is made between events due to atmospheric muons, atmospheric neutrinos or cosmic neutrinos. Further off-line analyses are necessary for further separation. The first step is the determination of the parameters that describe the muon trajectory.

2.9 Current status

Installation of the Antares neutrino telescope began on February 14^{th} 2006 when the first detector line was deployed. This line was connected to the junction box on March 2^{nd}. The line could be operated immediately and data were taken as of day one. Line 1 operated alone until September 21^{st} 2006, when a second line, Line 2, was connected. A detailed analysis of the data taken with Line 1, is presented in chapter 4. The operation of Line 1 overlapped with the operation of a designated instrumentation line. This line, called the Mini Instrumentation Line with Optical Modules (MILOM), was operational from April 2005. The goal of the MILOM was to check the detector elements and to validate the performance of the calibration devices. The MILOM consisted of three storeys. It was equipped with four optical modules, three on the second storey and a single optical module on the top storey. It contained three optical beacons, two LED beacons on the top and bottom storey and a laser beacon on the BSS. Several devices to measure the water properties were mounted on the MILOM. An acoustic Doppler current profiler (ADCP) was installed on the top storey to measure water currents. A conductivity and temperature sensor was mounted on the first storey and a sound velocity sensor on the second storey. Acoustic hydrophones were mounted on several storeys. Operation of the MILOM validated most of the systems [53]. The timing resolution was found to be better than 0.5 ns and the position resolution about 10 cm. Today (December 2007) the Antares neutrino telescope has ten lines and an instrumentation line operational. The full detector is expected to be operational in the beginning of 2008.

2.10 Simulation

In this section, the software used for the simulation of the processes leading to a detectable signal in the detector and the subsequent detector response are described. This includes neutrino and cosmic ray interactions, the propagation of the secondary particles and the random background. Also, the simulation of the data-acquisition system of the Antares detector is described. These simulations are necessary to understand the detector response and to validate analysis techniques.

Due to the attenuation of light, the production of a detectable signal needs to be considered only in the vicinity of the detector. The simulation of the production of photons is therefore limited to a cylindrical volume around the detector, referred to as the *can*. The can extends 2.5 absorption lengths around the detector. As muons can traverse distances up to several kilometers, all processes leading to a muon have to be simulated at larger distances away from the detector. Neutrino interactions are generated in a larger volume around the detector. The size of this volume depends on the neutrino energy. The generation of neutrino events is

described in section 2.10.3.

Muons from cosmic-ray interactions are generated directly on the can using a parameterisation based on a full simulation of the cosmic-ray interaction and propagation of the subsequent shower particles. The simulation of atmospheric muons is described in section 2.10.2. A realistic background is made using real data. The random background together with the simulation of the data acquisition system is presented in section 2.10.5. A general weighting scheme, primarily used for the simulation of neutrinos is described in section 2.10.1

2.10.1 Weights

An evaluation of the detector performance involves evaluating complex multi-dimensional integrals. This can be done efficiently by means of Monte Carlo integration [57]. In Monte Carlo integration, an integral can be approximated by the uniform random sampling of N points x_i in the phase space volume V.

$$\int f dV \approx V \frac{1}{N} \sum_{i=0}^{N-1} f(x_i) \tag{2.9}$$

In general, a uniform sampling is not the best choice, because the probability density function (PDF) of the physical process under study favors certain parts of phase space. Another aspect is the optimization of the statistics within the phase space. A way to take this into account is *importance sampling* (see for example reference [58]). This generalizes formula 2.9 to the case of non-uniform sampling. This means that, when sampling according to a normalized probability density p, equation 2.9 generalizes to

$$\int f dV = \int \frac{f}{p} p dV \approx \frac{1}{N} \sum_{i=0}^{N-1} \frac{f(x_i)}{p(x_i)} \tag{2.10}$$

If an unnormalized distribution $\hat{p}$ is used, it can be normalized by dividing by V_p:

$$V_p \equiv \int \hat{p} dV \tag{2.11}$$

and thus

$$p = \frac{\hat{p}}{V_p} \tag{2.12}$$

After inserting this into equation 2.10 one obtains

$$\int f dV = \int (V_p \frac{f}{\hat{p}}) \frac{\hat{p}}{V_p} dV \approx \frac{V_p}{N} \sum_{i=0}^{N-1} \frac{f(x_i)}{\hat{p}(x_i)} \tag{2.13}$$

This result is used for the calculation of event rates. The event rate R can be calculated with :

$$R = \int P_{Earth}(E, \hat{d})\sigma(E)\rho(\vec{x})N_a\Phi(E, \hat{d})P_{det}(\vec{x}, \hat{d}, E)d\vec{x}d\Omega dE \tag{2.14}$$

where $\vec{x}$, $\hat{d}$ and E are the position of the neutrino interaction, the direction of the neutrino and the neutrino energy, respectively. The other quantities are

P_{Earth} : the probability that the neutrino reaches the detector without interacting

$\sigma(E)$: total neutrino cross section

$\rho(\vec{x})$: target density

N_a : Avogadro's number

$\Phi(E, \vec{d})$: differential neutrino flux before crossing the Earth. Typical units are number of particles per solid angle, time, area and energy (sr^{-1} s^{-1} m^{-2} GeV^{-1})

P_{det} : probability of detection

The simulated events are generated following a power-law distribution in energy, $\Phi_{gen} \propto E^{-\gamma}$. The spectral index γ is in general chosen such that the statistics at higher energies are sufficient. Normalizing the generation flux on the energy interval used for generation yields

$$\Phi_{gen} \propto \frac{E^{-\gamma}(1-\gamma)}{E_{max}^{1-\gamma} - E_{min}^{1-\gamma}} \tag{2.15}$$

Combining this with equation 2.14 according to the prescription of equation 2.13 gives :

$$\begin{aligned} R = &\frac{V 2\pi \cos(\theta_{max} - \theta_{min})(E_{max}^{1-\gamma} - E_{min}^{1-\gamma})}{(1-\gamma)N} \times \\ &\sum_{i=0}^{N-1} P_{Earth}(E_i, \hat{d}_i)\sigma(E_i)\rho(\vec{x}_i)N_a P_{det}(\vec{x}_i, \hat{d}_i, E_i)E^{\gamma}\Phi(E_i, \hat{d}_i) \end{aligned} \tag{2.16}$$

Which can be simplified to

$$R = \frac{1}{N}\sum_{i=0}^{N-1} w_i \Phi(E_i, \hat{d}_i) \tag{2.17}$$

With w_i defined as

$$\begin{aligned} w_i \equiv & \frac{1}{1-\gamma} \times \\ & V 2\pi \cos(\theta_{max} - \theta_{min})(E_{max}^{1-\gamma} - E_{min}^{1-\gamma}) \times \\ & P_{Earth}(E_i, \hat{d}_i)\sigma(E_i)\rho(\vec{x}_i)N_a P_{det}(\vec{x}_i, \hat{d}_i, E_i)E^{\gamma} \end{aligned} \tag{2.18}$$

This quantity is referred to as the weight and is calculated for each generated event. In the example given above, the event rate for a different flux can be calculated by replacing the flux in equation 2.17 by another. This removes the need to repeat the simulation when only the input flux is changed, provided that the sample contains enough statistics over the covered phase space.

2.10.2 Atmospheric muons

For the simulation of the flux of muons originating from cosmic rays, the fast simulation package MUPAGE [59] is used. MUPAGE generates atmospheric muon events at the level of the can. It is based on a parametrization of the atmospheric muon flux at the depth of the detector [60]. The parametrization is tuned on a simulation done with HEMAS [61],[62]. HEMAS simulates the primary cosmic ray interaction and propagation of the subsequent shower. The model used for the hadronic interaction is DPMJET [63]. The input to the HEMAS simulation is the primary cosmic ray flux. A phenomenological model described in [12] is used, which combines results from direct and indirect measurements of cosmic rays in an energy range from 10 GeV to 1 EeV. The propagation of muons from sea-level down to the can is simulated with the MUSIC [64] package. MUSIC takes into account energy losses due to Bremsstrahlung, pair production, inelastic scattering and knock-on electrons. It includes the distortion of the muon direction due to multiple scattering, inelastic scattering and pair production. The distributions obtained by the simulation are used to fix the parametric formulas in MUPAGE. As MUPAGE generates the events according to their abundance, no weighting of the events is needed. Each set of events corresponds to a certain observation time.

2.10.3 Neutrinos

Neutrino interactions are generated isotropically in the extended volume around the can. The size of this volume depends on the maximum neutrino energy and the zenith angle considered. The size is such that interaction products of the most energetic interactions can reach the can. The size of the generation volume is mainly determined by the muon range at the highest considered energy. For the generation of neutrino events, the Genhen [65] software package is used. The deep inelastic neutrino interactions are simulated using the LEPTO package

[66]. LEPTO integrates the differential cross sections and provides the kinematic properties of the outgoing muon. The hadronisation of the nuclear fragments is done with PYTHIA 5.7 and JETSET 7.4 [67]. The CTEQ6D parton distribution functions [33] are used. For each event, the appropriate weight is calculated (see section 2.10.1). The probability for a neutrino to reach the interaction point is included in the weight. This survival probability is calculated from the neutrino energy and the column density through the Earth associated with the neutrino direction. The calculation is done with the appropriate neutrino cross sections and takes into account the decreasing probability of a neutrino penetrating the Earth with increasing energy. If a neutrino interaction takes place within the can, all resulting particles are stored for further processing, otherwise, only the resulting muons are propagated to the can using the MUSIC package.

The most frequent neutrino signal in the Antares detector is due to atmospheric neutrinos. The atmospheric neutrino flux consists of a part due to decay of pions and kaons produced in cosmic ray interaction. In addition, there is a contribution due to the decay of charm mesons. These prompt neutrinos dominate the atmospheric neutrino flux at neutrino energies above 10^5 GeV. In this work, the atmospheric neutrino fluxes described in [68] and [69] are used.

2.10.4 Photon generation

The production of Cherenkov light is simulated within the can volume. The propagation of muons and the associated production of light is simulated using the KM3 [39] program. Within KM3, a modified version of the muon propagation code MUSIC is used. Propagation of muons is performed in steps of one meter. If the energy loss of the muon in a single step exceeds 0.3 GeV, an electromagnetic shower is generated at a random point along the path. The photon yield is extracted from pre-calculated tables in order to speed up the simulation. These tables are generated from a full simulation of a large number of muons and electro-magnetic showers with GEANT3 [70]. Measured properties of the water at the Antares site are used to simulate effects due to absorption, scattering and dispersion of the photons. The properties of the optical module are used to determine the number of detected photons. These properties include the wavelength dependent quantum efficiency and absorption in glass and gel and the angular dependence of the acceptance of the PMT.

When a neutrino interaction occurs within the can volume, the propagation of the secondary particles, excluding muons, is done with the GEASIM software package [71]. GEASIM is based on GEANT3 and performs full tracking of the particles and relevant physics processes, however, the scattering of photons is not simulated. The response of the optical modules is simulated in the same way as in KM3.

2.10.5 Simulation chain

As described in section 2.6.3, the off-shore DAQ processes supply the DataFilter process with data in a continuous stream. The simulation provides data on an event by event basis. Therefore, a dedicated software chain simulates detector operation and data taking. The chain for processing the simulated events is shown schematically in figure 2.12. A schematic view of the real data flow is also shown. The *MonteCarloEventWriter* program translates ASCII formatted output files of the physics simulation into ROOT formatted files, for efficient storage and processing. The *TriggerEfficiency* program performs the following tasks :

Electronics and PMT simulation The hits from the physics simulation are encoded in a similar way as the off-shore processes do. This includes translating the time to timestamp and TVC data and the amplitude to AVC data. This includes the effect of the ARS integration gate of 45 ns, the dead-time of 200 ns, a TTS of 1.5 ns and a typical gain spread of 30% for single photoelectrons.

Background As described in section 2.6.3 the on-line DAQ processes record the total number of L0 hits and store the data in SummaryTimeSlices. These data can be used to reproduce the uncorrelated background according to the actual conditions of a data-taking run. The data are transformed to Monte-Carlo compatible information using the program *SummaryTimeSliceWriter*. The background for a 12-line detector can be simulated using data from Line 1. The TriggerEfficiency program generates hits for each data frame according to a flat background with a rate corresponding to a randomly picked SummaryTimeSlice. These hits are then added to the data from the physics simulation.

Triggering Any of the trigger algorithms which are used in the DAQ system can be applied to the simulated data. The algorithms are identical for measured and simulated data as they share the same code. When a trigger is found, a PhysicsEvent is written to disk, together with the corresponding SummaryTimeSlice.

Writing of Data When an event is triggered, the resulting PhysicsEvent is written to disc, together with a SummaryTimeSlice and the Monte-Carlo truth information, stored in the *Event* class. Optionally, the truth information can also be written to disc even if there is no trigger.

The end-product of this chain are files that are similar to the ones produced by the DAQ system. This facilitates the use of the same programs for further analysis of the data and comparisons with the Monte-Carlo data.

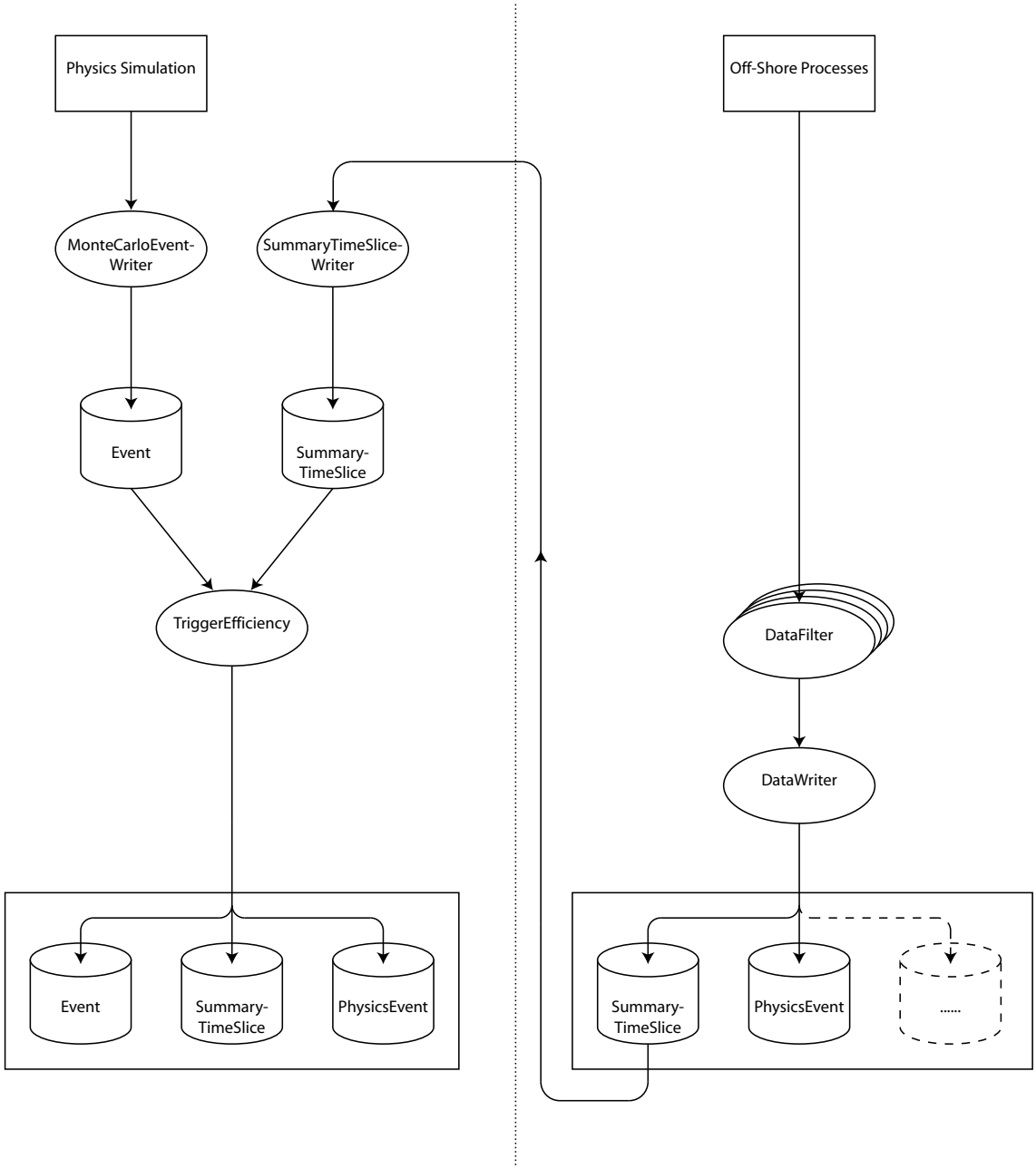

Figure 2.12: *Schematic view of the flow of data through the chain of simulation programs (left) and data (right). SummaryTimeSlices from data are used to generate the random background in the simulation.*

2.10.6 Analysis

The PhysicsEvents contain the raw ARS hit data. The TVC, timestamp and AVC values together with the logical identifiers of the ARSs can be converted to units which are directly used in the analysis. The conversion of the raw units involves

applying the calibration. Routines to make the conversion are available in the Antares DAQ software [72] which includes a common interface for both simulated and real detector geometries, including all calibration constants. The evaluation of the reconstruction algorithm in this work, and the analysis of data are done with stand-alone programs, using the available routines. A version of the reconstruction algorithm is also implemented in the Antares reconstruction and analysis framework [73] which was under development at time of writing of this thesis.

Chapter 3

Reconstruction

The process of reconstruction consists of finding values for the free parameters in the assumed model which most likely caused the outcome of the measurement. In the case of muon reconstruction, the basic model is a straight line passing through the detector along which a muon moves with the speed of light producing Cherenkov light on its way. The measurement consists of a set of times, positions and number of detected photons, usually referred to as hits. A commonly used reconstruction algorithm was already available, which is known as AartStrategy and documented in [74]. Alternative algorithms are also available [75], [73]. Here, a novel reconstruction algorithm will be presented that is based on a partial scan of the phase space. This algorithm is known as *ScanFit*.

3.1 Maximum Likelihood

The goal of track fitting is to find the most likely values of the parameters of the muon track $\vec{\theta}$ that caused the hits. The hits are the measurements and are denoted by $\vec{y}$. According to the *Principle of Maximum Likelihood* [57], the best estimate of $\vec{\theta}$ are the values that maximize the product of the probabilities $f(y_i;\vec{\theta})$ of the individual measurements, the likelihood :

$$L(\vec{y};\vec{\theta}) = \prod_{i=1}^{n} f(y_i;\vec{\theta}) \tag{3.1}$$

where i refers to the index of a hit. The search for the parameters $\vec{\theta}$ is in the realm of function optimisation. For practical reasons, it is customary to take the negative logarithm of the likelihood and perform a minimisation on its value. This can be done using custom made algorithms or by making use of an existing software package. In this work both approaches are used. The software package used is MINUIT [76].

The existence of multiple (local) maxima of the likelihood can not be excluded. In addition, symmetries can introduce solutions in different parts of the parame-

ter space that are equally correct, given the same measurements. So, care should be taken of two things. First, the common optimisation algorithms are guided through parameter space by gradients and second derivatives, and thus follow a certain path. When the starting conditions are unfavorable, certain parts of the parameter space will remain unexplored, possibly containing the global maximum of the likelihood. In case there are different solutions which have the same value of the likelihood, they should all be found. The way these two points are taken care of, is by making sure the whole parameter space is explored.

The likelihood used in this work is primarily defined as the product of the probabilities of time t_i of a hit i. The probability of measuring a certain hit time depends strongly on the track parameters. Given the measured time of a hit t_i and the model prediction of the hit time t_i^{th}, the time residual $t_i - t_i^{th}$ can be determined. The probability of measuring a hit with a certain residual is described by a Probability Density Function (PDF)

3.1.1 Probability Density Function

As explained in section 2.5 the photons that are detected are not only caused by direct Cherenkov emission from the muon. Excluding these effects, the PDF of the measured arrival times of photons can be approximated by a Gaussian distribution. The contribution from other processes and the scattering of light introduces a time delay with respect to the hypothesized direct Cherenkov light, as will be shown below. A complete model of a muon should include the positions and energies of electro-magnetic showers along the track. Due to the stochastic nature of these processes the number of parameters would then vary. The way this is usually handled is to include the averaged effects into the PDF. In this, the correlated effects between different hits are neglected. The exact modeling of such a PDF requires reliable knowledge about the contributing processes. These include the knowledge of the involved cross sections, the water parameters like scattering and absorption lengths, and a complete knowledge of the detector response.

3.1.2 The Gaussian approximation

Another approach is to enhance the purity of the measurements with respect to the assumed hypothesis. In the case of muon reconstruction, the hypothesis is that light is emitted from a muon at the Cherenkov angle. In that case, the PDF can be approximated by a Gaussian distribution. When the PDF of the hit-time residuals can be described by a Gaussian distribution with a width σ_i, the likelihood can be expressed as

$$L(\vec{t};\vec{\theta}) = \prod_{i=1}^{n} \frac{1}{\sqrt{2\pi}\sigma_i} e^{-\frac{1}{2}\left(\frac{t_i - t_i^{th}(\vec{\theta})}{\sigma_i}\right)^2} \tag{3.2}$$

Taking the logarithm of this equation yields

$$l(\vec{t};\vec{\theta}) = -\frac{n}{2}\ln 2\pi + \sum_{i=i}^{n} - \ln\sigma_i - \frac{(t_i - t_i^{th}(\vec{\theta}))^2}{2\sigma_i^2} \tag{3.3}$$

Maximizing L is now equivalent to minimizing

$$\chi^2(\vec{t};\vec{\theta})/2 = \sum_{i=1}^{n} \frac{(t_i - t_i^{th}(\vec{\theta}))^2}{2\sigma_i^2} \tag{3.4}$$

The χ^2 is a quantity with well-known properties [57]. One of the advantages is the possibility to use a χ^2 test, which is a way of assessing the goodness-of-fit. It relies on the known distribution of the χ^2 values for a given number of degrees of freedom, n_{dof}. This number amounts to the number of hits minus the number of free parameters in the fit, $n_{dof} = n - n_{par}$. The χ^2 probability corresponds to the likelihood that with a correct model and Gaussian errors, the χ^2 has a value equal or larger than the one obtained, given the number of degrees of freedom.

3.1.3 M-estimator

The χ^2 fitting procedure can be sensitive to so-called outliers. Outliers are hits with large residuals, either negative or positive. The derivative of the χ^2 with respect to the residuals depends linearly on the residual. This causes the weight of an outlier to increase linearly with the value of the residual. To reduce the influence of outliers, a different quantity can be minimized

$$M = \sum_{i=1}^{n} \rho(\frac{t_i - t_i^{th}}{\sigma_i}) \tag{3.5}$$

Where

$$\rho(z) = \ln(1 + \frac{1}{2}z^2) \tag{3.6}$$

This function behaves as the χ^2 function for small residuals. But for large residuals, the χ^2 depends logarithmically on the residual. As a consequence, large residuals have less influence, and the fit result depends less on the few outliers present in the measurement.

3.2 Parameters

In the general case, 5 parameters can describe the muon track. The direction of the muon can be described by the zenith angle (θ) and azimuth angle (ϕ). These

angles can be used to define a rotation of the coordinate system. The axes of the new coordinate system are then given by $\vec{x}' = \mathbf{R}\vec{x}$, where

$$\mathbf{R} = \begin{pmatrix} \cos(\theta)\cos(\phi) & \cos(\theta)\sin(\phi) & -\sin(\theta) \\ -\sin(\phi) & \cos(\phi) & 0 \\ \sin(\theta)\cos(\phi) & \sin(\theta)\sin(\phi) & \cos(\theta) \end{pmatrix} \tag{3.7}$$

The topology is shown in figure 3.1. In the new coordinate system the z-axis points in the direction of the muon. The $z' = 0$ plane is perpendicular to the muon direction. The point at which the muon crosses this plane is given by the parameters a and b. Finally, the time at which the muon crosses the plane $z' = 0$, is referred to as t_0. In summary, the five parameters describing the muon are θ, ϕ, a, b and t_0. Sometimes the angles θ and ϕ are replaced by the unit three-vector $\hat{d} = (\sin(\theta)\cos(\phi), \sin(\theta)\sin(\phi), \cos(\theta))$.

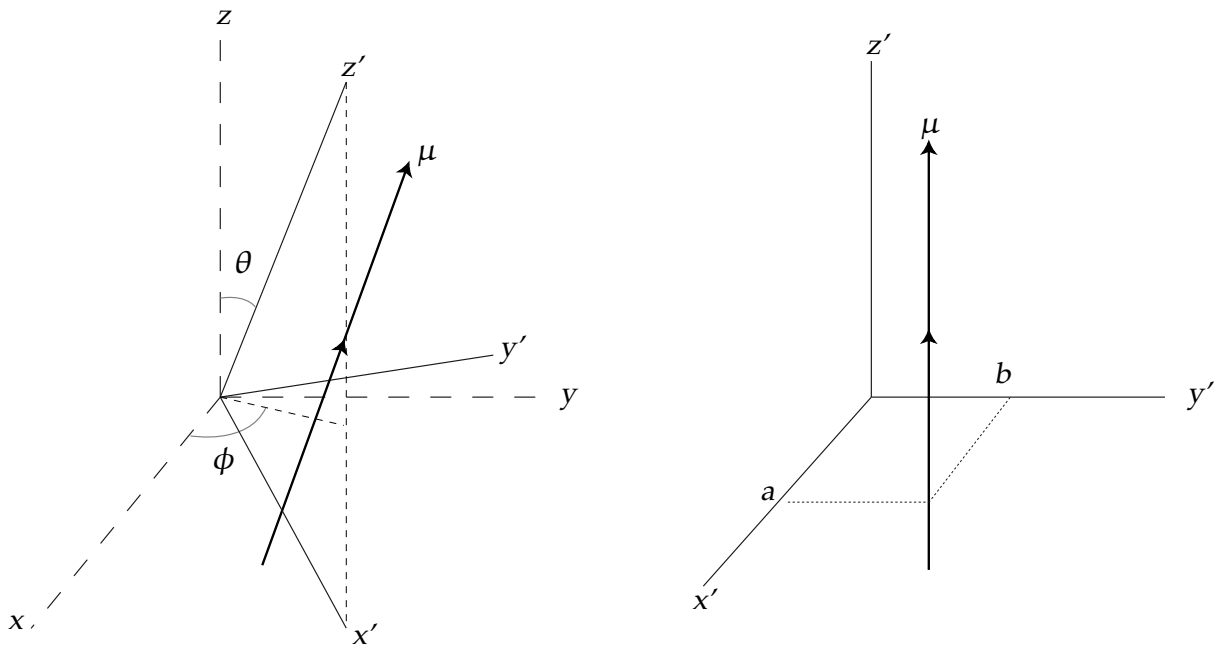

Figure 3.1: *The muon direction is given by θ and ϕ which define a rotation of the coordinate system. The position of the muon track is then defined by the transverse coordinates a and b in the rotated system.*

From the track parameters and the position of a PMT ($\vec{x}$), the arrival time of a photon can be determined. A coordinate system in which the z-axis lies along the muon direction can be obtained by rotating the coordinate system using the given zenith angle θ and azimuthal angle ϕ of the muon. The rotated position of the PMT is $\vec{x}'$. The arrival time of the photon (figure 3.2) can then be expressed as

:

$$t_j = t_0 + \frac{1}{c}\left(z'_j - \frac{r_j}{\tan(\theta_c)}\right) + \frac{1}{v_g}\frac{r_j}{\sin(\theta_c)} \tag{3.8}$$

with z'_j the z-coordinate of the PMT in the rotated frame, $r_j = \sqrt{(a-x')^2 + (b-y')^2}$ the 2D distance between the track and PMT, θ_c the Cherenkov angle and v_g the group velocity of light in water (see figure 3.2).

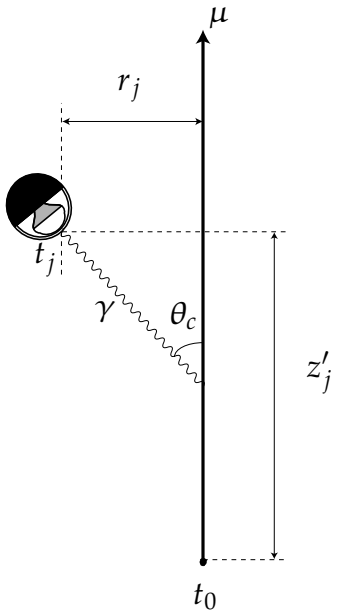

Figure 3.2: *Schematic view of a muon passing an optical module*

3.3 Hit Selection

3.3.1 L1′ Hits

A photon hitting a photomultiplier tube is digitized when the analogue signal from the anode exceeds a certain threshold, typically set at 0.3 photo-electron equivalent charge. The corresponding digital data are referred to as a L0 hit. A local coincidence of L0 hits on the same storey constitutes a L1 trigger. The coincidence gate is usually set at $[-20\text{ ns}, +20\text{ ns}]$. Also a hit with a large amplitude can be considered an L1 trigger. The amplitude has to be larger than a value, a_{th}, referred to as the high-amplitude threshold, and has a typical value of 3 photo-electrons. This value is set to suppress hits from the tail of the 1 photo-electron peak. In this work, single L0 hits are only used if they have an amplitude of at least 0.5 photo-electron. A L1′ hit is defined as the first hit of a L1 trigger. A L1′ hit has a higher probability of being due to direct Cherenkov light from a

muon track, as scattered photons and photons from EM-showers, in general, arrive later than photons from the direct Cherenkov light. To see this, consider a photon emitted from a random point along a track. The arrival time is given by replacing θ_c in formula 3.8 by an angle θ with $0 < \theta < 180°$. This yields

$$t_j = t_0 + \frac{1}{c}\left(z_j - \frac{r_j}{\tan(\theta)}\right) + \frac{1}{v_g}\frac{r_j}{\sin(\theta)}. \tag{3.9}$$

By subtracting 3.8 from 3.9 one obtains the time difference Δt between a Cherenkov photon and a photon emitted somewhere along the track in the direction of the PMT. After some manipulation, this results in

$$\Delta t = \frac{r_j}{c}\left(\frac{1 - \cos(\theta_c - \theta)}{\sin\theta\cos\theta_c}\right). \tag{3.10}$$

The value of Δt has a minimum of 0 at $\theta = \theta_c$ and is positive for any other value of θ. A photon emitted under the Cherenkov angle has the shortest optical path.

3.3.2 1D Clustering

As explained in 2.8 the standard trigger algorithm [72] looks for clusters of space-time correlated hits. Hits are causally related if they satisfy the causality relation 2.8.

In the framework of gamma-ray burst studies, a directional trigger was developed [47]. This trigger makes use of a more restrictive causality criterion. This is possible by using the information on the direction of the muon. When the coordinate system is rotated in such a way that the z-axis lies along the assumed direction of the muon, the expected arrival time t_j of a photon on a PMT can be expressed as in equation 3.8. Using $\kappa = \frac{c}{v_g}\frac{1}{\sin\theta_c} - \frac{1}{\tan\theta_c}$ this equation simplifies to

$$t_j = t_0 + \frac{1}{c}(z_j + \kappa r_j). \tag{3.11}$$

When considering two hits at times t_i and t_j (see figure 3.3) and by taking the time difference, one obtains after some manipulation

$$c(t_j - t_i) - (z_j - z_i) = \kappa(r_j - r_i). \tag{3.12}$$

The value $r_j - r_i$ is maximal and equal to the 2D distance R between the hits R when the muon track crosses either PMT. So

$$-R \leq r_j - r_i \leq R \tag{3.13}$$

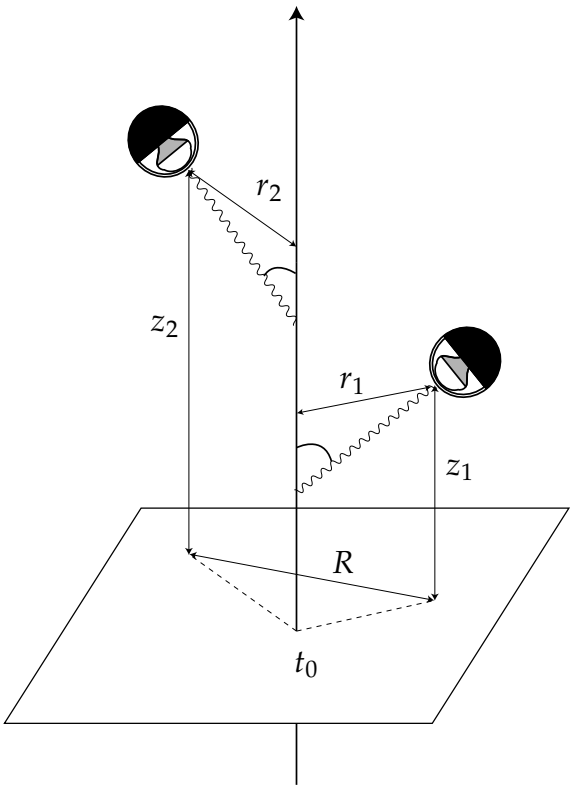

Figure 3.3: *Schematic view of a muon passing two optical modules.*

and thus the condition for two hits to be related becomes

$$-\kappa R + (z_j - z_i) \leq c(t_j - t_i) \leq \kappa R + (z_j - z_i) \tag{3.14}$$

This relation is more restrictive as the maximal time difference is determined by the the 2D distance between the PMTs. The distance along the assumed track direction is taken into account as the propagation time of the muon. In practice a safety margin of 20 ns is added, in order to account for effects of electronics, light scattering and inaccuracies in the alignment of the detector. The algorithm that is described below was designed to be applied to the first data taken with the Antares detector. In that phase, accurate alignment was not yet available. Therefore the safety margin is also used in the fit algorithm. With a more accurate alignment of the detector, the safety margin could be reduced.

An additional restriction when matching pairs of hits comes from the attenuation of the intensity of the Cherenkov photon flux. The photon intensity is described by formula 2.7. This means that most photons from the muon will be detected within a certain roadwidth from its path. By cutting on a maximum 2D distance between hits, the background of accidental coincidences will be reduced. As can be inferred from equation 3.14, the probability of an accidental coincidence increases with this distance. An additional condition is :

$$|r_j - r_i| < R_{max} \tag{3.15}$$

The value of R_{max} is usually set to a value corresponding to two attenuation lengths.

3.4 Track Reconstruction

For the fitting method that has been developed in this work, a selection of the hits is made using L1' hits and directional clustering. The fitting algorithm basically consists of three steps :

1. **Scanning**
   A scan over a part of the parameter space is made. For each point in the sub-space, a hit selection is made and the selected hits are used to make a prefit. The result is a set of prefits with associated hits.

2. χ^2 **fit**
   In this phase a χ^2 fit is made to determine final track parameters, using the prefits as start values. The hits which were selected in previous phase are used. Hits that are incompatible with the improved fit could be removed.

3. **Track Ordering**
   As, in general, the result is a set of track candidates, the tracks are ordered.

3.4.1 Scanning

The scanning phase is designed to tackle several problems inherent to the track fit. The first is the problem of the starting value. As the track fit is a non-linear problem (see equations 3.7 and 3.8), it has to be solved through an iterative process in which values for the track parameters are sought which maximize a likelihood or minimize a χ^2. Such a procedure requires a starting value for each of the parameters. However, it can be shown [77] that when assuming a direction, the determination of the remaining parameters can be reduced to a linear problem when only direct Cherenkov hits are considered. As a consequence, for each direction there is a unique solution for the position and time of the track. Another problem is the possibility of local maxima of the likelihood. This means that one can end up in a region of the parameter space where the derivatives of the likelihood are zero. Eventually, a local minimum could be considered as a solution. By scanning over the angular space, the local maxima are mapped out and no part of the phase space is missed. An important aspect of χ^2 minimisation, is finding the right hits. For this, the 1D clustering is used. To do the scan, the angular space (covering solid angle Ω) is divided in a grid with n_g points, distributed isotropically. This gives a set of points $G = \{(\theta_0, \phi_0), (\theta_1, \phi_1), ..., (\theta_{n-1}, \phi_{n-1})\}$. For each point, the directional clustering algorithm is applied to the L1' hits. This yields a cluster of L1's of size $n_{L1'}$. If $n_{L1'} \leq n_{par}$,with n_{par} the number of free parameters in the fit, this direction is rejected. Until now, only L1' hits are considered. These form a subset of the muon hits. Single L0 hits are not included. However, these form a significant fraction of the number of muon hits. In order to enhance the

hit yield, L0 hits are added to the sample. A L0 hit is added if it is causally related, assuming the given direction, with each selected L1' hit. Furthermore, the added L0's have to be causally related with each other. The total number of hits associated with a given direction is referred to as n_{tot}.

Prefit

In order to supply the following fitting steps with sufficient information, the position and time of the muon should be determined for each assumed direction. These quantities are estimated in several steps. Even though the problem is linear for a given direction, the estimation is done iteratively. The reason for this is that it allows the use of a *M-estimator* PDF. First, this takes care of a non 100% pure hit selection. Secondly, as the direction is quantized with a grid size Ω/n_g, the closest grid point can be some degrees away from the true track direction.

Linear approximation As a start, the position of the track is estimated by taking the average of the hit positions in space. From this, using the Cherenkov hypothesis, t_0 is calculated for each hit. The average of these values is used for the t_0 of the track. These two steps are repeated, but the hit coordinates perpendicular to the track are weighted using an estimated transverse distance.

Powell's Method Subsequently, the hit-time residuals are minimized using Powell's method ([58]). In short, this procedure carries out successive 1-dimensional gradient-less line-minimisations on a set of vectors in the 3-dimensional parameter space. This set of vectors is continuously optimized to achieve quick convergence, by including the vector difference between the previous point and the current point after each minimisation step.

Marquardt Method Previous procedures are used to get sufficiently close to the minimum of the function to be minimized. When this is the case, the function can be approximated by a quadratic form :

$$\chi^2(\vec{\theta}_{min}) \simeq \chi^2(\vec{\theta}_i) - (\vec{\theta}_{min} - \vec{\theta}_i) \cdot \nabla\chi^2(\vec{\theta}_i) + \frac{1}{2}(\vec{\theta}_{min} - \vec{\theta}_i) \cdot H \cdot (\vec{\theta}_{min} - \vec{\theta}_i) \tag{3.16}$$

Where $\vec{\theta}_i$ ($\vec{\theta}_{min}$) is the 3-vector containing the position and time at current iteration (minimum), $\nabla\chi^2(\vec{\theta}_i)$ its gradient and H is the Hessian matrix, containing the second derivatives. In this case, the minimisation can be made in all 3 dimensions simultaneously :

$$\vec{\theta}_{min} = \vec{\theta}_i + H^{-1} \cdot [-\nabla\chi^2(\vec{\theta}_i)] \tag{3.17}$$

This method can be applied when the Hessian matrix can be calculated analytically, which is the case for a χ^2 or *M-estimator* PDF. When far away from

the minimum or if the approximation 3.16 is not valid, only a step along the gradient can be taken :

$$\vec{\theta}_{new} = \vec{\theta}_i - constant \times \nabla\chi^2(\vec{\theta}_i) \tag{3.18}$$

The constant should be sufficiently small so as not to step over the minimum. Marquardt's method [58] uses a continuous steering parameter λ for which the value depends on the success of the last minimisation step.

Not all prefits yield equally good candidates. For reasons of efficiency in the following steps, an ordering of the prefits is helpful. The prefits can be sorted according to the number of associated hits N_{tot}. This is based on the assumption that for a direction close to the true direction, most hits should be found using the cluster procedure described above.

3.4.2 χ^2 Fit

The goal of the previous scanning phase is twofold. First it supplies a number of candidate directions, together with estimates of the position and time coordinates. Secondly, for each of the directions it includes a set of hits. In the final fit, also the direction is fitted, hence, the effect of the discretisation of the direction on the expected hit-time residual is no longer present. As a consequence, the fit is more demanding in terms of cpu-time. For performance reasons, the smallest clusters can be rejected. The largest number of associated hits is N_{max}. Only candidates with N hits are considered where $N > (1 - P_{Ncut}) \times N_{max}$. When the intrinsic time resolution is assumed in the calculation of the χ^2, the influence of impurities, or outliers, increases. This influence is twofold. First, outliers can pull the fit, so that the minimum of the χ^2 doesn't correspond to an accurate estimate of the track parameters. Secondly, events with outliers are more likely to be rejected on basis of their χ^2 probability, even though they can have a reasonable estimate of track parameters. In order to increase reconstruction efficiency and accuracy, the possibility to remove outliers is included. Outlier removal is attempted if the χ^2 probability of a fit is smaller than a value P_{min}. If the value of the probability is dominated by one or few outliers, removal of the outliers is beneficial. One outlier is removed at a time, and a fit is made with the remaining hits. The hit to be removed is the one contributing the most to the χ^2 and for which $\Delta t \geq n_{stdev} \times \sigma$. The number of standard deviations n_{stdev} is typically set to a value of 5. The final fitting procedure can be described as follows : First, the track parameters are fitted using a M-estimator PDF. Secondly, the χ^2 probability is calculated and, if it is below P_{min}, hit removal is attempted, until either the probability exceeds P_{min} or the maximum number of hits has been removed or no hit can be removed.

3.4.3 Track Selection

In the final step all parameters are left free to be estimated. Therefore the possibility exists that fits with different starting values from prefits converge to approximately the same solution. These tracks are identified as identical if the difference is less than some degrees. This value should be in the order of the final angular resolution of the fitting procedure. The collection with identical solutions is then sorted based on number of hits, and χ^2. For a given direction, the fit with the largest number of hits is preferred. If there are multiple solutions with the same number of hits, the one with the smallest χ^2 value is taken. The final result consists in the general case of multiple solutions. As mentioned earlier, multiple solutions are a consequence of symmetries in the topology of the event and the detector geometry. In general, ambiguities can not be excluded. The way to handle these depends on the kind of analysis. One way is to exclude events that have multiple solutions. This, of course, affects the detection efficiency, as it will cut away signal and introduce a bias. The other option is to keep these events and to take the solution that is most likely, according to some criterion. This is similar to commonly used reconstruction procedures which try to find a single solution. An interesting option is to use all solutions for point-source searches.

3.4.4 1 Dimensional case

A special case occurs when all the hits lie on a straight line. This is the case when hits are recorded on a single detector string. This implies a rotational symmetry around that axis. Consequently, the ϕ angle cannot be determined from the data. There is no need to scan over ϕ, and it can be set to a fixed value, arbitrarily chosen to be 0. There is now one parameter less to be fitted. This special case will be treated more in-depth in chapter 4.

3.5 PDF fit

In the described fit procedure the philosophy is to select those hits with a high purity with respect to the Cherenkov hypothesis. The ultimate fitting procedure should include all available information and thus use all hits. In order to asses the full potential of the reconstruction, a designated PDF fit can be done. So, the reconstruction algorithm described until now, ScanFit, acts as input to this fit. The PDF that is used has been developed in [74] and is implemented in the final fitting stage of the full reconstruction procedure. This PDF describes the probability for a hit-time residual Δt. Two additional effects are taken into account :

1. The rate of random background hits with amplitude a is given by $R^{bg}(a)$. In order to be able to normalize the PDF, only a finite time window is considered. The random hits are assumed to be distributed uniformly between

$-T/2$ and $T/2$, and each value of Δt is thus equally probable. The value of T is chosen large enough to contain all the signal hits. It typically amounts to 500 ns.

2. The PDF for the signal hits describes the distribution of the time residual Δt between the arrival time of a detected photon and a hypothesized Cherenkov photon. The PDF also includes effects from other processes like electro-magnetic showers. The PDF depends on the amplitude a of a hit. The probability of measuring a residual Δt is then expressed as $P^{sig}(\Delta t|a)$.

The relative contributions of the signal and background probabilities depend on several quantities. The main two quantities are the distance traveled by the photon to the optical module (d), and the angle of incidence of the photon on the optical module (α). These quantities can be determined from the track parameters, assuming the photon is emitted at the Cherenkov angle. The expected number of signal hits for a given amplitude $N^{sig}(\alpha, d|a)$ depends on these quantities. This value, together with the expected number of background hits is used to weight the time residual probabilities :

$$P(\Delta t|\alpha, d, a) = \frac{P^{sig}(\Delta t|a)N^{sig}(\alpha, d|a) + R^{bg}(a)}{N^{sig}(\alpha, d|a) + R^{bg}(a)T} \tag{3.19}$$

where the denominator corresponds to the expected total number of hits. $N^{sig}(\alpha, d|a)$ can be factorized in two different components, the expected number of hits which depends on distance and a factor describing the angular acceptance of the optical module, which depends on the angle of incidence :

$$N^{sig}(\alpha, d|a) = N(d|a) \times f(\alpha|a) \tag{3.20}$$

Both terms are obtained by fitting an appropriate function to the distributions obtained from simulations that include light scattering, shower processes etc. These distributions are made for different bins of amplitude. The chosen bin edges are $0, 1.5, 2.5, 5, 10$ and ∞ photo-electrons. For a detailed description of the distance and angle parameterisations, see [74]. Due to the amplitude dependence of the TTS of the PMT, there is a relation between the shape of $P^{sig}(\Delta t|a)$ and the variables d and α. However, $P^{sig}(\Delta t|\alpha)$ is not explicitly dependent on these two variables. The relation is implicitly taken into account by dividing both $P^{sig}(\Delta t|\alpha)$ and $N^{sig}(\alpha, d|a)$ into the same bins of amplitude. The muon energy has been integrated over.

Hit-Time Residual PDF

The likelihood as defined in formula 3.1 assumes uncorrelated hit probabilities. However, this is not necessarily the case. When the duration of the photon flux on a PMT exceeds the integration gate of the ARS, the second ARS takes over,

and a second hit is recorded (see section 2.6.3). In this case, the second hit is correlated with the first one and doesn't contain extra information. These second ARS hits cause the additional, off-zero peak in the hit-time residual distribution. The original $P^{sig}(\Delta t|a)$ doesn't account for this correlation and all hits are used in the calculation of the likelihood of the fit. On the other hand, a parameterisation for $P^{sig}(\Delta t|a)$ was made which ignores the double peaked structure. The reason for this was to avoid additional local minima in the likelihood. The parameterisation describes $P^{sig}(\Delta t|a)$ for a given amplitude bin, by a single Gaussian peak and a tail, parameterised as $C_{tail}e^{-\Delta t/\eta}/(\Delta t + \rho)$. The peak and tail are joined by a third-power polynomial in the range $c_1 \leq \Delta t \leq c_2$, requiring that the function is continuous and differentiable at the points c_1 and c_2. Including c_1 and c_2, the total number of free parameters in the function is 12. The values of the parameters are determined by fitting the function to normalized distributions of time residuals, obtained from a simulation of the detector response.

In this work, a different approach has been made in order to remove the above mentioned correlation. This is done by removing the hits that are recorded in the second ARS immediately after the integration gate of the first closes. This is accomplished by introducing a virtual dead-time after each hit, with a duration somewhat larger than the ARS integration gate. The above described parameterisation $P^{sig}(\Delta t|a)$ is then fit to the new distributions. The resulting distributions for the different amplitude bins are shown in figure 3.4. It can be seen from figure 3.4 that the peak due to the second ARS hits has disappeared, though a small remnant can be noticed. The peak at zero is unaffected by the dead-time, and the fits are generally very good.

3.6 Performance

In this section the performance of the reconstruction algorithm will be summarized. As explained above, the algorithm is divided in several phases. The behavior of each of these phases is presented separately. The combined result will also be given. The performance is tested on simulated data, so that the true values of the parameters to be estimated are known. An important parameter to measure is the pointing accuracy of the telescope. To measure the pointing accuracy, a quantity is introduced :

$$\Delta a_\mu = \cos^{-1}(\hat{d}_\mu^{true} \cdot \hat{d}_\mu^{fit}) \tag{3.21}$$

With $\hat{d}$ as defined in section 3.2. It measures the angular error between the true muon and the reconstructed muon (3.21). The data set consists of muons originating from upward going neutrinos. The neutrinos were generated with an energy spectrum $\frac{dN}{dE} \propto E^{-1.4}$ in the range from 10 GeV to 10^7 GeV. The detector response depends on the energy of the muon. Therefore, some quantities are presented as a function of the muon energy. A study on the effect of the random background

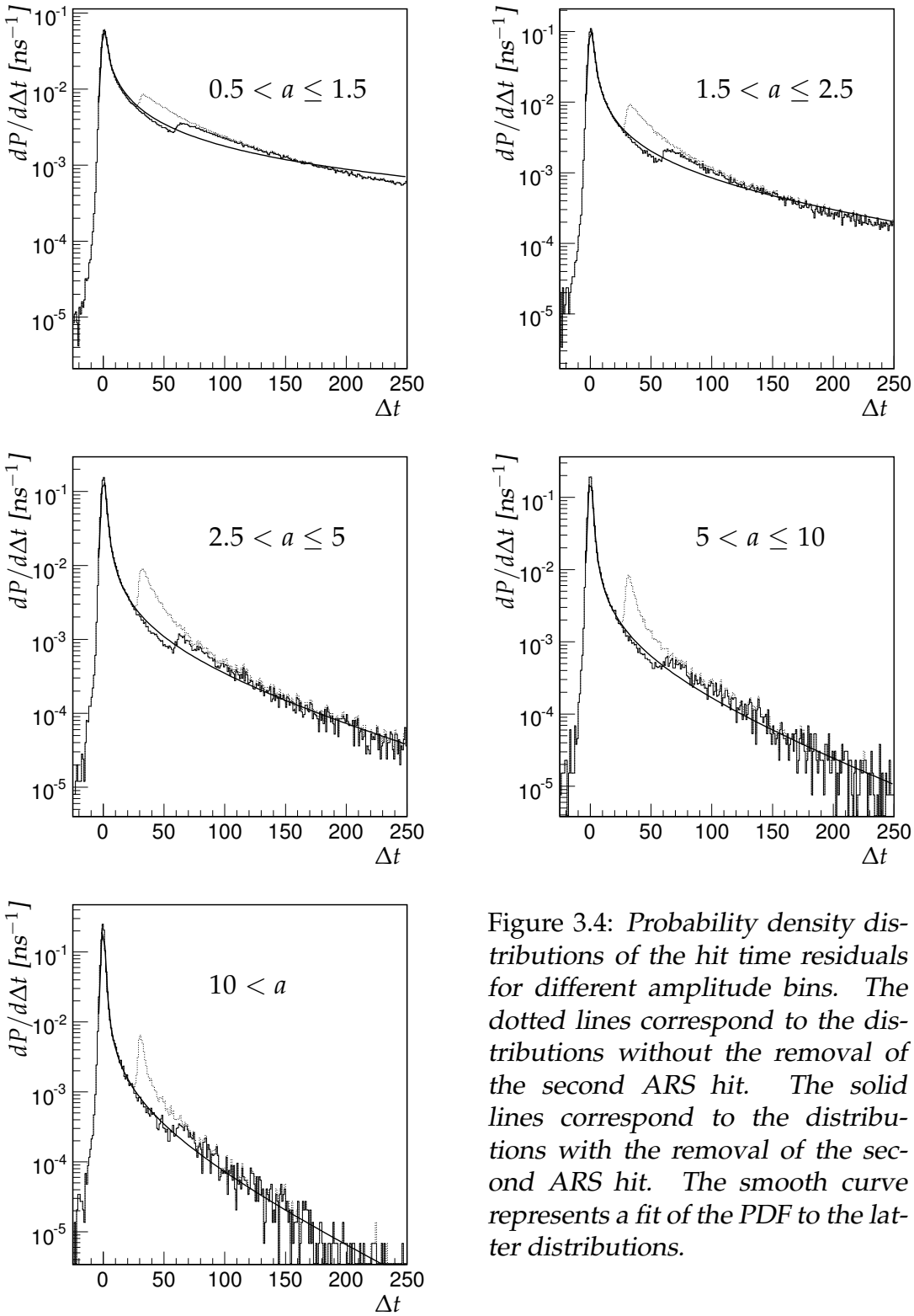

Figure 3.4: *Probability density distributions of the hit time residuals for different amplitude bins. The dotted lines correspond to the distributions without the removal of the second ARS hit. The solid lines correspond to the distributions with the removal of the second ARS hit. The smooth curve represents a fit of the PDF to the latter distributions.*

is included. For this purpose three levels of background are considered : 60 kHz, 120 kHz and 240 kHz. This largely covers the background observed so far. For some studies, the hypothetical case of no background is also included.

3.6.1 Hit Selection

As described in section 3.3, the selection of hits is based on a 1-dimensional causality criterion. In order to enhance purity a maximum transverse distance between two hits is imposed. In figure 3.5 the distributions of the transverse distance are shown. With increasing rates, the contribution of background to the L1' sample increases at larger distances. The reason for this can be found in formula 3.14. The allowed time interval increases with distance, and so does the probability for two random hits to coincide. Also, the effect of using L1'-hits can be seen by comparing the left and right plots. When using the L1'-hits, the obtained distributions overlap up to 90 meters, which represents 85 % of all signal hits. When using L0's the distributions differ significantly. A maximal value of the transverse distance has been introduced in section 3.3.1. Due to the geometry of the detector, the number of PMTs contained in a cylinder with radius R depends on the zenith angle θ. This is taken into account by making the value of R_{max} depend on the zenith angle :

$$R_{max}(\theta) = R_{max} \times (1 - 0.25\cos^2(\theta)) \tag{3.22}$$

The value of R_{max} is set to 90 meters.

Purity and Efficiency

The purity and efficiency of the hit selection determine the quality of reconstruction. The main reason for this is that the background is not modeled in the χ^2 fit. The purity of the hit-selection is defined as the fraction of the selected hits that is truly caused by a muon. A purity of 1 (or 100 %) indicates that no background hits are included. No distinction is made between photons due to Cherenkov light or due to electro-magnetic showers. The efficiency is defined as the ratio of the number of storeys in the selection and the total number of storeys that recorded a photon from the muon. It is defined in this way because at most one hit from a storey is used. Figures 3.6 and 3.7 summarise the purity and efficiency of the hit-selection in the simulated sample. Both the purity (figure 3.6, left) and the efficiency (right) are found to be independent of zenith angle. This supports the definition of $R_{max}(\theta)$ given in equation 3.22. Both purity and efficiency depend on the background rate, as can be expected. At 240 kHz the overall purity of the sample is above 90% and at 120 kHz above 95%. The overall efficiency remains above 40%. The maximum efficiency is about 50 %. When considering the muon energy dependence of both the purity (figure 3.7, left) and efficiency (figure 3.7,

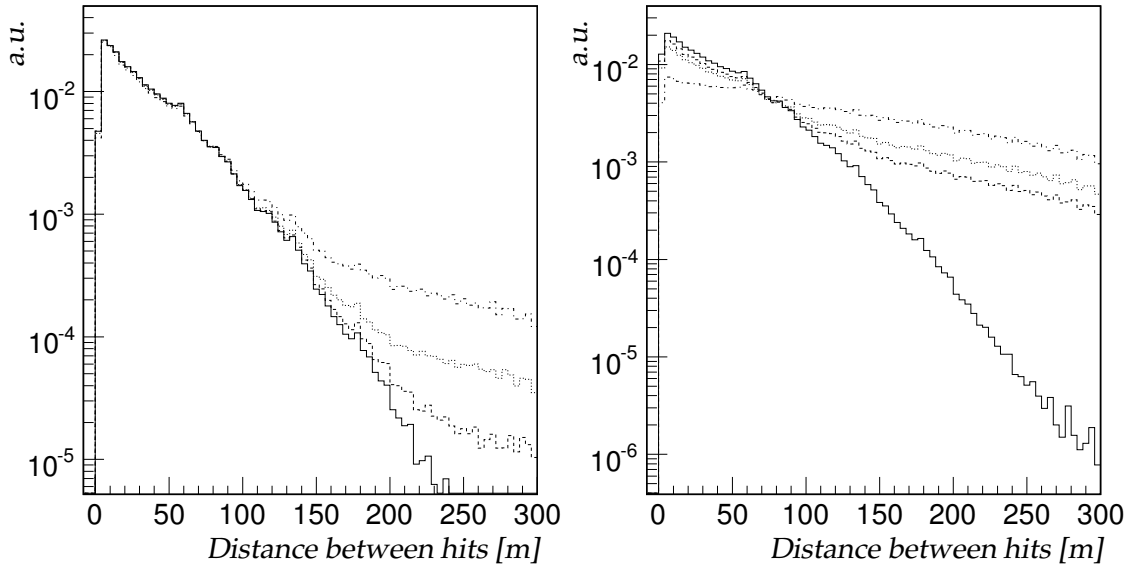

Figure 3.5: *Distributions of transverse distances between pairs of hits, corrected for phase-space effects. Left plot shows the distribution for L1′ hits, the right plot shows the distribution for the remaining L0 hits. Line type indicates background rates. The solid line represents no background. The dashed line represents a background rate of 60 kHz, the dotted line 120 kHz and the dash-dotted line 240 kHz.*

right), larger differences are observed. For any background rate, the purity decreases toward lower energies, and increases with increasing energy. The purity exceeds 95% for energies in excess of 100 TeV. The efficiency without background drops from about 70% at 10 GeV to just above 20% at 10 PeV. The explanation for this strong energy dependence lies in the increased photon yield with increased energy. On one hand it increases the purity, as the relative contribution of background hits decreases. On the other it decreases the efficiency as the additional hits more likely originate from electro-magnetic showers. These hits do not always satisfy the 1D causality criterion. The dependence of the efficiency on the background rate at low energies is caused by the interference of background hits which can cause signal hits to be rejected.

When the assumed muon direction deviates from the true muon direction, less hits are expected to be causally related. This affects the efficiency of the hit-selection. This loss in efficiency manifests itself in two ways. The first is a reduction of events which have enough hits to make a (pre)fit. The second is a general reduction of the number of hits. Both effects are studied as a function of the deviation of the assumed muon direction from the true muon direction.

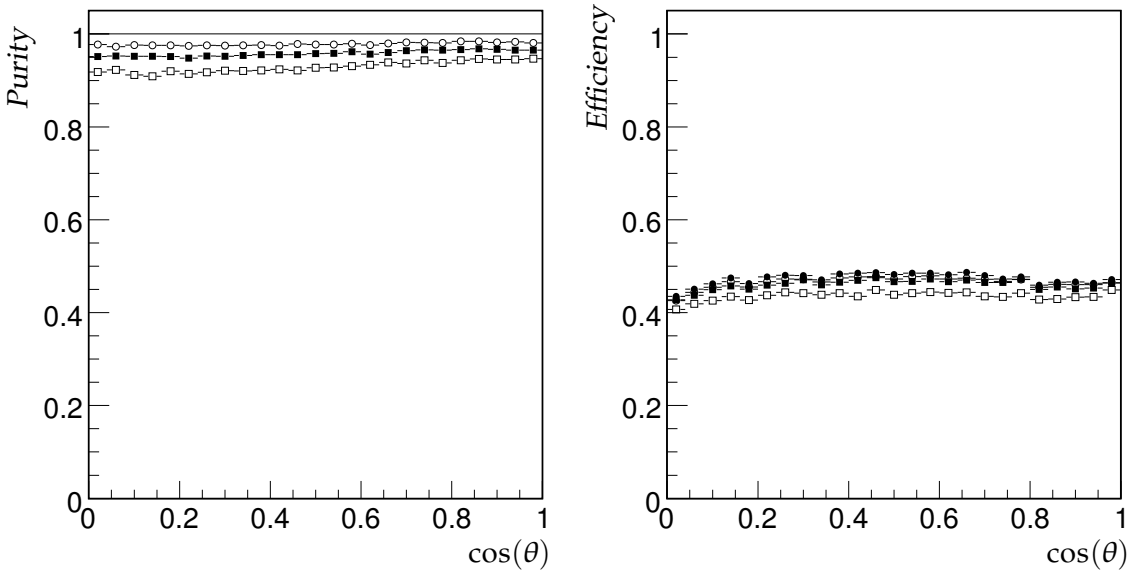

Figure 3.6: *Left : The purity of the hit selection as a function of the cosine of the zenith angle of the muon direction. Right : The efficiency of the hit selection as a function of the cosine of the zenith angle of the muon direction. The solid line is without background, the open circles indicate a background of 60 kHz, the closed squares indicate a background of 120 kHz and the open squares indicate a background of 240 kHz.*

The results are summarised in figure 3.8. The reconstruction efficiency is defined as the fraction of the total events that has sufficient hits ($\geq$ 5) for a (pre)fit. The hit selection efficiency is defined as the fraction of hits that remain. Up to 20 degrees, the reconstruction efficiency shows a plateau at about 95 %, while the hit-efficiency (figure 3.8, right) shows a large negative gradient. In this region, the fit quality is expected to decrease due to the reduction of the number of hits. Above 20 degrees, the reconstruction efficiency begins to fall, and the drop in the hit efficiency begins to flatten. This implies that the events that survive have just enough hits.

Hit time residuals

As mentioned earlier, the goal of the hit selection is to increase the purity with respect to the assumed muon hypothesis. This includes suppressing the late hits from the electro-magnetic showers and the hits from the continuous background. In the previous section, the purity with respect to the background and efficiency has been evaluated. This was done without making a distinction between the

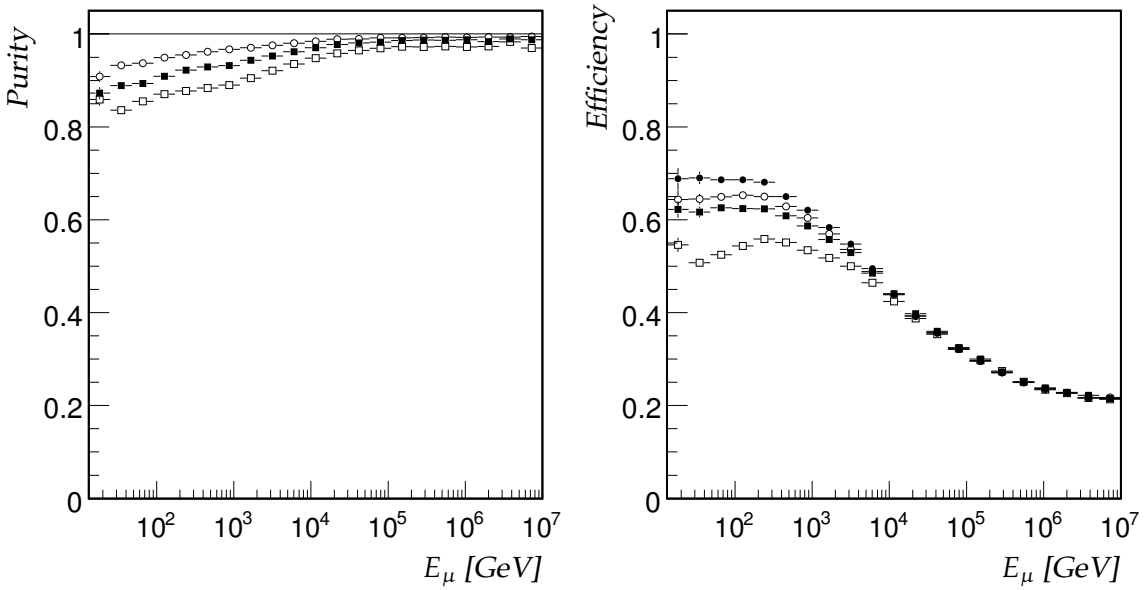

Figure 3.7: *Left : The purity of the hit selection as a function of the muon energy. Right : The efficiency of the hit selection as a function of the muon energy. The solid line is without background, the open circles indicate a background of 60 kHz, the closed squares indicate a background of 120 kHz and the open squares a background of 240 kHz.*

origin of the hit, which could be either direct Cherenkov or an electro-magnetic shower. When considering only direct Cherenkov light from a muon, the latter contribution should be suppressed as well. The tail of late hits should then decrease and the overall distribution should become more Gaussian. This aspect of the hit selection has been studied by comparing hit time residual distributions before and after the hit selection. In order to disentangle the effects of background and muon energy, the comparison is done for the different background rates and muon energies. The contribution of hits in the second ARS peak is suppressed by favoring the first L1 trigger in an LCM, be it either a coincident pair or a high amplitude hit. This is done by introducing a virtual dead-time after a L1 trigger, with a duration larger than the ARS integration gate. Figure 3.9 shows the distributions of time residuals for various conditions. The energy ranges are 10 GeV - 1 TeV, 1 TeV - 100 TeV and 100 TeV - 10 PeV. These ranges are chosen to represent a regime with low contribution from showers, the onset of a significant shower contribution and a shower dominated regime, respectively . In each plot, the distribution of hit time residuals before selection and after selection is shown. The latter corresponds to the hit sample that is used for the prefit and the subsequent χ^2 fit. Both distributions are normalized to retain the relative probabilities. The

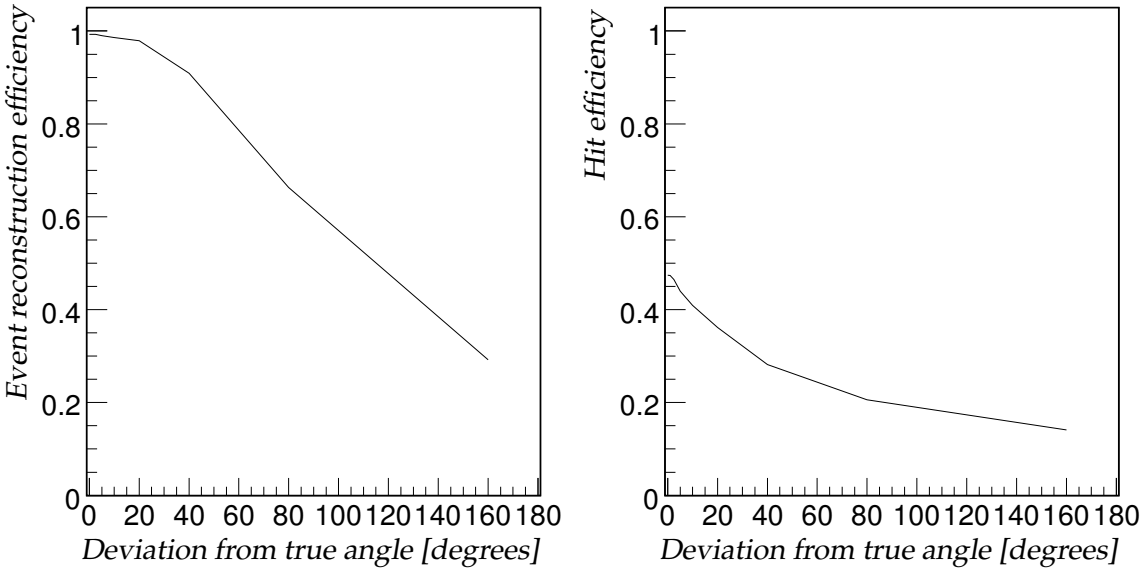

Figure 3.8: *Left : Efficiency to reconstruct an event as a function of the deviation of the assumed angle from the true muon angle. Right : Hit collection efficiency as a function of the deviation of the assumed angle from the true muon angle*

difference at a given residual is equal to a reduction of hits. As can be seen from figure 3.9 the tail of the distribution is suppressed, and the distribution resembles more closely a Gaussian distribution by making a hit selection. A feature is the increasing contribution of the second ARS peak with increasing rate. This is most clearly seen at the highest energies. This effect occurs even though the first hits are selected. It is due to the increased probability of a random hit preceding a high amplitude hit that triggered the L1. The probability of a high amplitude L1 trigger increases with muon energy due to the increase of the photon yield from more energetic electro-magnetic showers.

3.6.2 Scanning

This section gives a summary of the scanning phase (section 3.4.1) of the reconstruction algorithm. Scanning over the angular space allows the selection to be applied to the hit sample. It also allows identification of some solutions as local rather than absolute χ^2 minima. Examples of several scans are shown in figures 3.10, 3.11 and 3.12. For each event, the number of hits that are found by the directional clustering algorithm and the negative logarithm of the χ^2 per degree of

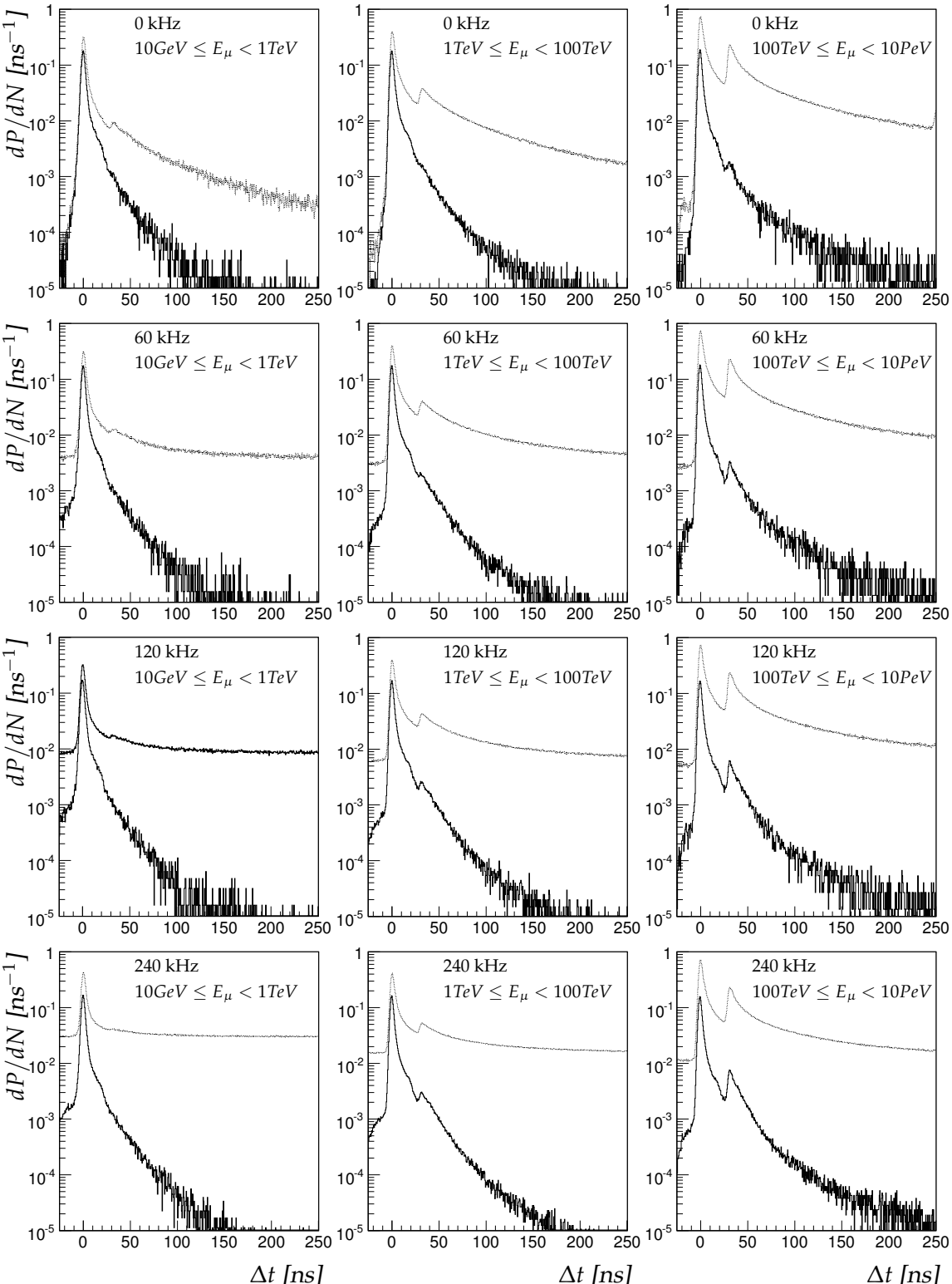

Figure 3.9: *Distributions of hit time residuals for different background rates and muon energy ranges. Each plot shows two lines, the top line is before hit selection, the bottom one is after hit selection.*

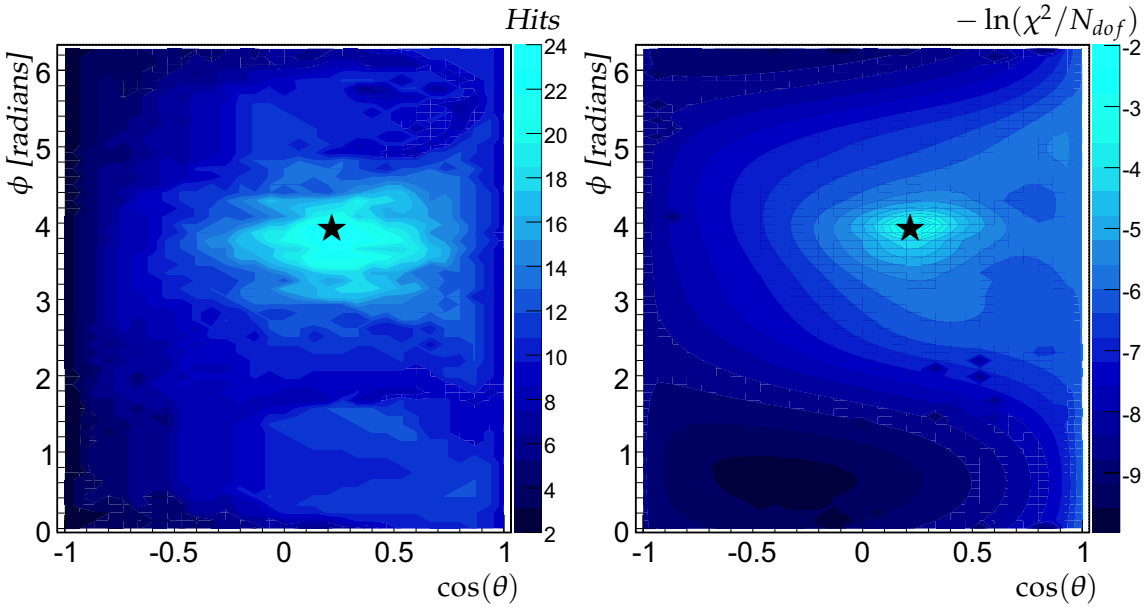

Figure 3.10: *Scan of the angular space for a 64 TeV muon. Left : number of associated hits. Right :* $-\ln(\chi^2/N_{dof})$*. The mark ★ : true track direction.*

freedom[1] is shown as a function of the direction. The χ^2 is obtained by making a fit with the angles fixed according to the given directions. The hits used in this fit are all the hits that caused the event to be triggered. The hit selection is omitted. In this way, the plots represent the landscape in which a χ^2 fitting procedure without hit selection should find a minimum. From figures 3.10, 3.11 and 3.12, some common observations can be made. The regions of the angular space in which the maximum number of hits could be found show a correlation with the true values of the track parameters. The existence of several disconnected local minima of the χ^2 values can be recognised.

It is expected that the direction in which the maximum number of hits (N_{max}) can be found using the hit selection procedure is close to the true muon direction. The angular residual between the true muon direction and the direction with N_{max} hits is shown in figure 3.13 as a function of scanning grid size ω/N_g (see section 3.4.1). If multiple solutions with N_{max} hits are found, the one with smallest residual is taken. It can be seen that the angular residual depends almost linearly on the grid size. The value for a scanning grid of 5 degrees is 5 degrees for an assumed background of 60 kHz. The actual resolution of the scanning phase is in general better than that due to the fact that the direction closest to the true direction can have a smaller number of associated hits.

[1]The negative logarithm of the χ^2 is taken to make the comparison with the contour plots. The logarithm reduces the dynamic range. The negation makes sure that a higher value corresponds to a 'better' χ^2.

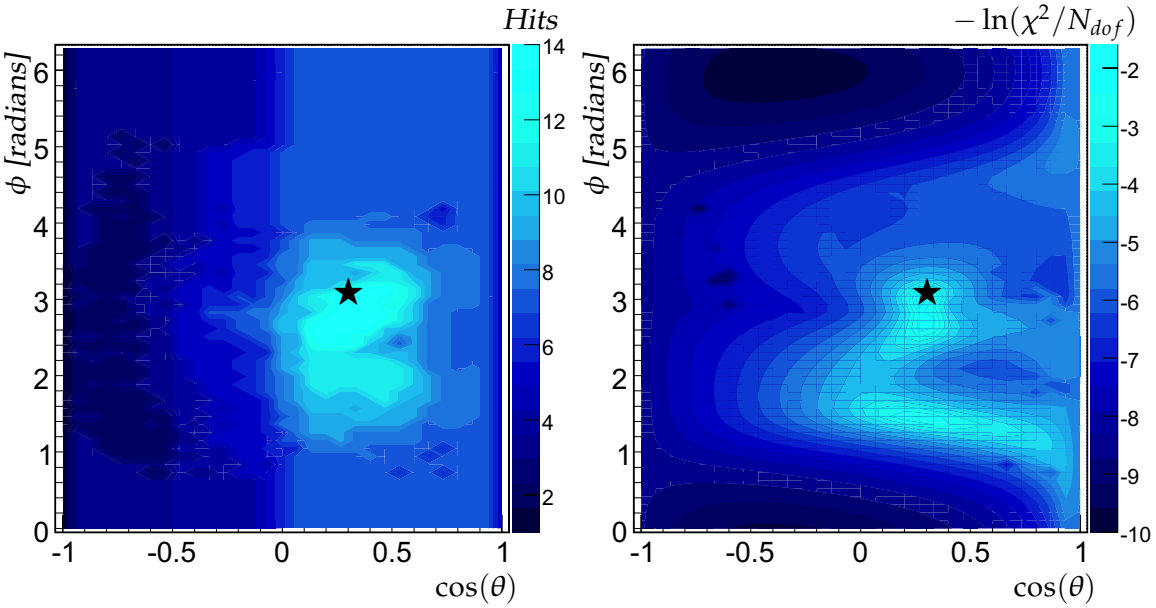

Figure 3.11: *Scan of the angular space for a 1.4 TeV muon. Left : number of associated hits. Right :* $-\ln(\chi^2/N_{dof})$*. The mark ★ : true track direction.*

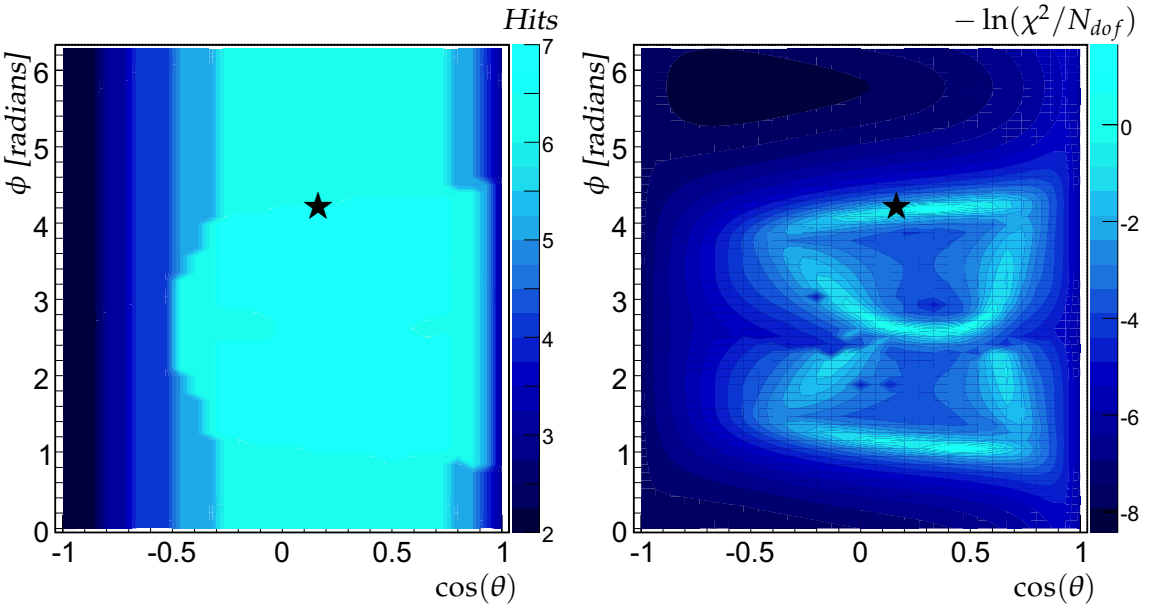

Figure 3.12: *Scan of the angular space for a 3 TeV muon. Left : number of associated hits. Right :* $-\ln(\chi^2/N_{dof})$*. The mark ★ : true track direction.*

The correlation between the number of associated hits and the probability of being close to the true direction can be used to speed up the further steps in the reconstruction. This can be done by excluding candidate directions with $N < (1 - P_{Ncut}) \times N_{max}$ hits from further steps (see section 3.4.2). The only parameter in this selection is P_{Ncut}, the fractional reduction of hits with respect to the maximum. The remaining fraction of candidate directions is shown in figure 3.14 for a grid size of 5 degrees at 60 kHz. The effect of this cut on the angular residual, calculated using the solution closest to the true direction, is also shown in figure 3.14. The value of P_{Ncut} used in this work is 0.2, which results in an average rejection of about 60% of the candidates while increasing the angular residual by about 10 %.

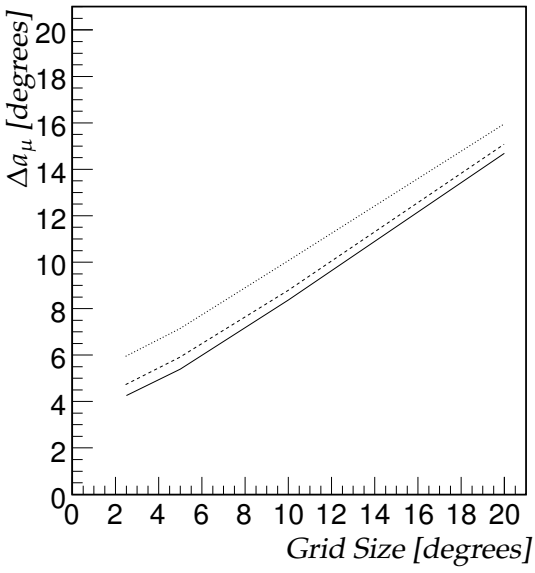

Figure 3.13: *Median of the angular residual Δa_μ as a function of the grid size used for scanning. The solid line corresponds to a random background of 60 kHz, the dashed line to 120 kHz and the dotted line to 240 kHz.*

3.6.3 χ^2 Fit

This section describes the χ^2 based fitting procedure. In this fit, the angles of the muon direction are added as additional free parameters.

Hit Removal

In the χ^2 fit, possible outliers can be removed iteratively, following a procedure described in section 3.4.2. The maximum allowed number of removed hits is defined a priori as a fraction of the total number of hits selected for the χ^2 fit and is referred to as f_r. The fraction of the number of fits with a χ^2 probability larger than 1 % has been studied as a function of the value of f_r. The χ^2 probability is calculated assuming a time resolution of $\sigma = 1.75$ ns for all hits. A hit is considered an outlier if $|\Delta t|/\sigma > 5$. This is done for a sample without background.

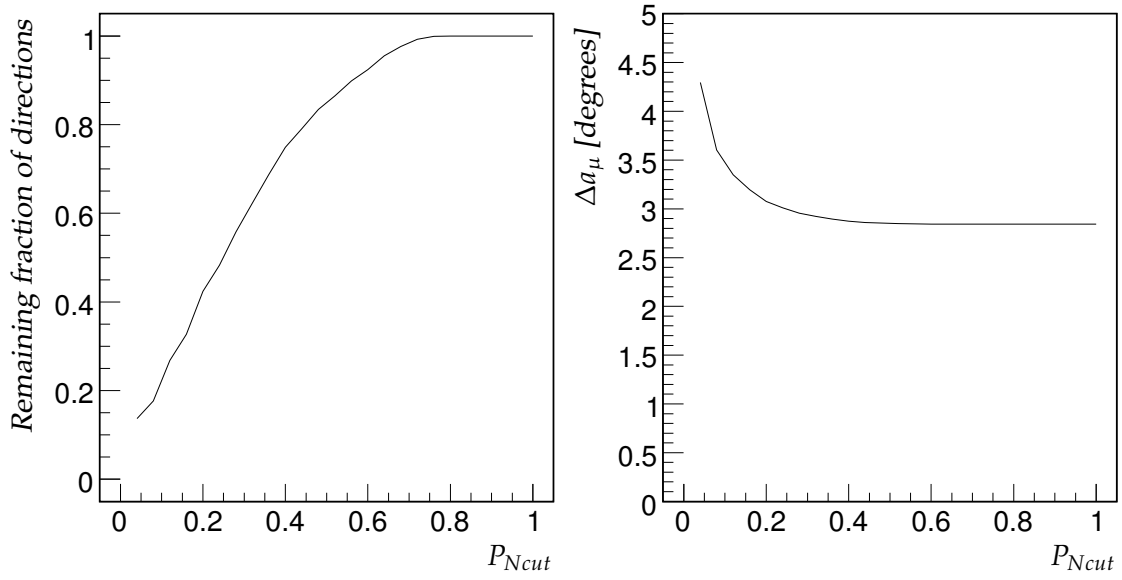

Figure 3.14: *Remaining fraction of candidate directions (left) and angular residual (right) as function of P_{Ncut}. P_{Ncut} is defined in the text..*

Figure 3.15 shows this relation. Allowing 10 % ($f_r = 0.1$) of hits to be removed increases the yield of the number of fits with a χ^2-probability larger than 1 % from about 40 % to 65 %. The value for f_r has been set to 0.2.

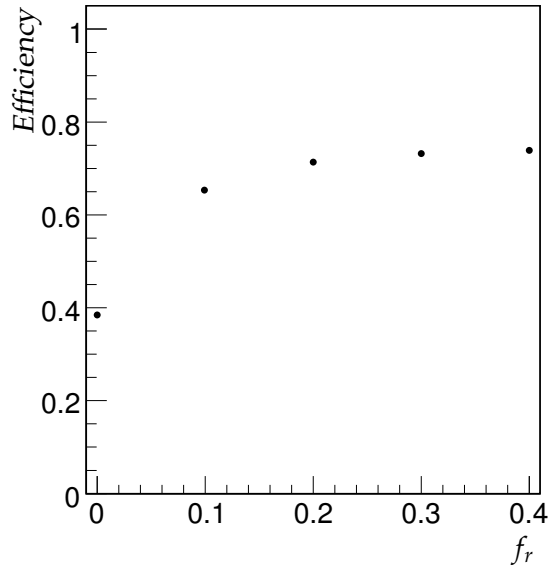

Figure 3.15: *Efficiency as function of the maximum fraction of hits allowed to be removed. The efficiency is defined as the fraction of events with a χ^2 probability $> 1\%$.*

Accuracy

The χ^2 fit includes all five track parameters in the optimisation process, including the angles which in the prefit were fixed. The error on the angle of the prefit passed on to the χ^2 fit can be controlled to some extent by the number of directions considered at the start. The probability of finding track parameters close to the true ones depends on the starting values. When there is a minimum of the χ^2 at the true parameter values, it is more likely to be found when the starting parameters are close to the true ones. How close the starting parameters have to be for a correct convergence has been investigated. The measure considered for this study is the angular residual. The χ^2 fit is started at different angles with respect to the true direction. The track is then rotated around the position of the track closest to the center of gravity of the hits. Figure 3.16 summarizes the results. As can be seen from figure 3.16, the angular residual is largest at low energies, especially below 100 GeV. This is due to the small number of hits that can be used for the reconstruction. Also, the angular residual tends to increase a bit at higher muon energies. This can be attributed to the contamination of hits in the tail of the time distributions. A cut in the χ^2 probability is expected to improve in the regions of high energy. At high rates (120 and 240 kHz) many of the fits which start close to the true values (0 and 1 degree) do not converge to the true direction. The high background rates clearly limit the angular resolution. In summary, the χ^2 fit typically improves the angular resolution from 2.5 degrees to 1 degree.

3.6.4 Full PDF Fit

Likelihood Values

In the full PDF fit, the estimators of the track parameters are those values which maximize the logarithm of the likelihood $\ln(L)$ (see section 3.1). The value of the likelihood at its maximum scales with the number of degrees of freedom involved. In order to account for this, the log-likelihood per degree of freedom, $\ln(L)/N_{dof}$ is used. This quantity is found to be effective in selecting good quality tracks as shown in reference [74].

The value of the likelihood at the true track parameters is referred to as L_{true}. If a maximisation of the likelihood is started at the true track parameters, then, in the limit of an infinite number of uncorrelated data points, it should find no better value than L_{true}. The convergence of the full PDF fit has been studied. This study was done for signal exclusively, no random background was added. The true track parameter values were taken as the start values of the likelihood maximisation. The value of the likelihood after the maximisation is referred to as L_{fit}. Figure 3.17 shows the distribution of $\ln(L_{fit})/N_{dof} - \ln(L_{true})/N_{dof}$. The contributions to the histogram from fits with different numbers of hits in the fit are indicated separately. It can be seen from figure 3.17 that in general the value of $\ln(L_{fit})/N_{dof} - \ln(L_{true})/N_{dof}$ is larger than the expected value of 0. This means

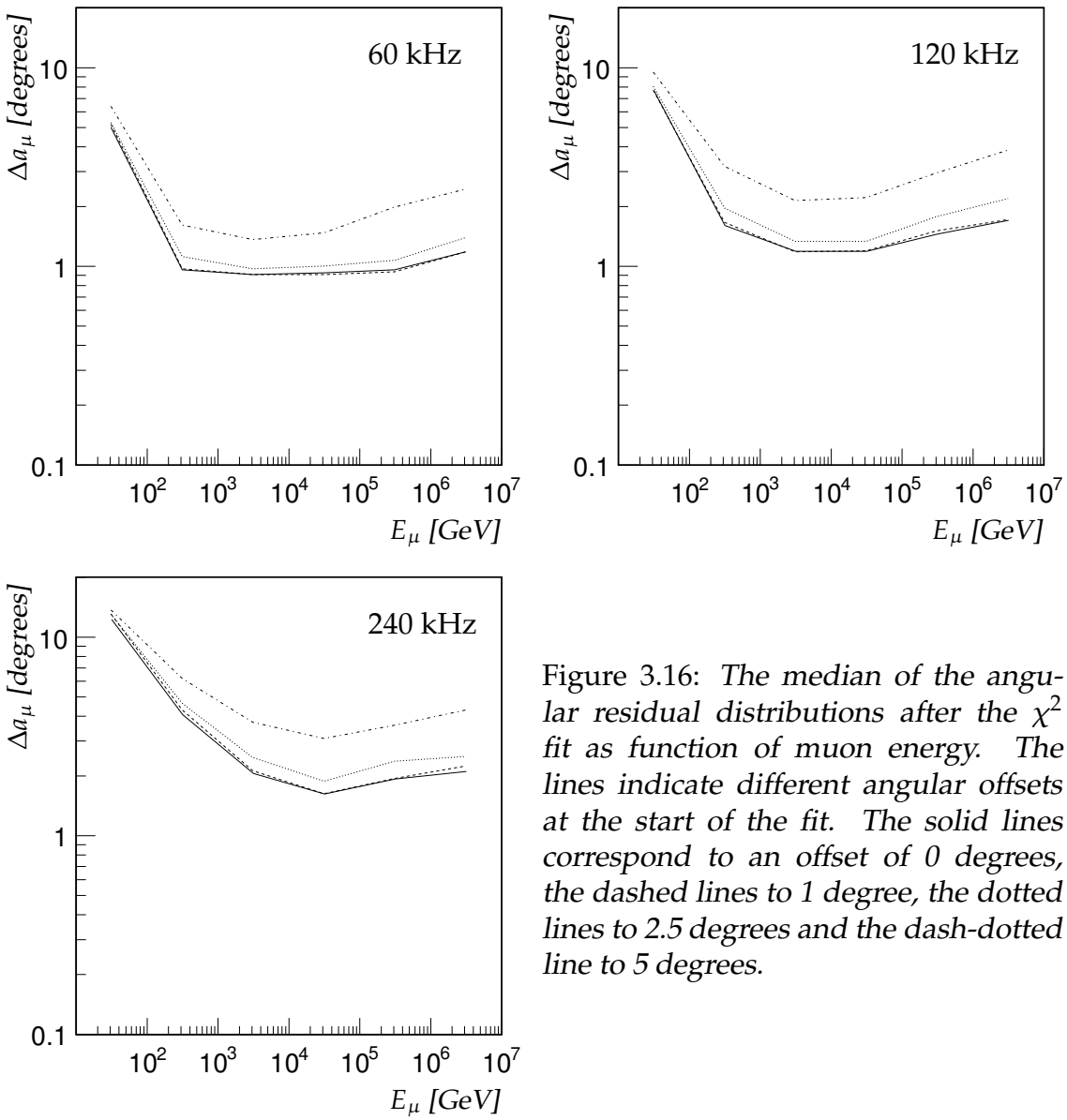

Figure 3.16: *The median of the angular residual distributions after the χ^2 fit as function of muon energy. The lines indicate different angular offsets at the start of the fit. The solid lines correspond to an offset of 0 degrees, the dashed lines to 1 degree, the dotted lines to 2.5 degrees and the dash-dotted line to 5 degrees.*

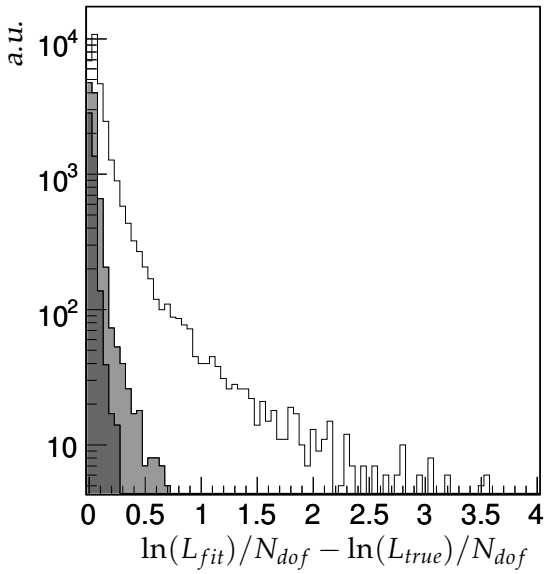

Figure 3.17: *Distribution of* $\ln(L_{fit})/N_{dof} - \ln(L_{true})/N_{dof}$. *The white distribution contains all events. The gray distribution contains events for which more than 75 hits were used to reconstruct the track. The dark gray distribution contains events in which more than 150 hits were used to reconstruct the track.*

that a maximum of the likelihood could be found that is larger than the truth. With an increasing number of hits used in the fit, the condition of infinite data is approached and the tail decreases. The extent of the tail is not solely determined by the statistical fluctuations at small numbers of hits. The larger values, $\ln(L_{fit})/N_{dof} - \ln(L_{true})/N_{dof} > 0.5$, are dominated by events which contain a set of correlated hits for which the measured time deviates from the expected time. Two distinct cases can be found. First are the events containing a large fraction of hits from an electro-magnetic shower occurring along the muon track. Figure 3.18 displays such an event. As can be seen in figure 3.18, a large fraction of the hits arrives later than the expected time. These hits are identified as originating from an electro-magnetic shower. The second case concerns events in which two muons cause a detectable signal in the detector. In figure 3.19, a simulated event is shown in which one muon originates from the charged-current neutrino interaction, and an other from a pion decay. The pion was created in the charged-current interaction.

The present PDF doesn't explicitly depend on the energy of the muon. It is clear though, that the hit time residual probability P^{sig} depends on the energy, as can be seen for example in figure 3.9. What can also be seen from this figure is that there is an interplay between the background and the contribution of the second ARS peak. At higher background rates, there is a higher probability that a signal hit ends up the second peak, because an earlier background hit caused the first ARS to make a hit. This relation is not taken into account, as the P^{sig} is modeled independently from the background rate. The modified P^{sig} as developed in this work describes the hit-time residual distribution better than the original, as can be seen from figure 3.4. A special feature is the decreased sensitivity to the correlated second ARS hits. The modified PDF is thus expected to perform better for a larger

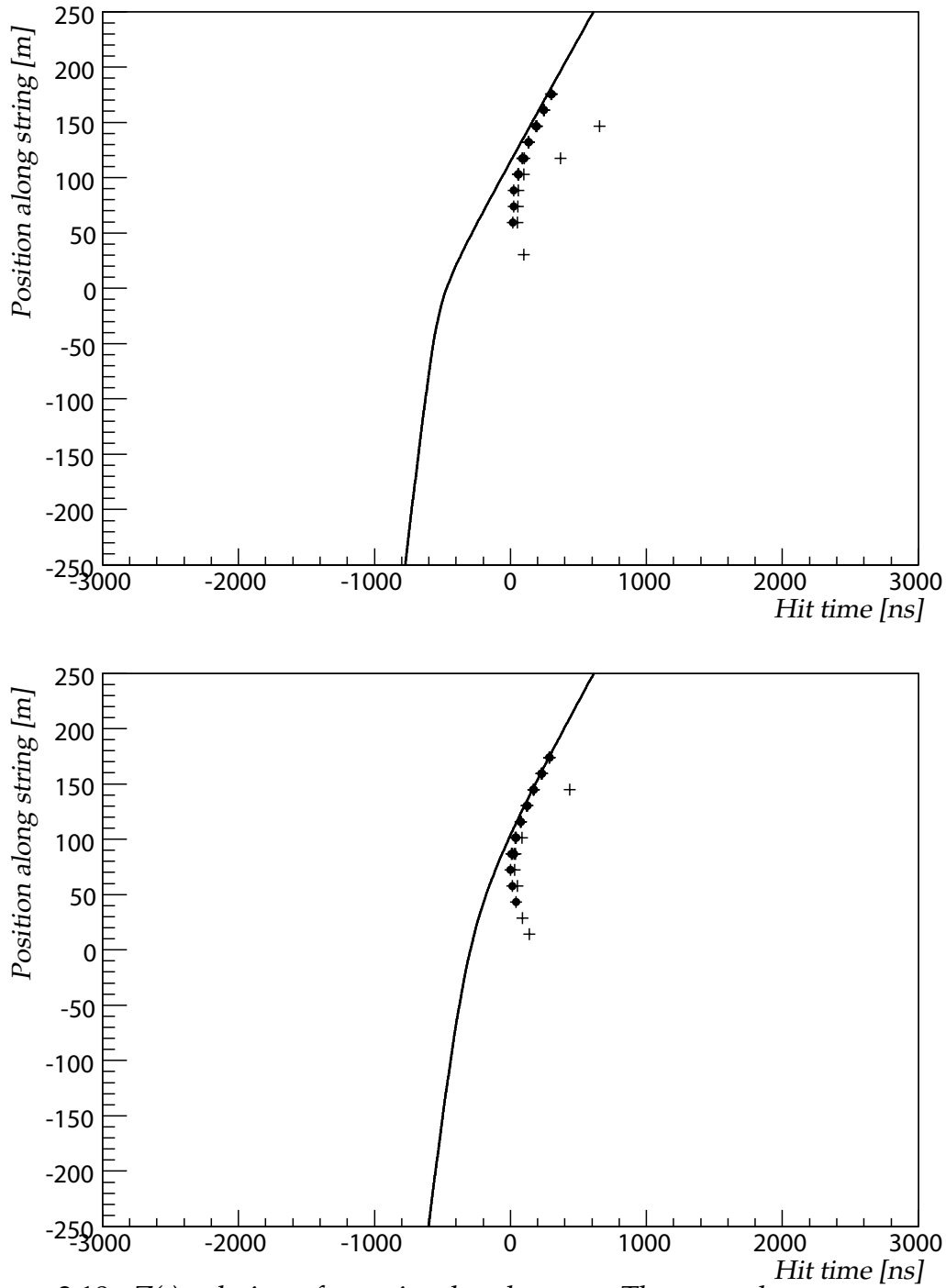

Figure 3.18: *Z(t) relations for a simulated event. The two plots correspond to different detector lines. The top plot corresponds to line 1 and the bottom to line 2 (see figure 2.8). The solid lines correspond to the expected arrival times of Cherenkov photons. The black dots and crosses are hits that originated from an electromagnetic shower occurring along the muon track. The black dots are the hits that caused the event to be triggered.*

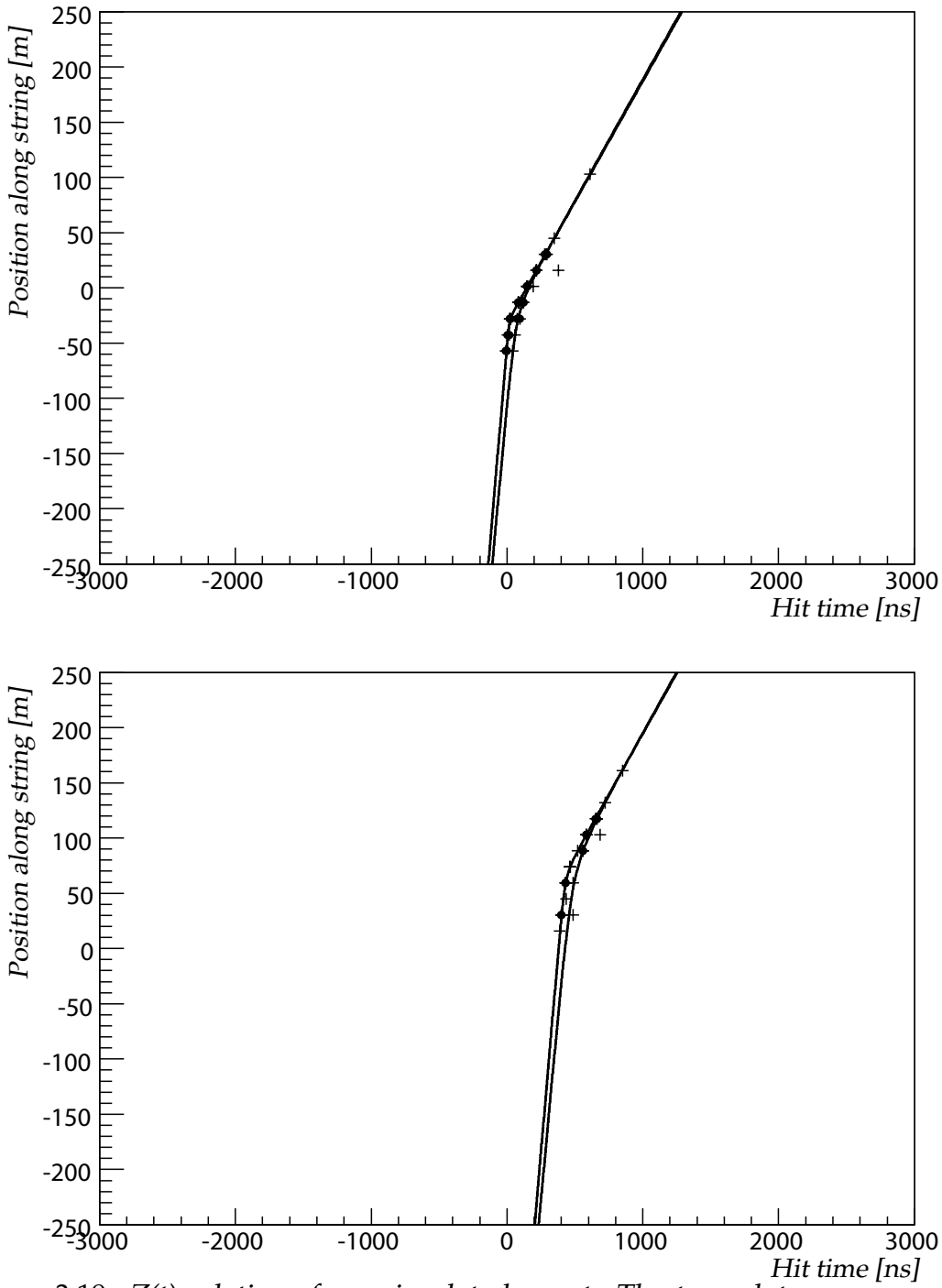

Figure 3.19: *Z(t) relations for a simulated event. The two plots correspond to different detector lines. The top plot corresponds to line 1 and the bottom to line 7 (see figure 2.8). The solid lines correspond to the expected arrival times of Cherenkov photons. In this event an additional muon originating from pion decay can be identified (the rightmost line). The black dots and crosses are hits caused by either line.*

range of muon energies.

A study of $\ln(L)/N_{dof}$ as a function of energy and background rate has been made. Figure 3.20 shows for three different background rates, the distribution of $\ln(L)/N_{dof}$ as a function the muon energy. The likelihood values are calculated with the fit starting at the true track coordinates. For all background rates a dependence on the energy can be seen. The original PDF shows a change of slope with increasing energy. This indicates a deviation from the expected trend that the likelihood increases with energy as the signal-to-noise of the hits increases. This is due to an increasing contribution of the second ARS hits. The modified PDF shows a more monotonous behavior. It can be concluded that the modification of the PDF and the associated hit selection lead to a better compatibility between the PDF and data.

Accuracy

The convergence of the full PDF fit is evaluated in the same way as the χ^2 fit in the previous section. Figure 3.21 summarizes the resolution after the fit as function of background rate and muon energy. It can be seen from figure 3.21 that the full PDF fit converges to smaller angular residuals than the χ^2 fit (compare figure 3.16). For small values of the angular offset, the value of the angular residual after the fit is consistently well below 1 degree and for higher energies well below 0.4 degrees.

3.6.5 Complete Algorithm

In this section the performance of the complete algorithm will be discussed. This is done by presenting the results after each stage of the fit. The results after the χ^2 stage will be presented first and then the results of the full PDF fit.

One feature of the algorithm was not taken into account so far when evaluating the different stages, especially the χ^2 and full PDF stage: the scanning of angular space not only maps out local minima, but can also provide different paths to a possibly broad (global) minimum. This can lead to multiple solutions which are (almost) identical. Solutions are considered identical when they differ less than 1 degree. When such a set of solutions is found, the different solutions are sorted according to the number of associated hits. The solution with the largest number of hits is taken as the best solution, and if there are different solutions with equal numbers of hits, the solution with the smallest χ^2 or the largest likelihood is selected.

χ^2 fit

As the algorithm, in general, produces several different solutions, various ways of selecting the 'best' solution are presented. The solutions are sorted based on

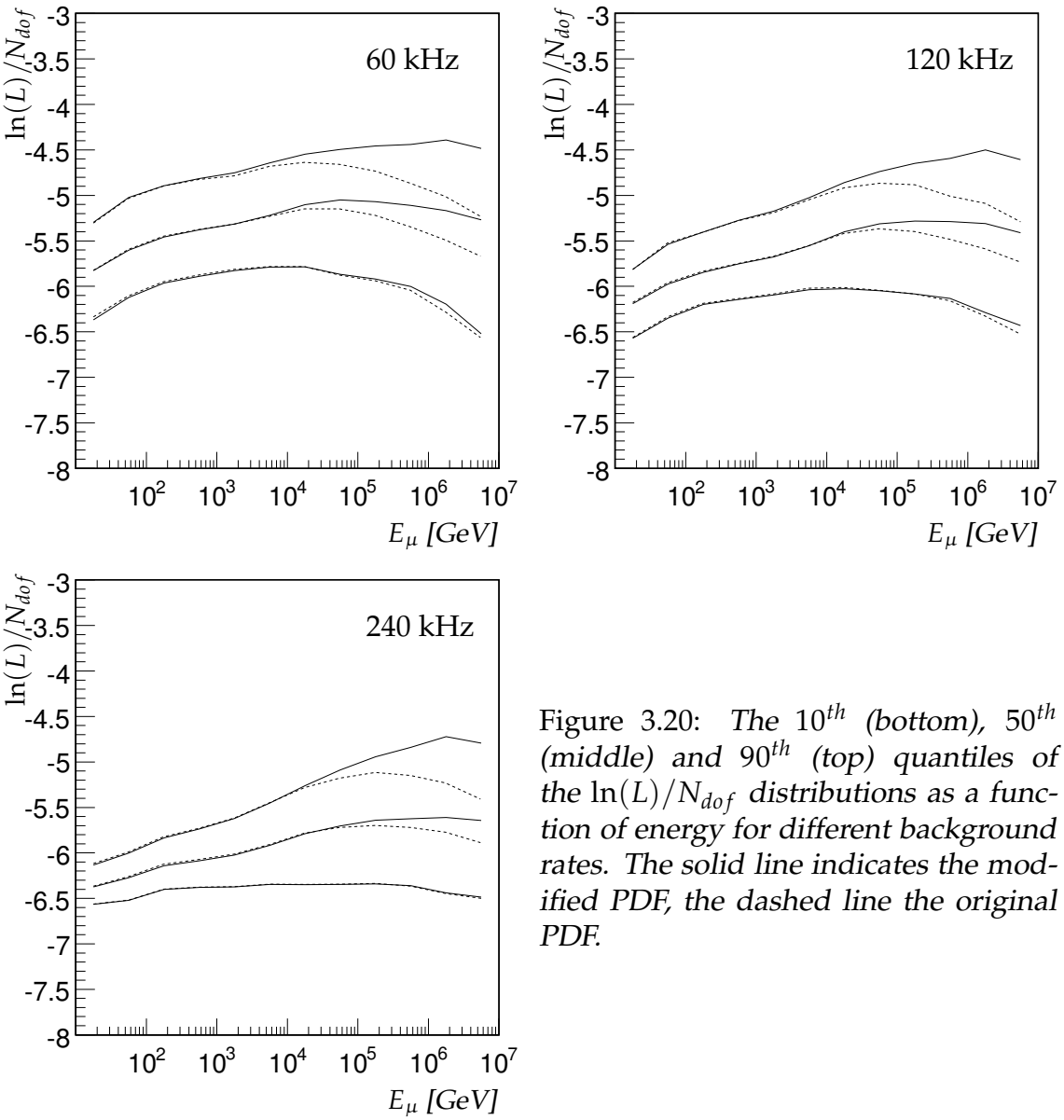

Figure 3.20: *The 10^{th} (bottom), 50^{th} (middle) and 90^{th} (top) quantiles of the $\ln(L)/N_{dof}$ distributions as a function of energy for different background rates. The solid line indicates the modified PDF, the dashed line the original PDF.*

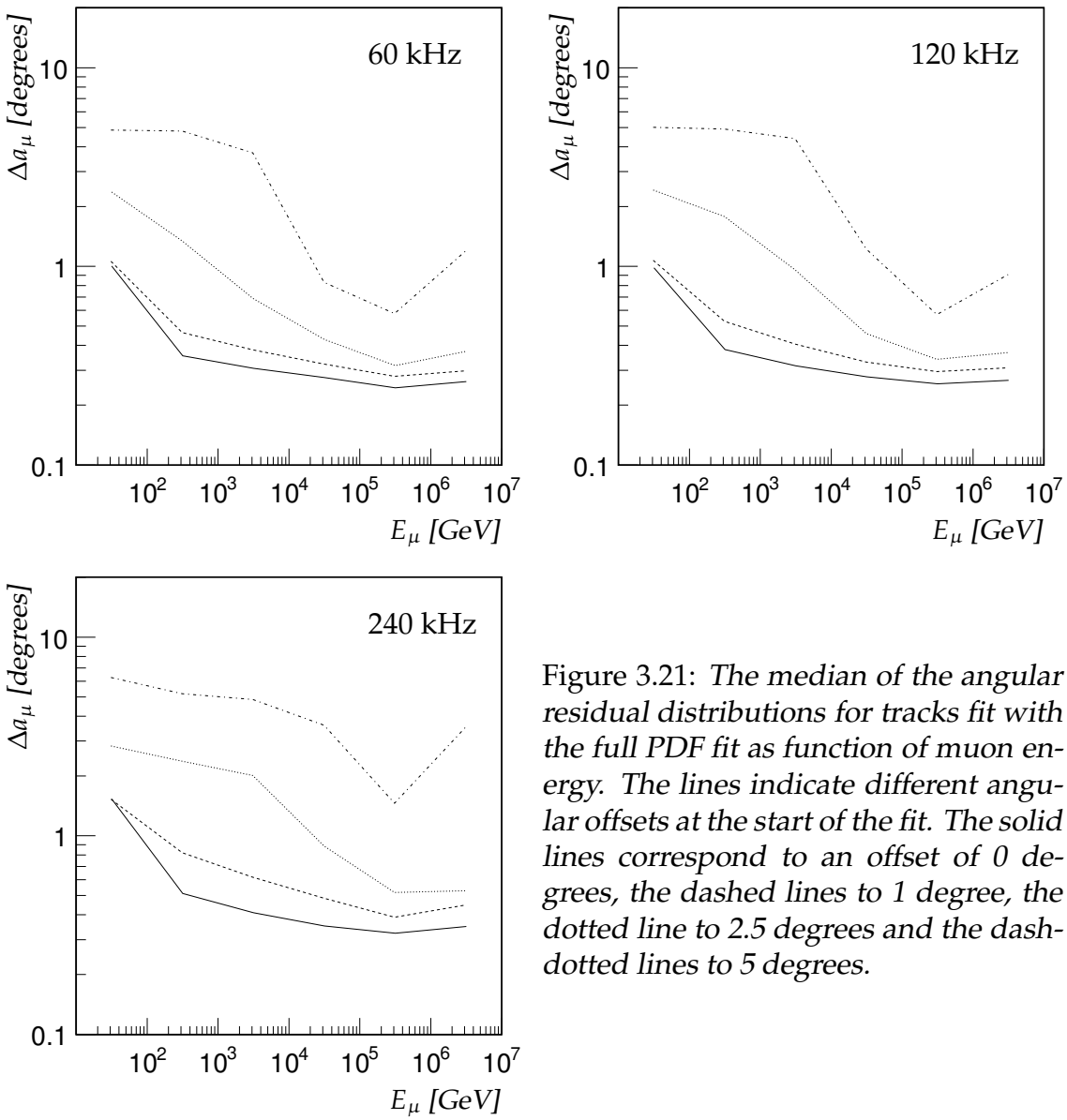

Figure 3.21: *The median of the angular residual distributions for tracks fit with the full PDF fit as function of muon energy. The lines indicate different angular offsets at the start of the fit. The solid lines correspond to an offset of 0 degrees, the dashed lines to 1 degree, the dotted line to 2.5 degrees and the dash-dotted lines to 5 degrees.*

the number of hits and on the χ^2 likelihood. The solution with the largest number of hits is taken as the best solution. If there are different solutions with the same number of hits, the solution with the smallest χ^2 is taken. Optionally, only solutions with a χ^2 probability of 1 % or larger are considered.

Figure 3.22 shows the χ^2 probability distribution after the fit. The value of the assumed time resolution is set to 1.75 ns for all hits. This is the same value used in the hit-removal. The distribution is reasonably flat indicating a good agreement between model and data. The rise towards higher values of $P(\chi^2)$ indicates a slight overestimate of the assumed time resolution. The peak at zero contains events with a large fraction of outlier hits. The resulting hit-time residual distribution is shown in figure 3.23, together with a fit of a Gaussian distribution. Only hits that are used for the reconstruction are included. The width of the fitted distribution is about 2 ns.

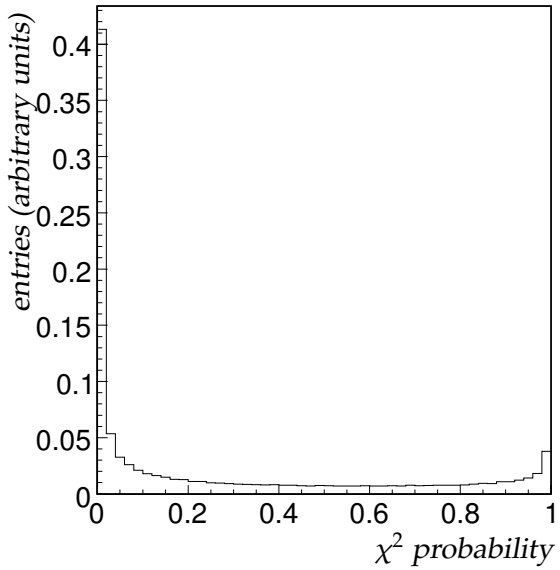

Figure 3.22: *Distribution of the χ^2 probability after the χ^2 fit. A grid size of 5 degrees is used and a background rate of 60 kHz has been assumed.*

The resolution of the χ^2 fit is summarized in figure 3.24 for an angular grid with a step size of 5 degrees. By comparing the lines corresponding to the median in figure 3.24 to those in figure 3.16, it can be seen that the angular residual has improved. For low rates the selection criterium is capable of selecting the solution closest to the true direction. The selection of fits based on χ^2 probability larger than 1 % is effective in decreasing the angular residual of the remaining events, especially at higher rates. The same sorting criterium is less effective for larger angular residuals. Although the angular resolution is the most important parameter for astrophysics, the error on the position of the muon has also been studied. In the context of the algorithm, a good estimate of the position helps in the next step of the fitting procedure. The next step is in this case the full PDF fit. The error on the position is measured by the distance of closest approach between the true muon track and the reconstructed track. As with the angular residuals this quantity is summarized as function of energy for the different background

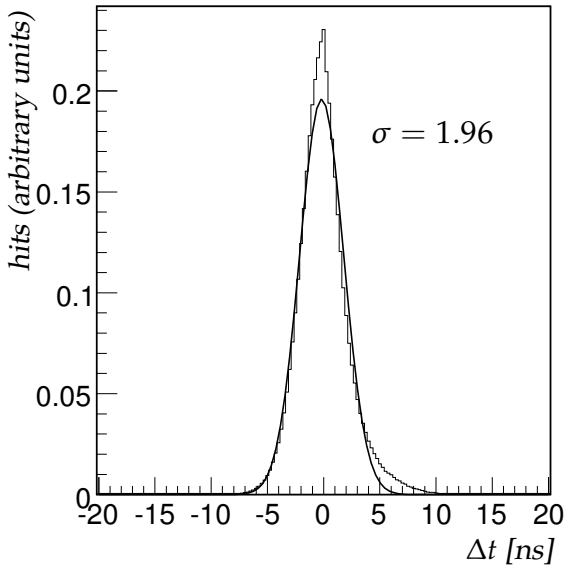

Figure 3.23: *Distribution of the hit time residuals after the χ^2 fit. A grid size of 5 degrees is used and a background rate of 60 kHz has been assumed. The smooth curve is a fit of a Gaussian distribution to the data (see text).*

rates. The result is shown in figure 3.25. As with the angular residual, the error on the position increases with the background rate, the median reaches 2 meters at high rates. There is a larger difference between the results using the best solution and the selected one. This is to be expected as the best solution is defined in terms of angular resolution, and the χ^2 probability cut selects on the overall quality.

Full PDF fit

The accuracy of the fit after the full PDF fit will now be presented. As after the χ^2 stage, there are in general multiple track candidates due to the angular scanning in the algorithm. In section 3.6.4 the likelihood per degree of freedom was introduced. This quantity is used to sort the different solutions for a given event. The solution with the largest likelihood per degree of freedom is taken as the preferred solution. In figure 3.26 the angular residuals are shown as a function of energy for different background rates. As can be seen from figure 3.26 the lines corresponding to the selected solution and the ideal case overlap for small angular residuals, except at the lowest energies. This validates the likelihood per degree of freedom as a sorting criterium. The angular residual (median) drops below 1 degree for about 100 GeV muons at 60 kHz, for 300 GeV muons at 120 kHz and 240 kHz. The angular residual (median) reaches 0.3 degrees for about 30 TeV muons at 60 kHz. At 120 and 240 kHz this angular resolution is reached at about 200 TeV.

The likelihood per degree of freedom is used to select the preferred solution. It is also a measure of fit quality. This was shown for instance in reference [74]. There, a cut on the likelihood per degree of freedom was used to separate well reconstructed tracks from poorly reconstructed tracks. The two most important

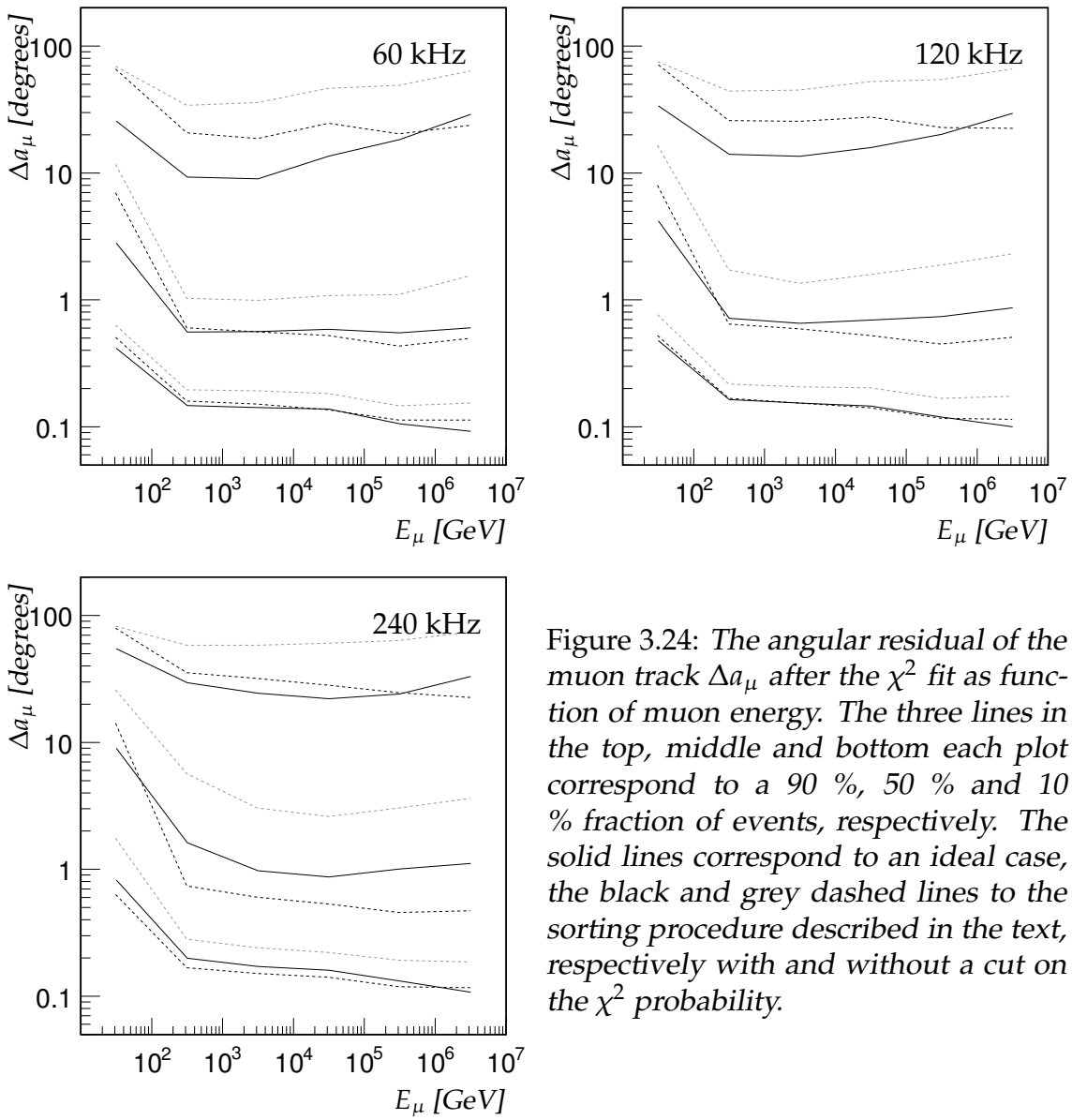

Figure 3.24: *The angular residual of the muon track Δa_μ after the χ^2 fit as function of muon energy. The three lines in the top, middle and bottom each plot correspond to a 90 %, 50 % and 10 % fraction of events, respectively. The solid lines correspond to an ideal case, the black and grey dashed lines to the sorting procedure described in the text, respectively with and without a cut on the χ^2 probability.*

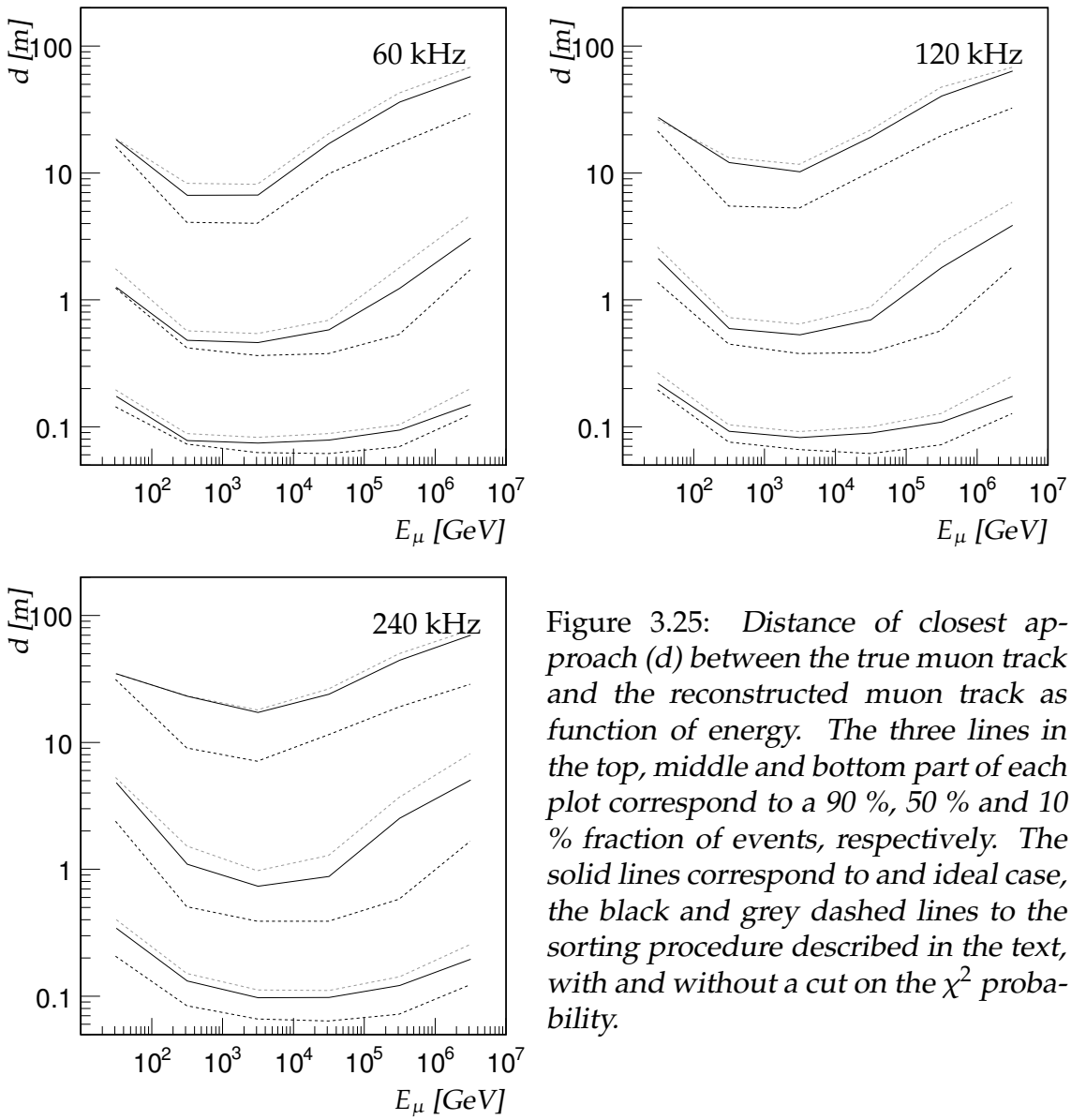

Figure 3.25: *Distance of closest approach (d) between the true muon track and the reconstructed muon track as function of energy. The three lines in the top, middle and bottom part of each plot correspond to a 90 %, 50 % and 10 % fraction of events, respectively. The solid lines correspond to and ideal case, the black and grey dashed lines to the sorting procedure described in the text, with and without a cut on the χ^2 probability.*

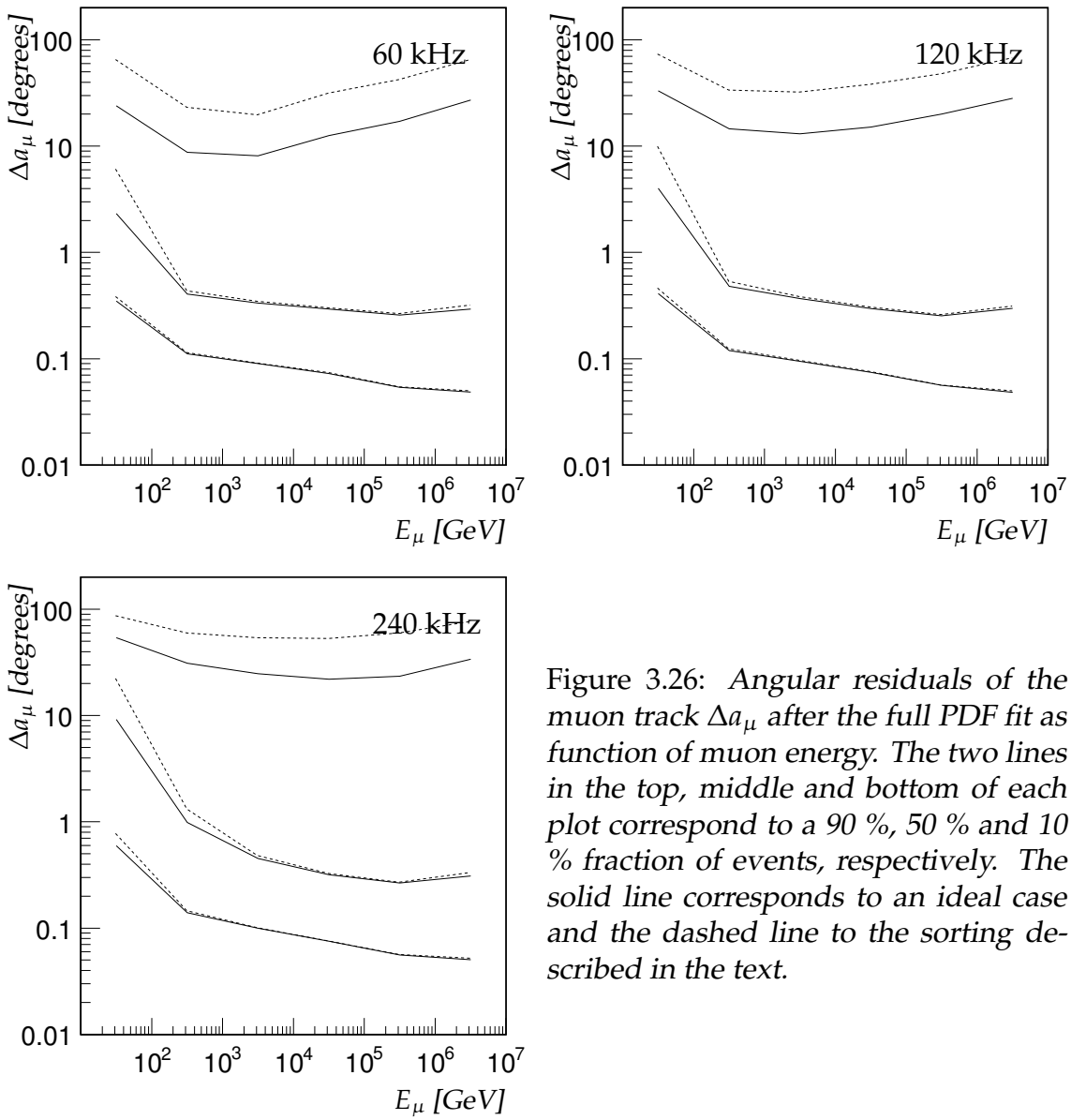

Figure 3.26: *Angular residuals of the muon track Δa_μ after the full PDF fit as function of muon energy. The two lines in the top, middle and bottom of each plot correspond to a 90 %, 50 % and 10 % fraction of events, respectively. The solid line corresponds to an ideal case and the dashed line to the sorting described in the text.*

features related to a cut on the likelihood per degree of freedom will be discussed. First, as shown in section 3.6.4, the behavior of the likelihood per degree of freedom depends on the background rate. Thus a cut on this quantity behaves differently for different background rates. The optimum value will be different for different background conditions. Which brings us to the second point. In general, a cut to improve quality has negative consequences for the efficiency. The fit quality, or accuracy, and efficiency are two related quantities. The relation between these two quantities has been studied in more detail. The event samples for the different background rates were divided in three energy bins. The first with 1 GeV $< E_\mu \leq$ 1 TeV, the second with 1 TeV $\leq E_\mu <$ 100 TeV and the third with 100 TeV$\leq E_\mu <$ 10 PeV, referred to as low, medium or high energies, respectively. To each of these samples, different cuts on the likelihood per degree of freedom were applied. For each of these cut values, the median of the angular residual distribution was calculated, together with the efficiency. The efficiency is defined as the remaining fraction of events with respect to all reconstructed events. The results are shown in figure 3.27. As can be seen from figure 3.27 the efficiency decreases with increasing cut values, while the accuracy increases. As seen before, the accuracy of the fit increases with energy. It can also be seen that, with increasing background rates, the cut levels for a given efficiency and accuracy increase. This reflects the overall shift of the likelihood per degree of freedom distribution as shown in section 3.6.4. Another observation is that for different background levels, the accuracies for a given efficiency differ by a small amount, typically less than 15 %.

3.6.6 Error estimates

The pull of a fitted quantity is defined as the difference between the fitted quantity and the true quantity (the residual) divided by the estimated uncertainty (one sigma error). Thus for the zenith angle θ the pull is $\left(\hat{\theta} - \theta\right) / \sigma_{\hat{\theta}}$. Ideally, the distribution of the pull should be a Gaussian distribution with mean 0 and width 1. For a maximum likelihood fit, generally, the 1σ limit is given by the parameter values for which $\ln(L_{max}) - \ln(L) = 0.5$ with L_{max} the maximum likelihood value resulting from the fit. In the limit of infinite data, the distributions can be described by a Gaussian function. In this case, the error matrix $\mathbf{V}$ is given by the inverse of the second derivative, or Hesse, matrix $\mathbf{H}$:

$$\mathbf{V} = \mathbf{H}^{-1} \tag{3.23}$$

$$\mathbf{H}_{ij} = \frac{-\partial^2 \ln L}{\partial x_i \partial x_j}\Big|_{L=L_{max}} \tag{3.24}$$

where $\vec{x} = (\theta, \phi, a, b, t_0)$ is the vector of track parameters. The Hesse matrix is calculated during the fit procedure and is determined together with the estimated

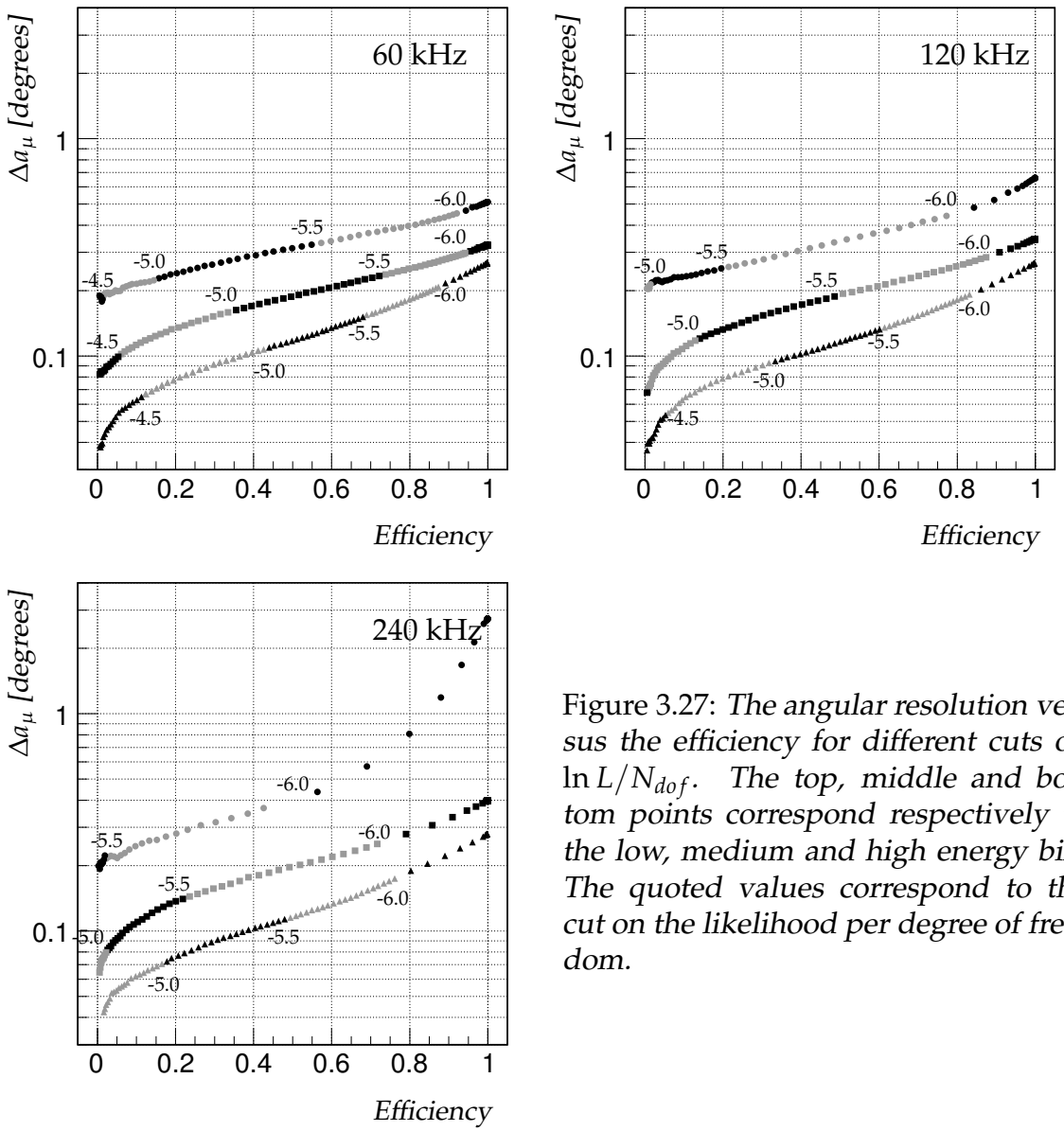

Figure 3.27: *The angular resolution versus the efficiency for different cuts on* $\ln L/N_{dof}$. *The top, middle and bottom points correspond respectively to the low, medium and high energy bin. The quoted values correspond to the cut on the likelihood per degree of freedom.*

track parameters. The diagonal elements of $\mathbf{V}$ are the variances of the track parameters, $(\sigma^2_{\hat{\theta}}, \sigma^2_{\hat{\phi}}, \sigma^2_{\hat{a}}, \sigma^2_{\hat{b}}, \sigma^2_{\hat{t}_0})$ and are used to calculate the pull values. The distributions are shown in figure 3.28 for the zenith angle and the azimuthal angle. The pull distributions in figure 3.28 have a similar shape. As expected, they peak at zero. The distributions are not fully Gaussian as they have longer tails towards negative and positive values. These tails are due to events in which either a local minimum of the likelihood was found or the global minimum did not correspond to the true muon direction. This leads to an underestimation of the error. A Gaussian function has been fitted to the data in the interval $-3 \leq \text{pull} \leq 3$. This includes more than 75 percent of the data. The widths of the fitted functions are indicated in figure 3.28. The fitted widths are typically 1.2. This indicates a consistent description of the PDF. The fitted widths are in reasonable agreement with the expected value of 1, but the errors are slightly (20%) underestimated.

3.6.7 Track length

A muon track is measured across a certain longitudinal distance. When the muon energy exceeds 100 GeV, it can traverse the complete detector. One expects that the accuracy with which the track parameters can be determined, depends to certain extent on the length of the track that is sampled. In order to estimate this effect, the quantity $\Delta z^{'}$ is used. This quantity is equal to the largest distance between two hits, measured along the track. So, in the reference frame defined by the track direction (see section 3.2) $\Delta z^{'}$ equals the difference between the hits with the largest and smallest z coordinate :

$$\Delta z^{'} = z^{'}_{max} - z^{'}_{min} \tag{3.25}$$

The collection of hits used by the full PDF fit includes hits caused by the random background. When calculating $\Delta z^{'}$ these background hits should be avoided. For this reason, only the hits selected by the 1D clustering algorithm (see section 3.3.1) are considered when calculating $\Delta z^{'}$. The relation between the median of the angular residual of the muon Δa_μ and $\Delta z^{'}$ is shown in figure 3.29 for different background rates. The assumed neutrino energy spectrum is proportional to E^{-2}. Figure 3.29 shows a strong dependence of the muon angular residual on the sampled track length. With a sampled track length of about 150 meters and more, the angular residual drops below 1 degree. For a background rate of 240 kHz this happens at 180 meters. At 380 meter track length, the median angular residual reaches 0.1 degree for a random background rate of 60 kHz. The slope of the curve at the end of the plot, which is limited by the detector geometry is still negative, indicating that a larger detector would improve the angular residual even more. The right plot of figure 3.29 shows a box plot of the angular residual versus the sampled length. The size of the boxes indicates the relative occurrence of a certain track length and angular residual. It can be seen that most of the tracks

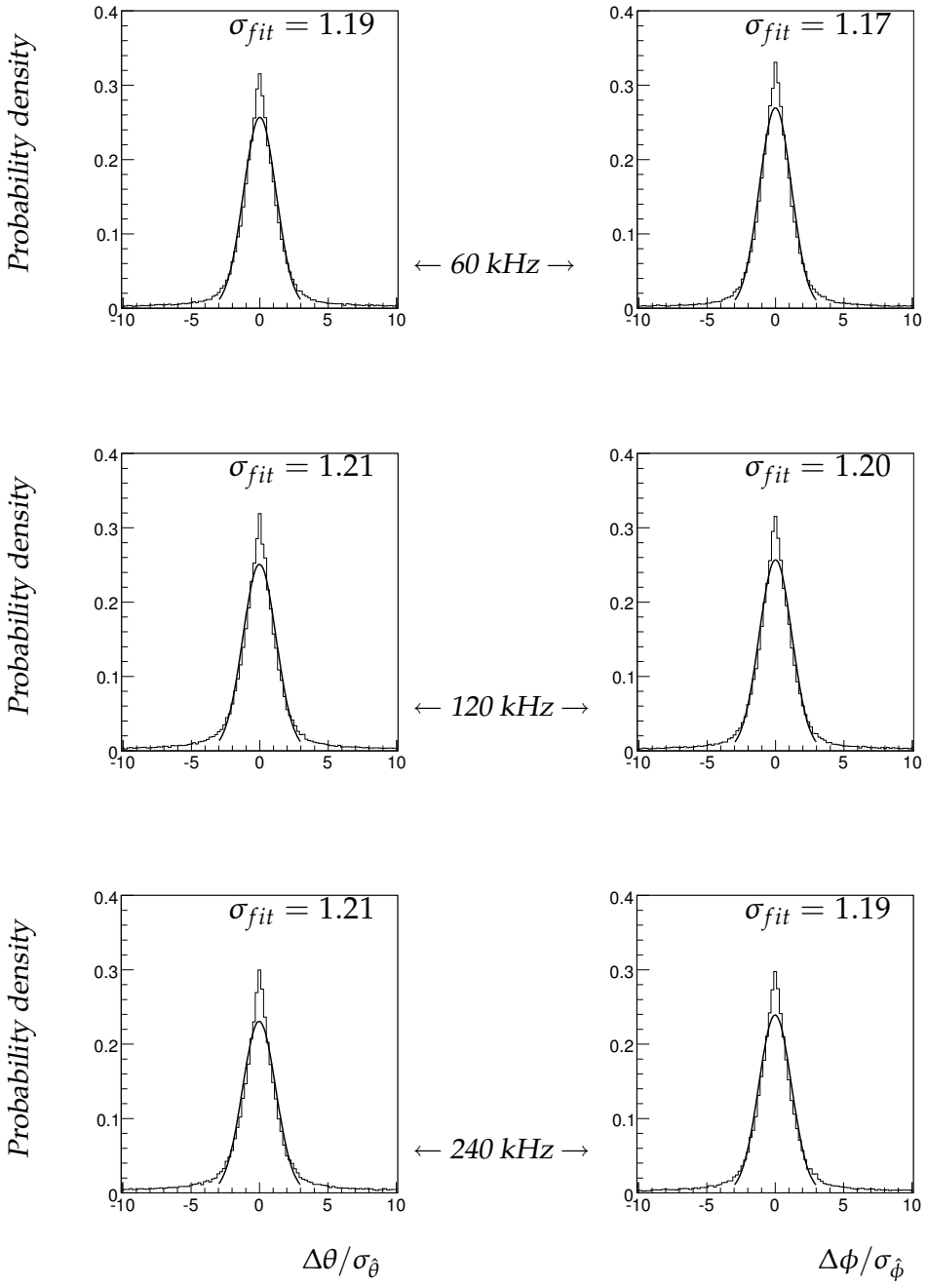

Figure 3.28: *Pull distributions for the zenith (left) and azimuth (right) angles. The distributions are shown for different random background rates.*

have a sampled length around 200 meters, which is characteristic for the Antares neutrino telescope.

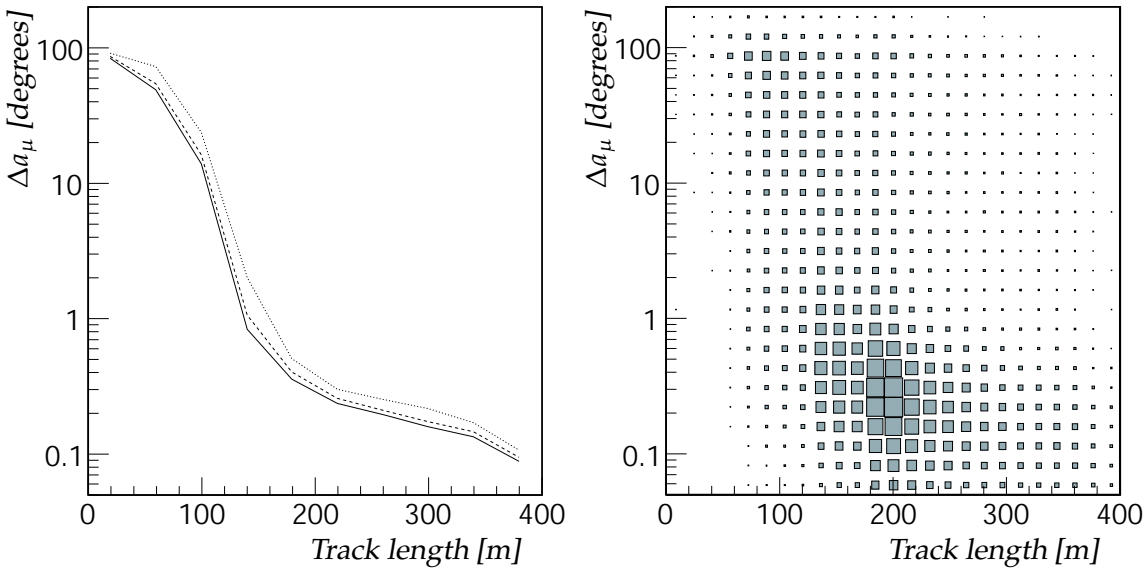

Figure 3.29: *Left : The median angular residual after the full PDF fit as function of estimated track length in the detector. The line types indicate different background rates. The solid line corresponds to 60 kHz, the dashed line to 120 kHz and the dotted line to 240 kHz. Right : Scatter plot of angular residual versus the estimated track length in the detector.*

3.6.8 Compatible solutions

The muon track reconstruction procedure starts out with a scan of the angular space to map out all solutions. In the consecutive fitting steps, the angles are free parameters. If a track is not rejected on basis of the number of selected hits, it can converge to a local optimum. Track candidates with different starting angles can converge to the same local or global minimum of the χ^2 or likelihood. When the global minimum is well defined it is more likely that several track candidates will converge to this same minimum. So, the number of track candidates that converge to the same solution can be considered as a measure for the overall quality. As explained before, tracks that converge to within 1 degree are collected and the one with the largest number of associated hits is taken. This is done for the χ^2 fitting step and for the full PDF fitting step. The number of converged tracks for a given solution are propagated from the χ^2 step on to the full PDF fit, and are taken into account when calculating the final number of track candidates that converged to a certain solution. This number is referred to as N_{comp}. This quan-

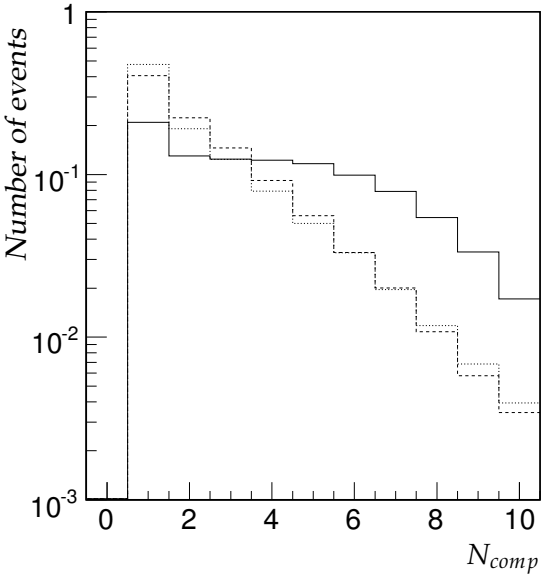

Figure 3.30: *Distribution of the number of compatible solutions N_{comp} after the full PDF fit. The solid line indicates a random background of 60 kHz, the dashed 120 kHz and the dotted 240 kHz.*

tity is already to some extent present in the fitting procedure developed in [74]. Now it is defined in a more rigorous way. Figure 3.30 shows the distribution of N_{comp} for the solution with the largest likelihood per degree of freedom after the full PDF fit for different rates. It can be seen from figure 3.30 that all distributions are peaked at one. A tail containing events in which multiple track candidates converged to the same solution is present. The size of this tail decreases with increasing random background rate. This can be expected as the minimum of the negative likelihood becomes less pronounced. The muon angular residual as function of N_{comp} is shown in figure 3.31. It can be seen from figure 3.31 that the events reconstructed with an angular residual smaller than 1 degree are dominated by events with $N_{comp} > 1$. It can also be seen that with increasing random background rates, the solutions with $N_{comp} > 1$ migrate to lower values of N_{comp} and to larger angular residuals. To conclude, the value of N_{comp} can be used as an indicator of track quality.

3.7 Summary

The muon track reconstruction algorithm presented in this chapter consists of several elements. It includes a partial scan over the phase space to map out local solutions. This scan is combined with a hit selection procedure which aims to maximize the purity of the hits with respect to the assumed muon. Candidate tracks from the scanning phase are used to start a final fit χ^2 based fit using the selected hits. This method aims at maximizing the performance without relying on detailed knowledge of the environmental properties. This robustness makes it particular useful at the beginning of detector operation. The performance of the reconstruction was evaluated and shown to able to achieve a resolution of

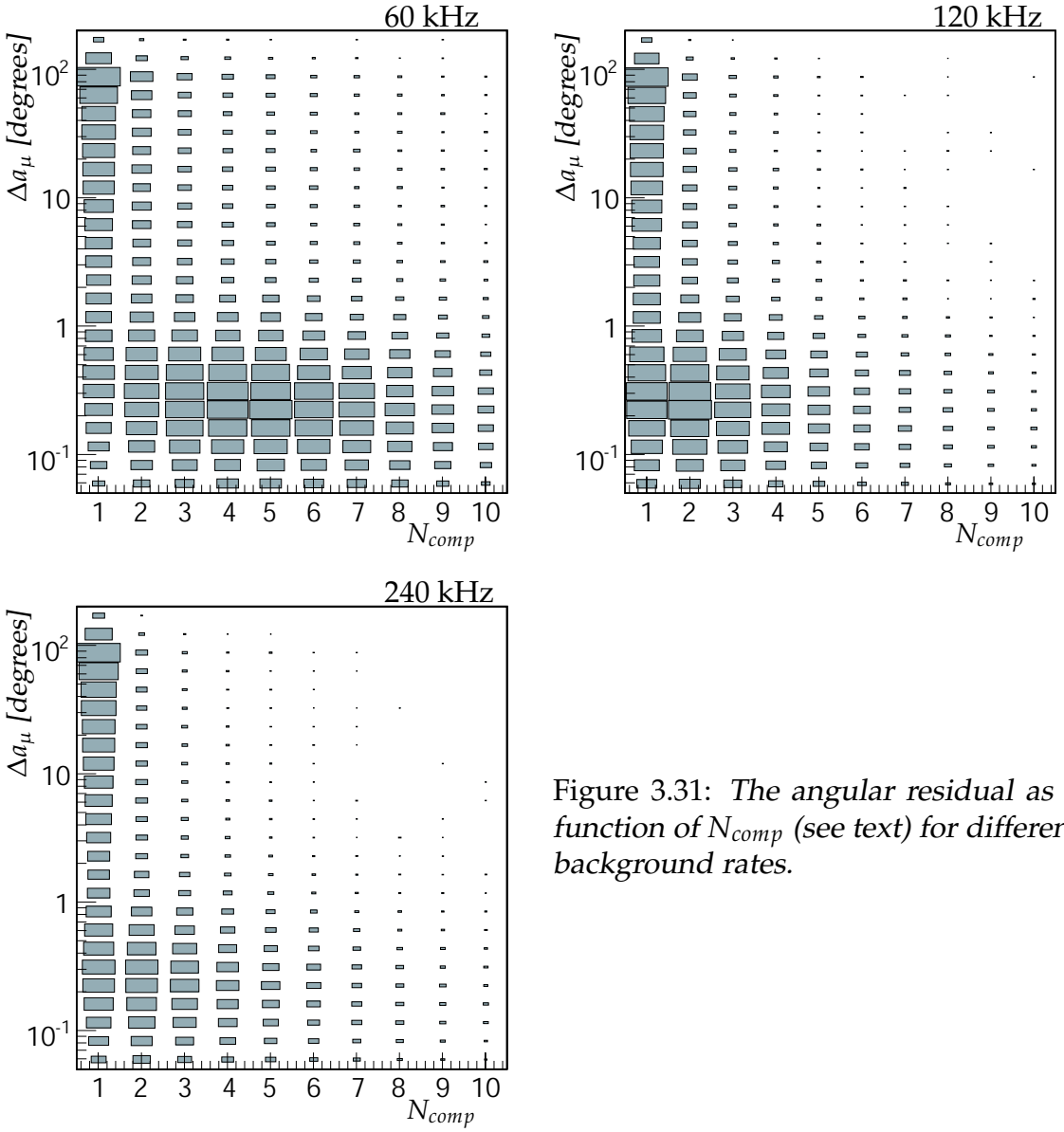

Figure 3.31: *The angular residual as a function of N_{comp} (see text) for different background rates.*

0.5 degrees for neutrinos at 60 kHz background rate and 1 degree at 240 kHz. However, in order to achieve better performance in terms of angular resolution, a more detailed modeling of the processes leading to the photon signal is needed. This was done by including a maximum likelihood fit using a detailed PDF for the hits. The PDF describing the hits was modified together with a the selection of hits in order to reduce the effect of correlations between hits. The maximum likelihood fit improves the angular resolution. It was found that the occurrence of correlated hits due to electro-magnetic showers affects the ability of the algorithm to estimate the track parameters. Several quantities were identified which can be used as indicators of track quality. The hit selection procedure based on the directional causality relation offers a way to calculate a track length. The angular resolution scales with this track length and is limited by the finite size of the Antares detector. The value of the log-likelihood per degree of freedom can be used to select a track from the track candidates. It is also a good measure of track quality. Also the number of tracks converging to the same solution is a measure of track quality. Studies of the performance of the track reconstruction were done for several background rates covering those encountered during data taking. The angular resolution is most affected at low energies. At 100 GeV muon energy doubling the background rates from 60 to 120 kHz or from 120 to 240 kHz results in a maximum deterioration of the angular resolution by a factor 2. However, at higher energies (10^6 GeV muon energy) the difference is negligible.

Chapter 4

Analysis of Line 1 Data

Line 1, the first full detector line of the Antares detector, was deployed on February 14 2006 and connected 16 days later on March 2. Using the algorithm described in chapter 3, the first muon tracks were reconstructed shortly after. This chapter will describe a more detailed analysis of the data that were taken until September 21. On that day the second line was connected, and the analysis of single line data was abandoned in favor of two line data.
In the analysis presented in this chapter, the muon track reconstruction algorithm presented in chapter 3 was used, excluding the full PDF fit.

4.1 Introduction

Line 1 represents a special case for the muon reconstruction. All optical modules are arranged along a single string which can be approximated by a straight line. With this assumption the optical modules are placed at $x = 0, y = 0$. The position is then only defined by z, the position along the line. This introduces a rotational symmetry around the z-axis. The arrival times of Cherenkov photons is no longer dependent on ϕ, and formula 2.5 reduces to a 4-parameter formula [78]. This relation can be derived as follows. A muon traveling with the speed of light emits a Cherenkov photon at position $\vec{e}$, as illustrated in figure 4.1. Position $\vec{o}'$ corresponds to the point where the muon passes the line at the closest distance. The corresponding position on the line is $\vec{o} = (0, 0, z_0)$. The time at which the muon passes point $\vec{o}'$ is defined as t_0. Using the relation $\cos(\theta_c) \times |\vec{a} - \vec{e}| = |\vec{p} - \vec{e}|$, the muon passes position $\vec{a}$ when the photon reaches position $\vec{p} = (0, 0, z)$ where

it is detected at time t. With this it follows :

$$\begin{aligned} c \times (t - t_0) &= |\vec{a} - \vec{o'}| \\ &= -|\vec{o'} - \vec{r}| + |\vec{a} - \vec{r}| \\ &= \cos(\theta) \times (z - z_0) + \frac{|\vec{p} - \vec{r}|}{\tan(\frac{\pi}{2} - \theta_c)} \\ &= \cos(\theta) \times (z - z_0) + \tan(\theta_c)\sqrt{|\vec{r} - \vec{q}|^2 + \vec{p} - \vec{r}|^2} \\ &= \cos(\theta) \times (z - z_0) + \sqrt{n^2 - 1}\sqrt{d^2 + (z - z_0)^2 \sin^2(\theta)} \end{aligned} \tag{4.1}$$

As can be seen in the final expression, the arrival time of the photon is described by a hyperbolic function and is independent of the azimuthal angle ϕ. The asymptotes of the function can be found in the case

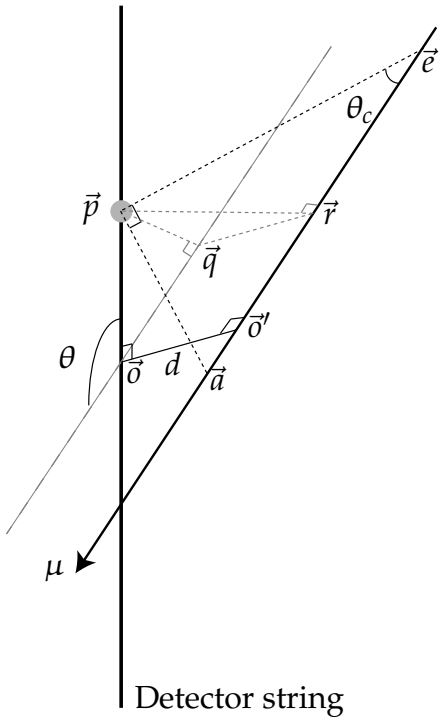

Figure 4.1: *Schematic view of a muon passing a detector line.*

$$|(z - z_0)| \gg \frac{d}{\sin(\theta)} \tag{4.2}$$

By using this assumption

$$c \times (t - t_0) = (z - z_0) \times (\cos(\theta) \pm \sqrt{n^2 - 1}\sin(\theta)) \tag{4.3}$$

and the distance d drops out. So, in this case, the distance d of the muon to the line cannot be determined. Furthermore, equation 4.3 can be simplified to

$$c \times (t - t_0) = (z - z_0) \times n \times \cos(\theta \pm \theta_c) \tag{4.4}$$

From this it can be seen that the two asymptotic solutions differ by $2\theta_c$. Requirement 4.2 can be met when a muon passes above or below the optical modules that record a hit, so that only one side of the Cherenkov cone is seen. In this case it is not possible to distinguish between the two asymptotic solutions and possibly the zenith angle of the muon is reconstructed with an offset of $2\theta_c$. This is illustrated in figure 4.1. These solutions are usually referred to as *ghost* solutions. In this analysis, the general formalism introduced in chapter 3 is used. The rotational symmetry is taken into account by fixing the ϕ parameter. As a result, the number of free parameters in the fit is reduced to 4.

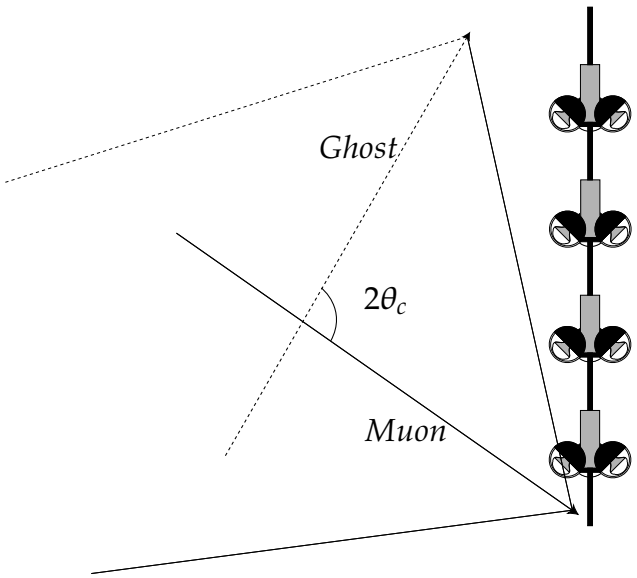

Figure 4.2: *When only one side of the Cherenkov cone of a muon is seen with a single line, an additional* ghost *solution exists. The solid lines indicate the true muon. The dashed lines indicate the* ghost *solution with its inferred missing part of the Cherenkov cone.*

4.2 Data sample

For this analysis, runs are selected from the period when Line 1 was operated stand-alone. The selected runs are flagged as 'golden' in the Antares run-selection.

A run obtains the qualification 'golden' if it meets the following requirements :

- Time lost at run start and stop is less than 100 seconds
- Total run time is more than 4000 seconds
- Trigger rate between 0.01 Hz and 10 Hz
- The baseline rate averaged over all active components should be below 120 kHz
- The burstfraction must be below 15 %

Figure 4.3 summarizes the baseline rate and burstfraction for the whole period. Each point represents the average baseline rate (figure 4.3 top) or the burstfraction (figure 4.3 bottom) for a period of 15 minutes. The black dots in the middle of figure 4.3 indicate the runs selected for this analysis. The number of runs that were selected is 63. For all selected runs, the high-amplitude threshold for L1-hits was equal to 10 photo-electrons, the standard 3D trigger was used with a minimum cluster size of 5 and event merging was on. Although the integrated running time for the selected runs is 1612764 seconds, the effective measuring time is a factor two smaller, namely 806382 seconds or about 9.3 days. This is due to the sampling factor (see section 2.6.3) which was 2 for all the selected runs. The number of triggered events written to disk during the golden runs is 75621. This corresponds to an average trigger rate of 0.094 Hz.

4.3 Monte Carlo simulation

For this analysis, a full simulation of the detector response to atmospheric muons and atmospheric neutrinos has been made. In the following a short description of the optical background, the acceptance of the optical modules and the detector geometry is given.

4.3.1 Optical background

The uncorrelated random background is simulated using the procedure explained in section 2.10. The goal is to simulate the environmental conditions, and their effects on data taking, that were present during the runs selected for this analysis. A selection is made, representing the statistical properties of the whole sample. In total 53.4 hours of data, spread over 13 runs are used. Figure 4.4 shows the distribution of rates that is used in the simulation (solid line) together with the actual measured distribution for the whole set (dashed line). By applying the trigger algorithm to data generated using this sample, the trigger rate due to uncorrelated background has been estimated. The trigger rate due to accidental coincidences was found to be less than 0.01 Hz.

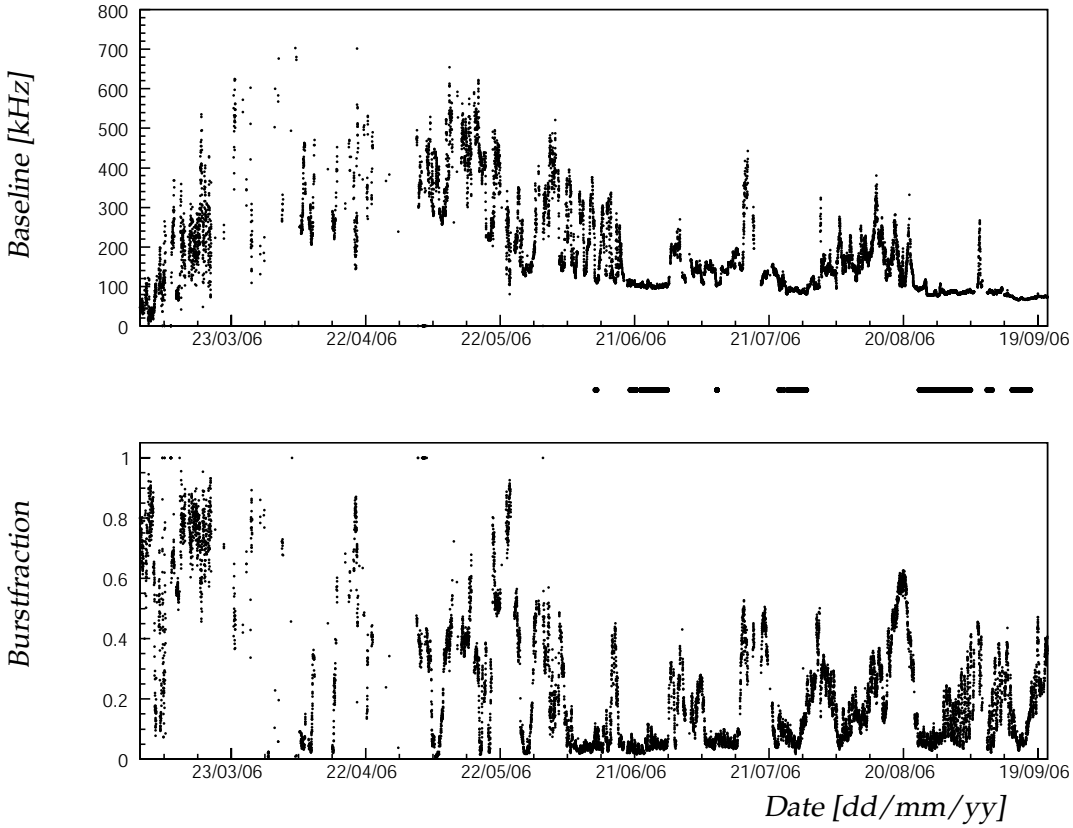

Figure 4.3: *Baseline rate (top) and burstfraction (bottom) versus time for Line 1. The black points between the plots indicate the periods selected for the analysis.*

4.3.2 Angular acceptance of the optical modules

The acceptance of the optical module depends on the angle of incidence of the photon. The optical modules are oriented downwards at and angle of 45 degrees from vertical. This maximizes the acceptance for light from upward going muons. As a consequence the photons from downward going muons hit the optical module at the edge of its acceptance, as can be seen in figure 2.5. As a consequence, a small error in the assumed acceptance translates directly to a large error in the event rate. This is taken into account as a systematic error. In order to quantify the systematic error due to the angular acceptance, an alternative parameterisation of the angular acceptance is used besides the one obtained from a measurement of the acceptance [40]. This alternative parameterisation is obtained through a ray tracing simulation of the optical module [42].

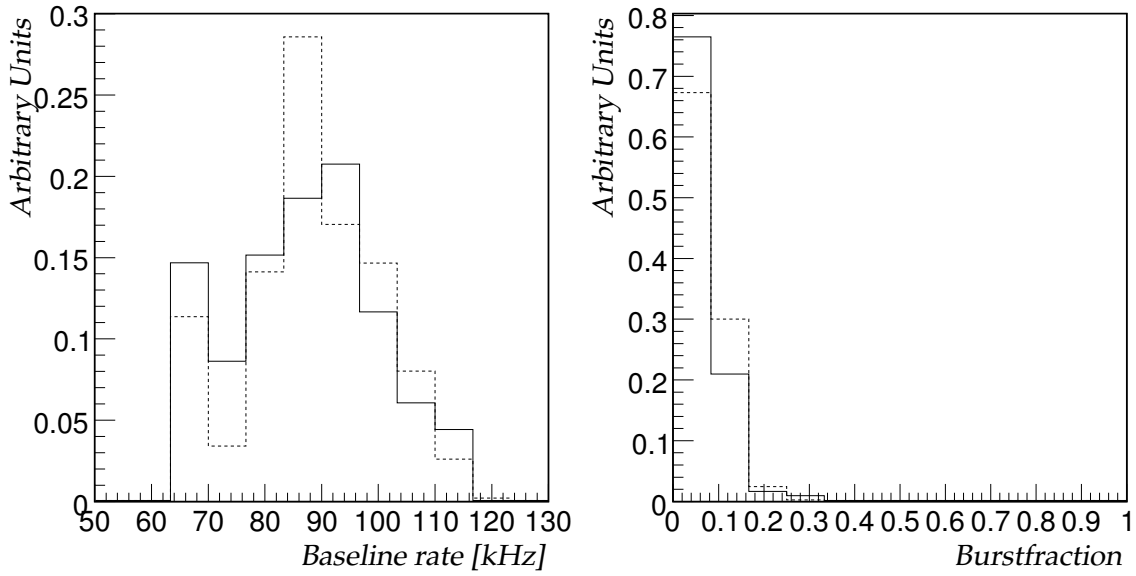

Figure 4.4: *Distribution of baseline rate (left) and burstfraction (right) for simulation (solid lines) and data (dashed lines).*

4.3.3 Line geometry

In this analysis of the data from Line 1, the detector line is assumed to be perfectly straight. Of course, in reality the line is subject to forces due to the undersea environment. Hence, the line will be bent. Two factors contribute to the uncertainty on the optical module positions. First there is the rotation of a storey around the axis. The distance from the photo-cathode of the PMT to the axis is about 56.4 cm. Ignoring the rotation of a storey introduces an error of $\sqrt{1/6} \times 56.4 \approx 23$ cm on both the x and y coordinate. The total uncertainty due to the rotation is thus about 32.5 cm. The error on the position can be transformed into an uncertainty on the timing considering the speed of light in water. The error on the timing due to the rotation is then about 1.5 ns. Second, the underwater currents can make the line sway. This makes for two effects to be considered. The current introduces relative offsets in the x-y plane between storeys. As a result, an error in the relative positioning of the storeys and thus optical modules is introduced. Figure 4.5 shows the distribution of the water-current speeds as measured with the ADCP on the MILOM for the periods of the run selection. These currents correspond to the line deviating 1 meter or less from a vertical position for 94 % of the selected data taking period. A deviation of 1 meter corresponds to an error of about 4.5 ns. The second effect of the swaying affects the absolute orientation of the line. When the detector line is tilted, while assuming a vertical orientation,

the true zenith is displaced with respect to the assumed zenith. A displacement of the top of the line of 1 meter, corresponds to a shift of the zenith of far less than 1 degree. This displacement is smaller than the expected resolution. In summary, a static alignment has been assumed in this analysis.

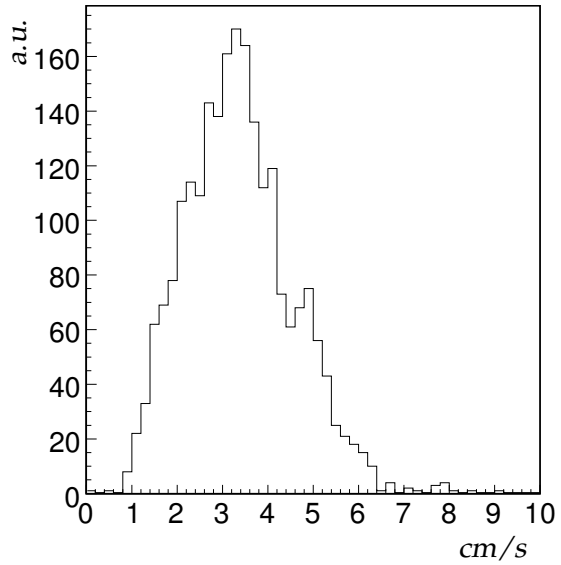

Figure 4.5: *Distribution of the water current speed as measured with the MILOM during the data taking period used in this analysis.*

4.3.4 Atmospheric muons

For this study, the atmospheric muons are generated with the fast simulation program MUPAGE, as described in section 2.10.2. For efficiency reasons, the sample was divided in two samples of different muon multiplicity (N_μ) ranges. The ranges were $1 \leq N_\mu < 30$ and $31 \leq N_\mu < 1000$. Each of the ranges represents its own equivalent livetime. In table 4.1 the atmospheric muon samples used for this study are summarized. In the table, the different (sub)samples are organised in columns. The row 'OM Angular acceptance' indicates the angular acceptance used for the samples. The row 'Multiplicity' indicates the muon multiplicity range. The row 'Generated' corresponds to the number of atmospheric muon events generated on the so-called can. The row '$N_{photons} \geq 10$' corresponds to the number of events with at least 10 detected photons. The rows 'Triggered' and 'Reconstructed' correspond to the number of triggered and reconstructed events, respectively. The row 'Livetime' corresponds to the total livetime of the sample. From this livetime, together with the number of triggered events, the trigger rate can be calculated. The trigger rate is indicated by the row 'Trigger rate'.

OM Angular acceptance	From [40]		From [42]	
Multiplicity	1-30	31-1000	1-30	31-1000
Generated	$880 \cdot 10^6$	$8 \cdot 10^6$	$440 \cdot 10^6$	$3.6 \cdot 10^6$
$N_{photons} \geq 10$	3538930	73381	2133348	35034
Triggered	70930	17184	55211	9075
Reconstructed	66925	16114	52689	8545
Livetime [day]	11.7	32.4	5.6	14.6
Trigger rate [Hz]	0.066	0.006	0.11	0.007

Table 4.1: *Sample of simulated atmospheric muons used in this study.*

4.3.5 Neutrinos

The neutrino sample consists of a mixture of muon neutrinos and anti-neutrinos. The energy ranges between 10 GeV and 10 PeV generated randomly according a $E^{-1.4}$ spectrum. Only upward going (anti-) neutrinos ($\cos(\theta) > 0$) were generated. The generation was done with the GENHEN package that is described in section 2.10.3. Table 4.2 summarizes the sample used. The sample is sub-divided in neutrinos and anti-neutrinos. The row 'Generated' corresponds to the number of neutrino interactions generated inside the so-called extended can. The other rows have the same definition as in the previous section.

Neutrino type	ν_μ	$\bar{\nu}_\mu$
Generated	$91 \cdot 10^{10}$	$110 \cdot 10^{10}$
$N_{photons} \geq 10$	330865	414859
Triggered	107279	136914
Reconstructed	106432	131256

Table 4.2: *Sample of simulated neutrino events used in this study.*

4.4 Event display

For the Line 1, the position of a hit is described by a single coordinate, namely the height z. This means that the two most important quantities for reconstruction, the position and time of the hits, can be plotted in a 2-dimensional display. Such a display is referred to as a z(t) plot. Two displays of real events are shown in figures 4.6 and 4.7. The y-axis indicates the position of the hit along the line, where $z = 0$ corresponds to the middle of the line. The x-axis gives the time at which the hit was measured, where $t = 0$ corresponds to the time of the first triggered hit. The crosses are the hits from the so-called snapshot (see section 2.8) and the black dots are hits that caused the event to be triggered. Information

about the result of the reconstruction is also shown. A square box around a hit means that this particular hit was used in the reconstruction of the event. Using the estimated track coordinates a prediction is made for the arrival time of direct Cherenkov light at a given position. This prediction is shown as the solid curve. Figure 4.6 shows an event that has hits on all the 25 floors of the line. Hits from all these floors are used to reconstruct the event. The reconstructed zenith angle of this event is about 180 degrees ; a vertically down going event. Figure 4.7 shows an event in which 8 floors are used in the reconstruction, of which 5 caused the trigger. The zenith angle of this event is about 142 degrees. In figure 4.7, the intersection of the Cherenkov cone with the detector can be recognised as the curved solid line.

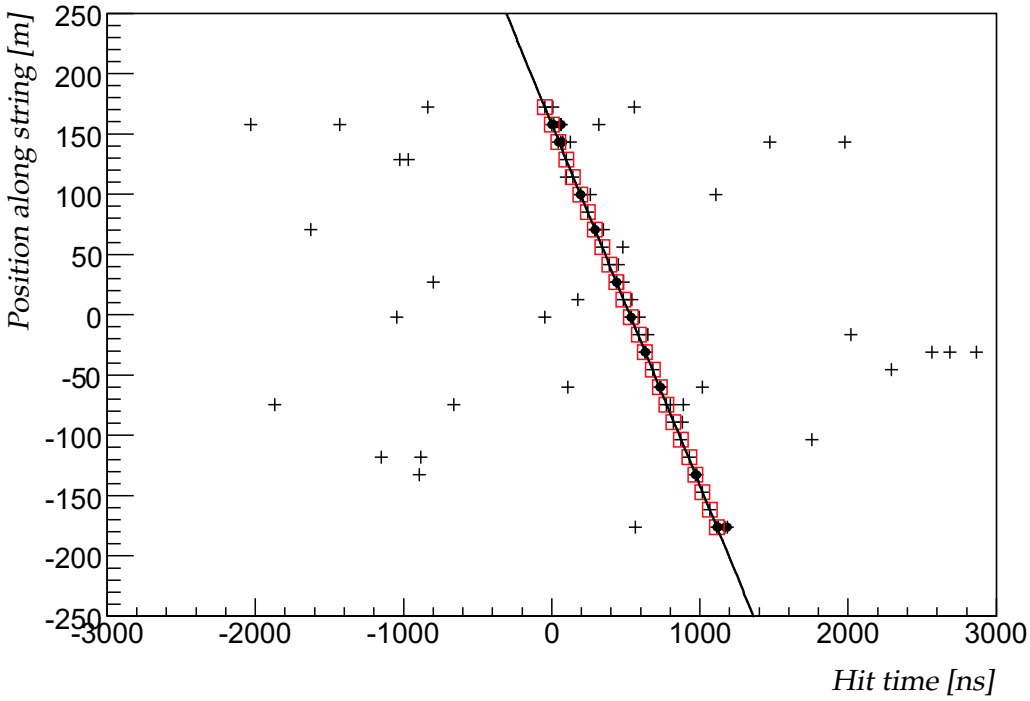

Figure 4.6: *z(t) relation for a vertically downward going reconstructed event.*

4.5 Electro-magnetic showers

Electro-magnetic showers occurring along muon tracks can show a particular signature in the detector. The first factor which contributes to this is the extension of a shower. The other factor is the angular distribution of the be emitted light. Light from an electro-magnetic shower can emitted in the complete 4π solid angle. Due

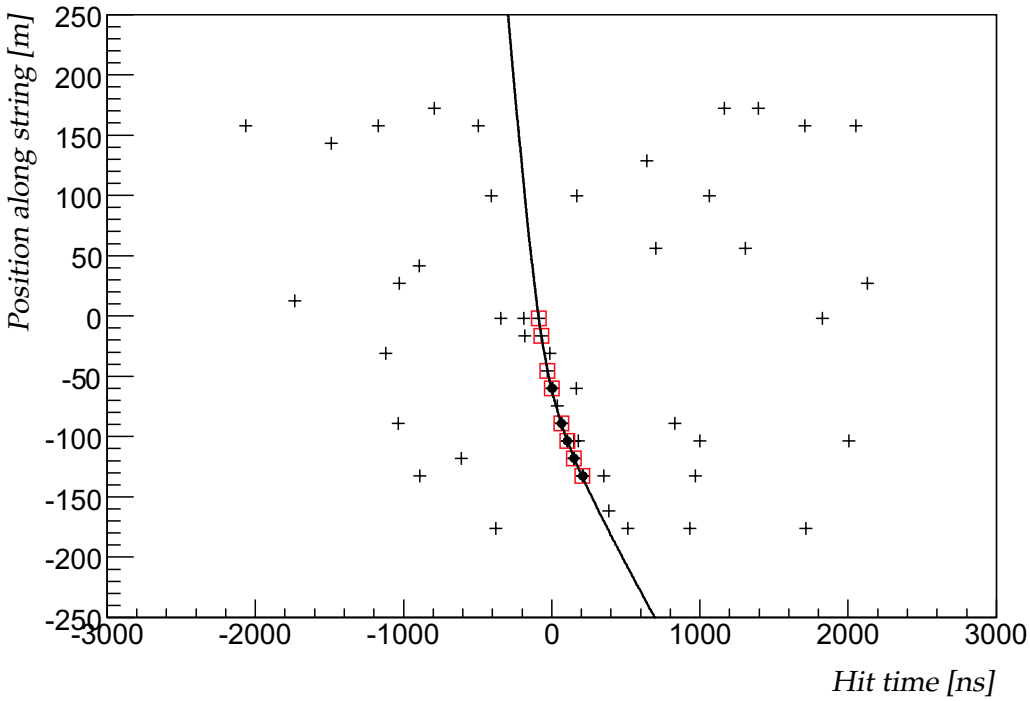

Figure 4.7: *z(t) relation for an event reconstructed with $\theta = 142$ degrees.*

to the small radiation length of water ($\sim$ 36 cm) a shower can be approximated by a point source of light. In case of a single detector line, the predicted time of a hit t_i on a optical module at position z_i along the line is given by

$$t_i = t_s + \frac{n}{c}\sqrt{d_s^2 + (z_i - z_s)^2} \tag{4.5}$$

Where t_s, z_s and d_s are the time at which the shower occurs, the height along the line and the distance from the line, respectively. The constant c is the speed of light and n the refractive index. Consider the case when $d_s^2 \ll (z_i - z_s)^2$. This occurs when the shower is close to the line or far below (above). The relation between the position and time at which the photons are detected is then linear. This linear relation between time and position is the same as the asymptotic solutions of the Cherenkov arrival time given in equation 4.4 for $\theta = \theta_c$ or $\theta = \pi - \theta_c$. Plot a) of figure 4.8 shows both the simulated z(t) relation for a muon traveling upwards with $\theta = \theta_c$ and an electro-magnetic shower occurring at 25 meters from the line. In the plots of figure 4.8, the effect of the attenuation of light with distance is ignored. Next, consider the case in which $\theta = \pi/2$ in equation 4.1, yielding

$$t_i = t_0 + \frac{\sqrt{n^2 - 1}}{c}\sqrt{d^2 + (z_i - z_0)^2} \tag{4.6}$$

This relation describes the arrival times of Cherenkov photons from a horizontal muon. It is very similar to equation 4.5. The equations differ only in the constant term in front of the square-root. Due to this similarity, a fit of a muon to a shower can result in a near-horizontal track with z_0 close to the position of the shower (z_s). The plots in figure 4.8 illustrate the z(t) relations of electro-magnetic showers and muons traveling in different directions. As can be seen from figure 4.8, electro-magnetic showers can introduce special complications when reconstructing down going muons. Photons originating from a shower and traveling in the upward direction are more likely to be detected than the direct Cherenkov photons originating from a downward going muon. This is a result of the downward orientation of the optical modules. Figures 4.9 and 4.10 show the z(t) relation of a reconstructed event. In both cases multiple solutions were found. In both figures the top plot shows the preferred solution of the reconstruction following the selection criterium introduced in chapter 3. The bottom plot shows an alternative solution with a zenith angle corresponding to a near horizontal direction. Again, the square boxes indicate the hits used for the reconstruction. The vertical solutions primarily contain Cherenkov hits from the muon while the horizontal solutions include hits from an electro-magnetic shower.

4.6 Residuals

In this section, a study of the hit time residuals will be presented. As defined in section 3.1, the hit time residual is the difference between the measured and predicted arrival time of a photon. The prediction of the arrival time is calculated assuming that the photon is emitted at the Cherenkov angle with respect to the muon direction. In the context of the reconstruction, there are two kinds of hit time residual distributions. The first kind of distribution contains all the hits that were present in the snapshot. In general, this includes background photons and late photons. The distribution of the time residuals of all hits in the event for real data is shown in figure 4.11. Several features can be distinguished. First, there is a large peak at $\Delta t = 0$ due to (direct) Cherenkov light. A second peak at about $\Delta t = 45$ ns reflects the effect of the second ARS, as explained in section 2.6.3. The tail $\Delta t \gg 0$ is due to effects such as light scattering and electro-magnetic showers. A small shoulder of negative time residuals is caused by mis-reconstructed tracks. The shoulder with positive residuals is due to the coincidence gate of the trigger, which is 20 ns. The random background can be recognised at very negative time residuals ($\Delta t \leq -100$ ns). In the second kind of distribution only the hits that are used in the reconstruction are considered. This distribution is influenced by the hit selection and hit removal procedures in the reconstruction algorithm. As explained in chapter 3 the reconstruction algorithm used in this study aims to maximize the purity of the hits with respect to the Cherenkov hypothesis. This will suppress the tail of the late photons. In the following, the

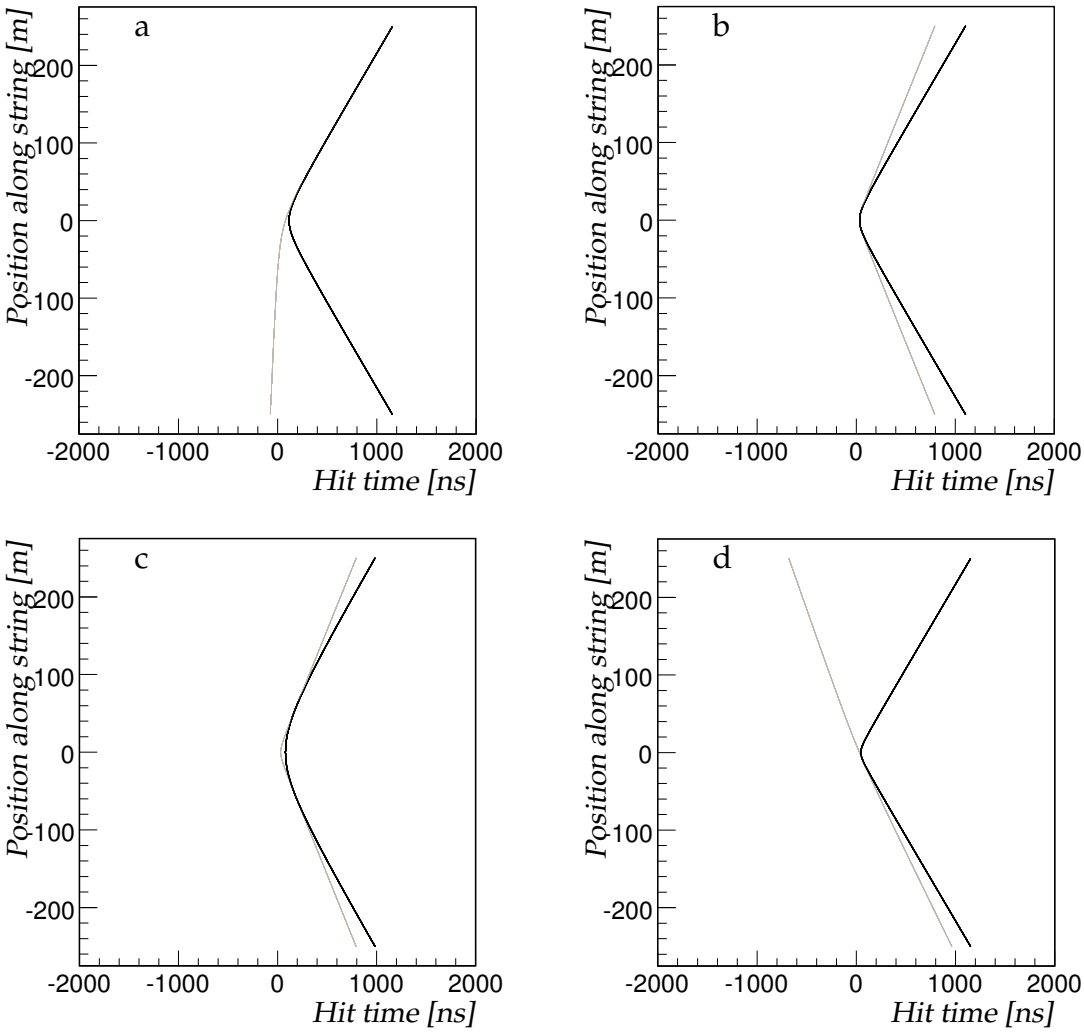

Figure 4.8: *Simulated z(t) relations for muons and electro-magnetic showers. The attenuation of the light is ignored.*
(a) A muon traveling upwards at $\theta = \theta_c$ degrees from vertical (grey line) at a distance of 25 meters for the line. An electro-magnetic shower occurs at the point of closest approach (black line).
(b) A muon traveling in horizontal direction at a distance of 10 meters from the line. An electro-magnetic shower at 15 meters from the line (black line).
(c) A muon traveling in horizontal direction at a distance of 10 meters from the line. An electro-magnetic shower at 60 meters from the line (black line).
(d) A muon traveling downwards with $\theta = 170^\circ$ at a distance of 10 meters from the line (grey line). A shower occurs at the point of closest approach (black line).

definition of a L1′-hit (see section 3.3.1) is used. With this definition of a hit, the distribution of time residuals is approximately Gaussian. When calculating the

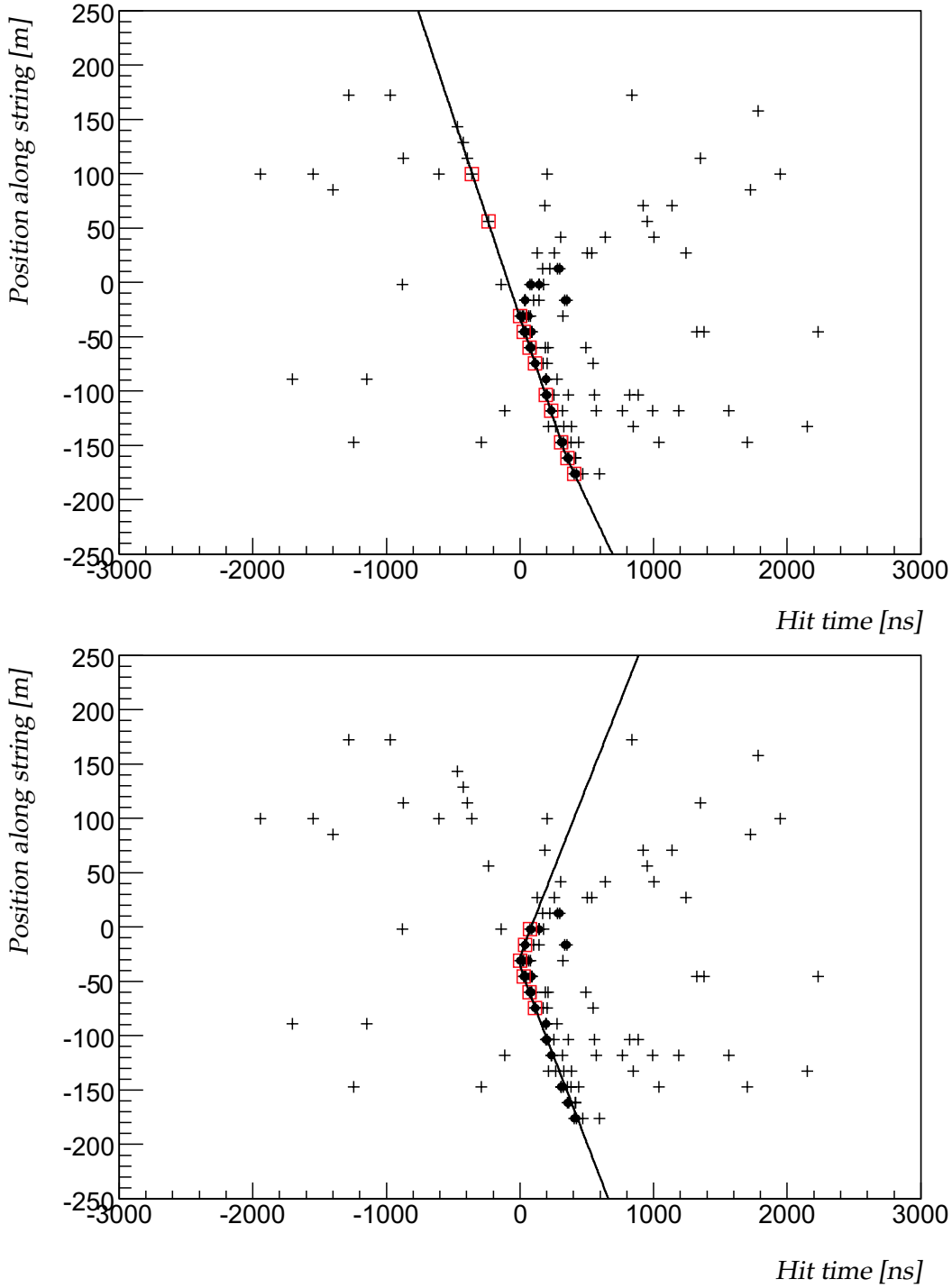

Figure 4.9: *Example of an event with multiple solutions. Top plot shows the preferred solution: a downward going muon with $\theta = 169°$. Bottom plot shows an alternative solution: a nearly horizontal going muon with $\theta = 89°$. See text.*

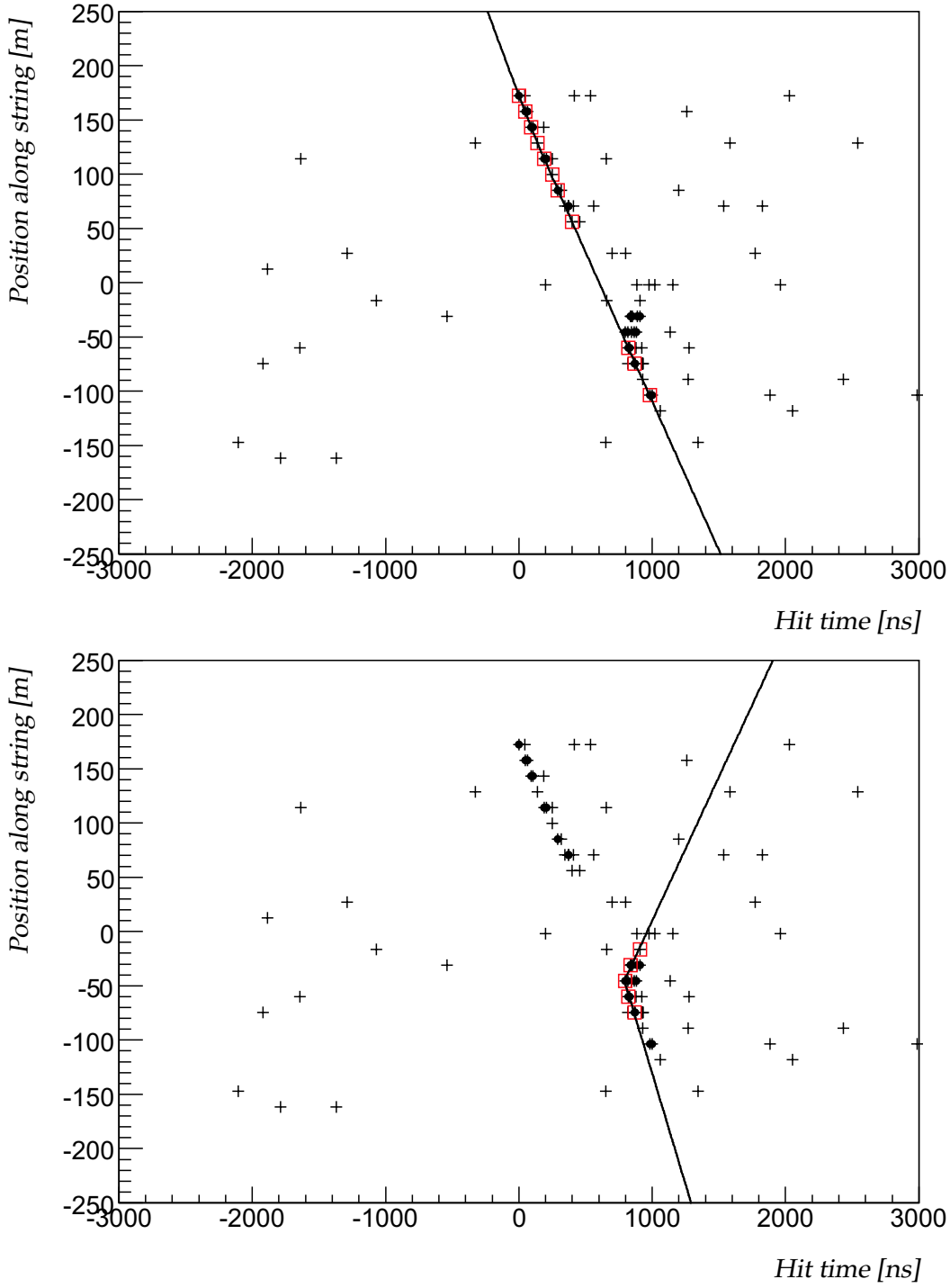

Figure 4.10: *Example of an event reconstructed with multiple solutions. Top plot shows the preferred solution: a downward going muon with* $\theta = 174°$*. Bottom plot shows an alternative solution: a nearly horizontal going muon with* $\theta = 78°$*. See text.*

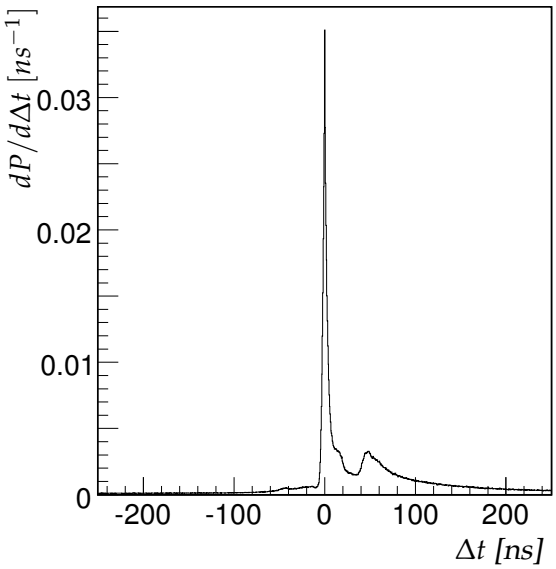

Figure 4.11: *Distribution of the time residuals for all hits in the event.*

residual, the predicted time of hit j, t_j^{th} depends on the estimated track parameters, i.e. $t_j^{th} = t_j^{th}(\vec{\theta})$. The track parameters are estimated by minimisation of the χ^2 in equation 3.4. In general, there are two scenarios to obtain the track parameters when calculating a residual.

Inclusive The hit j for which the residual is calculated is included in the minimization of the χ^2. This leads to a reduction of the dispersion of the time residuals. The underestimate becomes more prominent if the contribution of the term $(t_j - t_j^{th}(\vec{\theta}))^2$ in summation of equation 3.4 increases. This may occur when decreasing the number of hits in the sum. Of course, this pull of individual hits is also reflected in the quality of the fit, expressed as the angular residual. The dispersion on the time residuals can be small while the angular residual is large.

Exclusive The hit j for which the residual is calculated is excluded in the minimization of the χ^2. Equation 3.4 thus becomes

$$\chi^2(t_1, ..., t_n; \vec{\theta}) = \sum_{i=1, i\neq j}^{n} \frac{(t_i - t_i^{th}(\vec{\theta}))^2}{\sigma_i^2} \tag{4.7}$$

The estimated track parameters do not depend on hit j and the distribution of time residuals reflects the resolution of the hits and the accuracy of the estimated track parameters. The width of the distribution of time residuals is a result of several effects. First is the intrinsic time resolution of the measurement, indicated by σ_{int}. Second is the contribution from the error on the estimation of the track

parameters, indicated by σ_{track}. It can be calculated from the derivatives of the expected arrival times and the covariance matrix $V_{\vec{\theta}}$ of the track parameters and is given by

$$\sigma^2_{track} = \left(\frac{d\Delta t}{d\Delta\vec{\theta}}\right)^T V_{\vec{\theta}} \left(\frac{d\Delta t}{d\Delta\vec{\theta}}\right) \tag{4.8}$$

If the fit model and data agree, then these two contributions could be added quadratically, provided that the errors are Gaussian.

In figure 4.12 the inclusive and exclusive distributions of time residuals are shown. From figure 4.12 it can be seen that the exclusive distribution is broader than the inclusive, as expected. A fit of a Gaussian function in the region $-10 \leq \Delta t \leq 10$ ns gives a standard deviation of about 3.6 ns for the inclusive distribution and 5.3 ns for the exclusive distribution. As the accuracy of the fit parameters depends on the number of hits used in the fit, the same distributions are studied as function of the number of hits. Following the definition of a L1' hit (see section 3.3.1) the number of hits is equal to the number of storeys. The distributions are determined for different numbers of hits used in the fit. For inclusive residuals, this number can be as high as the maximum number of floors in the line, so 25. For exclusive residuals the maximum is 24, as the hit for which the residual is calculated is excluded. To each of the distributions a Gaussian function is fitted and the width is determined. Figure 4.13 shows the fitted widths of the distributions as function of the number of hits used in the fit. At small number of hits, several effects contribute to the width of the distributions. The dominant effect is the degradation of the fit. This effect is exacerbated by the occurrence of electro-magnetic showers and multiple muons in the event. As can be seen from figure 4.13 the inclusive residuals are affected significantly less by these effects. The different processes that contribute to the time residuals can be disentangled by a Monte Carlo simulation. Figure 4.14 shows the standard deviations of the exclusive distributions as function of numbers of hits using simulated data. The open circles include all processes and can be compared with the black circles in figure 4.13. This comparison shows a reasonable agreement between data and Monte Carlo. The squares in figure 4.14 correspond to the distributions obtained by excluding all hits caused by electro-magnetic showers in both the fit and the calculation of the time residuals. It can be seen from figure 4.14 that the distributions of the time residuals improve. This can be understood because the fit model agrees better with the selected data. The improvement is most prominent at small numbers of hits. The triangles in figure 4.14 are obtained by excluding hits from electro-magnetic showers and by selecting hits from a single track in the atmospheric shower. In this way, the fit model agrees with the selected data. Indeed, the distributions of time residuals become narrower. The only remaining effect is the possible scattering of the photons. The residual is then determined by the uncertainty of the fit (see equation 4.8).

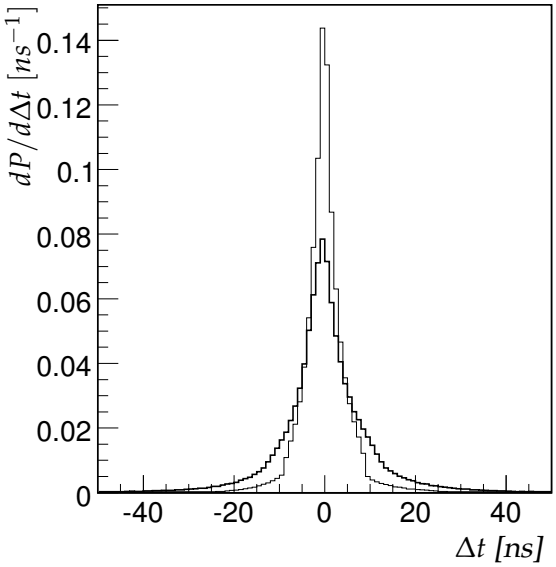

Figure 4.12: *Distribution of the time residuals obtained from real data. The black lines indicate exclusive residuals and the grey lines indicate inclusive residuals.(See text.)*

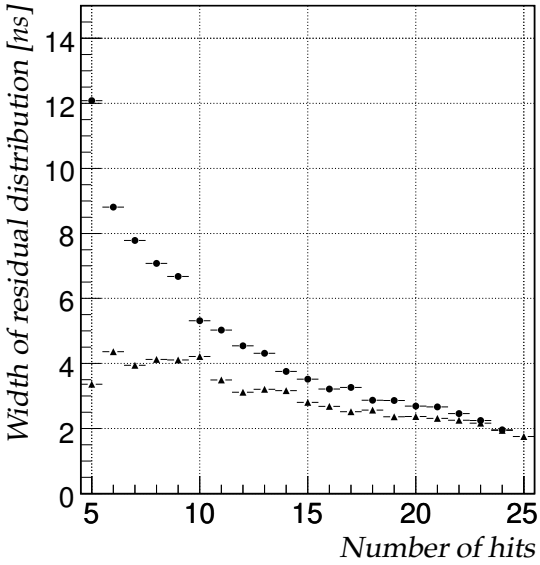

Figure 4.13: *Fitted widths of the distributions of time residuals as function of the number of hits used in the fit obtained from data. The symbols correspond to ● : exclusive residuals, ▲ : inclusive residuals.*

4.7 Zenith angle distribution

In this section the zenith angle distribution of reconstructed muons will be presented. This distribution is the result of several factors, in particular the particle flux, the detection efficiency and the reconstruction. The fluxes show a dependence on zenith angle. The muon flux originates from atmospheric showers and dominates the total flux. The detection efficiency depends on the zenith angle. The main effect is due to the geometry of the detector. Muons traveling in a near vertical direction can pass within a detectable distance from the line. Consequently, they will have a larger probability to cause hits on several floors compared to a muon traveling in a more horizontal direction. The effect of the ori-

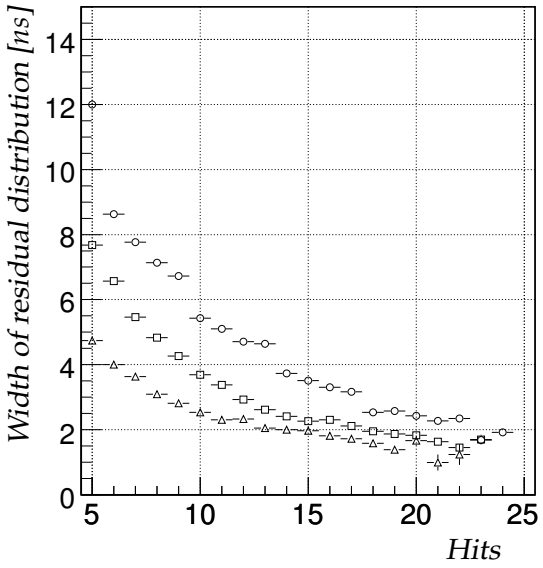

Figure 4.14: *Fitted widths of the exclusive distributions of the time residuals as function of the number of hits used in the fit obtained from simulated atmospheric muon data. The symbols correspond to ∘ : all hits, □ : only Cherenkov hits, △ : only Cherenkov hits from single tracks*

entation and the acceptance of the optical modules has been discussed in section 4.3.2. In general, the measured zenith angle of the muon differs from the actual angle. As a result of the finite angular resolution the zenith angle distribution will be smeared. Hits caused by electro-magnetic showers along the tracks, possibly complemented with other hits can cause wrong reconstruction of the track (see section 4.5). When only part of the Cherenkov cone is seen, the muon can be reconstructed at an angle $2\theta_c$ with respect to the actual muon track (see section 4.1).

4.7.1 Monte Carlo simulation

In order to estimate the effect of the angular resolution, ghost solutions and electromagnetic showers, a Monte Carlo simulation of the detector response to muons is made. The angular residual ($\Delta\theta$) is defined as the difference between the reconstructed zenith angle (θ_{fit}) and true zenith angle (θ_{true}) :

$$\Delta\theta = \theta_{true} - \theta_{fit} \tag{4.9}$$

This quantity is related to the angular residual defined in formula 3.21 by

$$\Delta a_\mu = |\Delta\theta| \tag{4.10}$$

The distribution of $\Delta\theta$ for atmospheric muons is shown in figure 4.15. In this, the events are weighted with their expected rate. The different shaded zones in the distribution indicate the contributions of events reconstructed with less than 7 hits (dark grey), 7 or 8 hits (white) and 9 or more hits (light grey). The asymmetric tail is due to mis-reconstructed events. There is a contribution of events containing hits from electro-magnetic showers and a contribution of ghost

solutions. It can be seen from figure 4.15 that the events in the tail show a small number of hits used in the fit. The median value of $|\Delta\theta|$ is about 9 degrees. As can be seen from figure 4.15 the median of the $|\Delta\theta|$ distribution decreases rapidly with increasing number of hits used in the fit. For 10 or more hits used in the fit the median is about 1.7 degrees. The dependence of the angular residual on the reconstructed zenith angle is shown in figure 4.16. The asymmetric distribution of the tail of figure 4.15 contains events that are preferably reconstructed with a zenith angle less than 120 degrees. As can be seen from figure 4.15, these events are in general reconstructed with a small number of hits.
It can be concluded that for atmospheric muons a cut on the number of hits is an effective way of improving the angular residual. It largely eliminates the tail of events that are reconstructed with a wrong zenith angle. The mis-reconstructed events could be mistakenly regarded as upward going neutrino events.
The $\Delta\theta$ distribution for upward going atmospheric neutrino events is shown in figure 4.17. The distribution is reasonably symmetric. The median of the $|\Delta\theta|$ distribution has a value of about 3.9 degrees. Requiring at least 10 hits used in the fit improves the median to about 1.1 degrees.

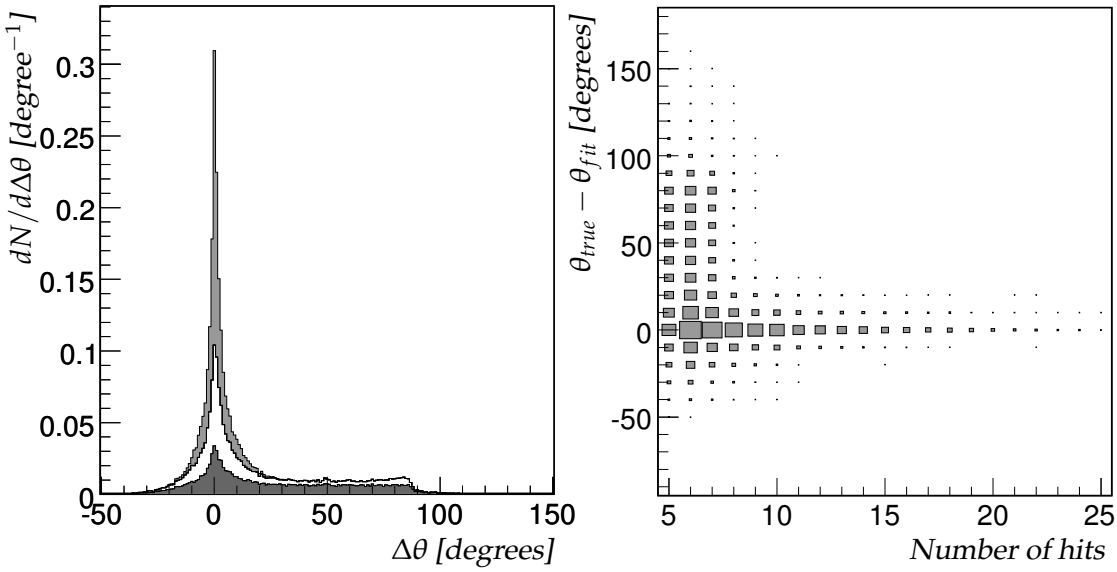

Figure 4.15: *Left: Distribution of the angular residual for atmospheric muons. Different shades indicate the numbers of hits used in the fit. Dark grey : 5-6, white : 7-8, light grey : > 8. Right: Angular residual as a function of the number of hits used in the fit.*

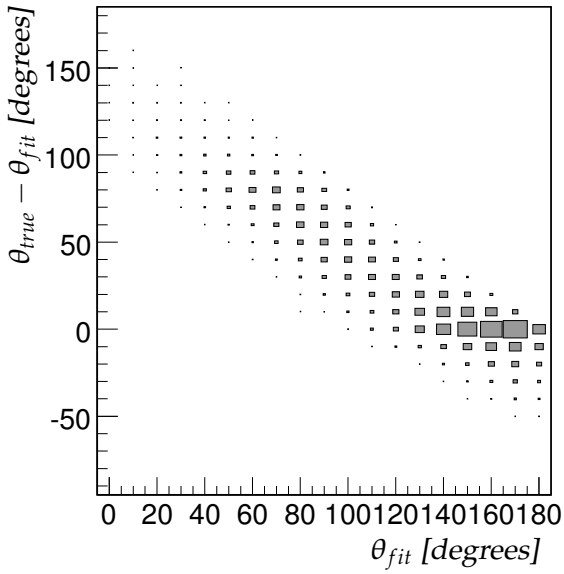

Figure 4.16: *Angular residual as function of the reconstructed zenith angle for atmospheric muons.*

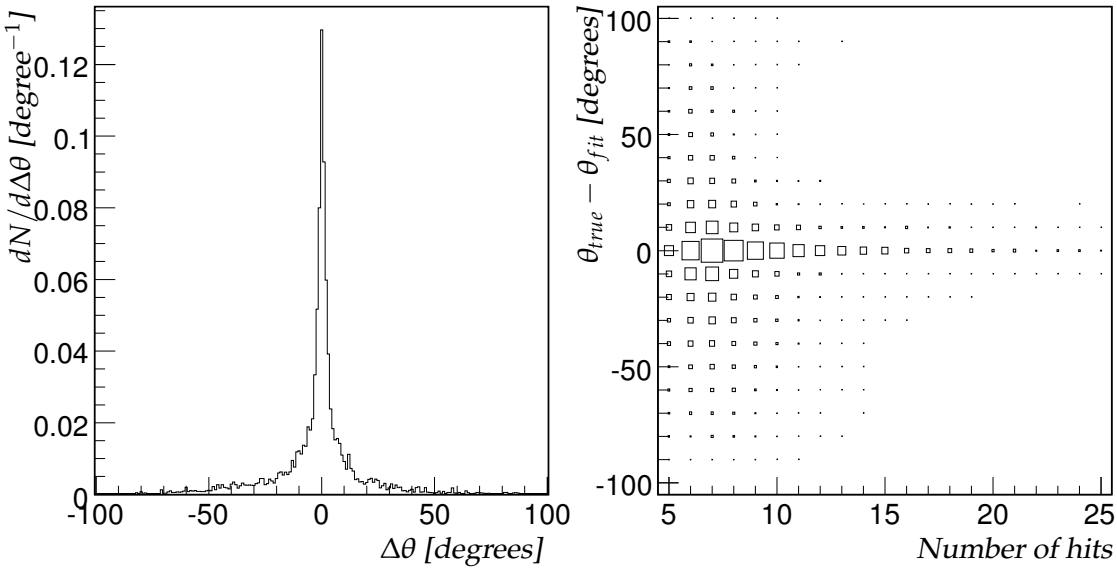

Figure 4.17: *Left: Distribution of the angular residual for atmospheric neutrino events. Right: The angular residual as function of hits used in the fit.*

4.7.2 Measured muon rate

In figure 4.18 the muon rate as function of the cosine of the zenith angle is shown. In the figure, both the measured and the simulated data sets are shown. The simulated data set consists of the atmospheric muons presented in section 4.3.4. The same selection is applied to both the data and the Monte Carlo data. The

requirement for an event to be included is that at least 5 hits, and thus 5 storeys, were used to reconstruct the event. The measured data points only have statistical errors drawn. The band drawn for the simulated data contains the systematic error due to the angular acceptance of the optical modules and the statistical error. The distributions of data and Monte Carlo simulation agree reasonably well. The

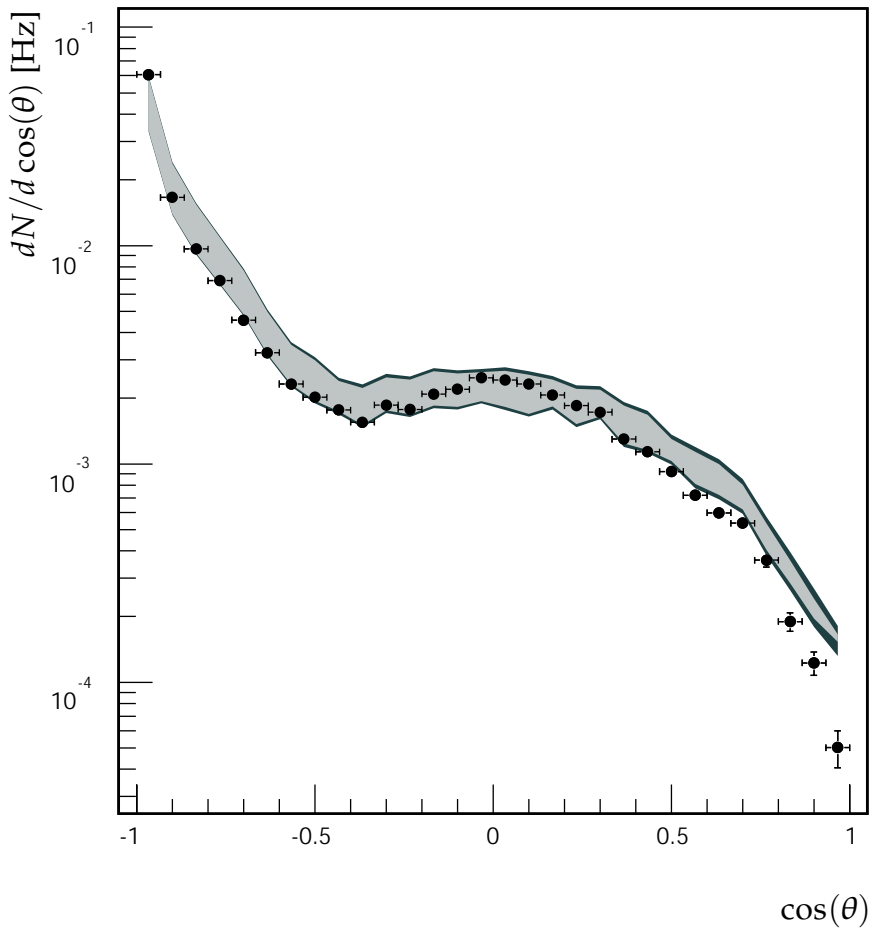

Figure 4.18: *Measured muon rate as function of the cosine of the reconstructed zenith angle. The points correspond to the data. The band corresponds to the Monte Carlo simulation. The width of the band indicates the systematic error (light grey) and the statistical error (dark grey).*

distribution is strongly peaked at $\cos(\theta) = -1$ which corresponds to the vertical downward direction. This confirms the general picture that the muon flux is dominated by atmospheric muons. The bump occurring between $\cos(\theta) = -0.5$ and $\cos(\theta) = 0.5$ reflects the tail in the $\Delta\theta$ distribution from figure 4.15.

4.7.3 Angular resolution from data

The Antares detector is built up of identical detection units, the storeys. Any set of the storeys can be regarded as a detector. This means that the detector can be split in parts to perform consistency checks and cross-calibrations. This section describes an estimation of the angular resolution. In order to facilitate the estimation of the resolution, the detector line can be split in two parts with nearly identical properties. These two parts are denoted by A and B, each consisting of a set of storeys. Zenith angles reconstructed with set A (B) are referred to as θ_A (θ_B). In order to estimate the angular residual from the real data, the difference between the reconstructed zenith-angles using sets A and B is studied :

$$\Delta\theta_{A-B} = \theta_A - \theta_B \tag{4.11}$$

The uncertainty of θ_A and θ_B are assumed to be equal and are denoted by $\Delta\theta_{A/B}$. Assuming a Gaussian distribution of $\Delta\theta_{A/B}$, the standard deviations of $\Delta\theta_{A/B}$ and $\Delta\theta_{A-B}$ are related by

$$\sigma_{\Delta\theta_{A/B}} = \sigma_{\Delta\theta_{A-B}}/\sqrt{2} \tag{4.12}$$

For a Gaussian distribution, the median of the absolute deviation is related to the standard deviation by a numerical factor, thus

$$median(|\Delta\theta_{A/B}|) = median(|\Delta\theta_{A-B}|)/\sqrt{2} \tag{4.13}$$

For this study, Line 1 was split up in two different ways. For the first split, the odd floor numbers belong to set A, the even floor numbers to set B. This way of splitting is referred to as the *even/odd* split. The other split divides the line in a top and bottom part. The top 13 floors belong to set A, the remaining 12 floors belong to set B. This way of splitting is referred to as the *top/bottom* split. The number of events reconstructed with each of the subsets are summarized in table 4.3. The third row in the table gives the number of events that were reconstructed for both subsets. The numbers in this row correspond to the events that can be used to estimate the angular resolution. Thus for the *even/odd* split, 4007 events are reconstructed in both subsets and for the *top/bottom* 2211 events. The yield of reconstructed events differs significantly between the *even* and *odd* sets and between the *top* and *bottom* sets. This is linked to the numbers of working optical modules in each of the subsets. In total there were six optical modules which have no recorded data in the selected data sample. Only one out of these six was on an *odd* floor, and four out of the six were located in the *top* half of the detector.

The measured distributions of $\Delta\theta_{A-B}$ are shown in figure 4.19. The median of the $|\Delta\theta_{A-B}|$ distribution of the *top/bottom* sets is about 11.8 degrees, while for the *even/odd* sets it is about 3.7 degrees. This gives a median angular residual for the

even	8001	top	29075
odd	12172	bottom	37142
even & odd	4007	top & bottom	2211

Table 4.3: *Numbers of reconstructed events for different sub-divisions of the Line 1.*

top or bottom set of about 8.4 degrees and for the even or odd set of about 2.6 degrees. It should be noted that the *even/odd* sets span a larger length of the detector line. A larger length of the track reduces both the probability of a ghost solution and the influence of electro-magnetic showers along the track. The *top/bottom* sets correspond to different parts of the track. Hence, an electro-magnetic shower affects usually one of the sets. This can result in a large difference between the reconstructed zenith angles. The effect of the χ^2 probability and the number of hits used in the fit is also studied. In figure 4.20, the median of the $|\Delta\theta_{A-B}|$ distribution is shown as function of the minimum number of hits used in the fit (with and without a cut on the χ^2 probability). The requirement of the minimum number of hits is on *both* fits. For the cut on the χ^2 probability of larger than one percent, a resolution 1.75 ns is assumed. The medians of $|\Delta\theta_{A-B}|$ decrease when more hits are required for the fit. This decrease is consistent with figure 4.15. For the *top/bottom* split the angular residual drops below 3 degrees when at least 10 hits are required. For the *even/odd* split, the angular residual drops below 1 degree. According to formula 4.13 this leads to a median angular residual of about 2.1 degrees for the *top/bottom* split and about 0.7 degrees for the *even/odd*. This implies that the resolution of the complete line, thus when combining the even and odd parts, can reach about 0.5 degrees.

4.8 Vertical muon intensity

The reconstructed number of events as function of $\cos(\theta)$ is shown in figure 4.18. The number of detected events in a $\cos(\theta)$ bin i depends on the muon flux $\mathcal{F}_i$ in that bin and the detector acceptance. The detector acceptance includes the detection efficiency and the effects from the reconstruction. The detector acceptance can be described by a two-dimensional matrix R_{ij}, as events can migrate to a different bin due to the finite angular resolution. With $\mathcal{N}$ bins covering $\cos(\theta) \in [-1, 1]$, the measured rate F_i is related to the flux by

$$F_i = \sum_{j=0}^{\mathcal{N}} R_{ij}\mathcal{F}_j \tag{4.14}$$

When the angular resolution is small compared to the bin size the off-diagonal elements of R_{ij} will be close to zero, i.e. $R_{ij} = 0$ for $i \neq j$. In this case the matrix

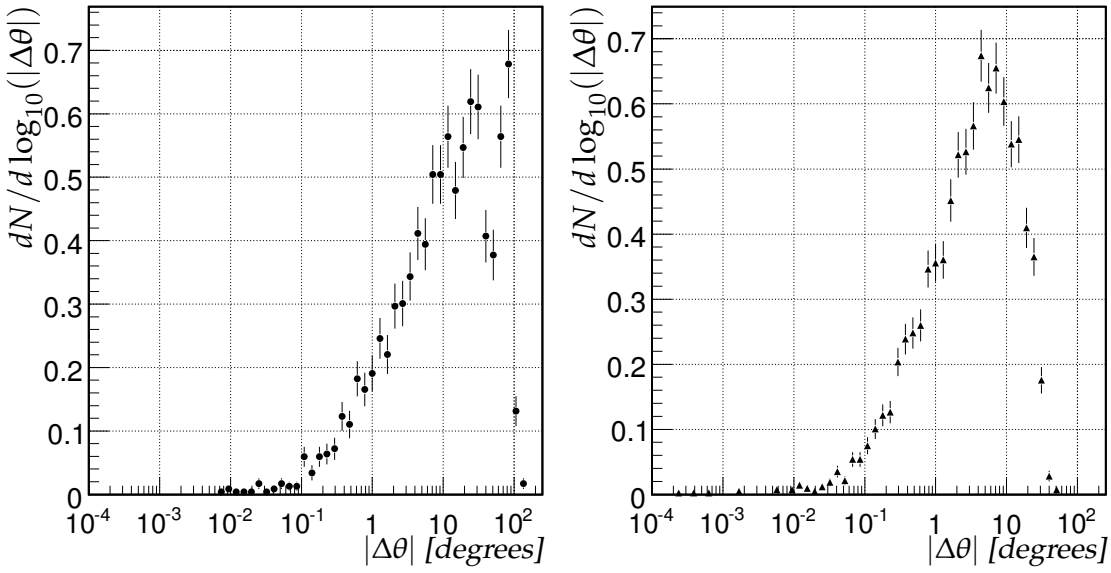

Figure 4.19: *Distributions of the angular residual $|\Delta\theta_{A-B}|$ between the results of the reconstruction with the line split up in a top and bottom part (left) or an even and odd part (right).*

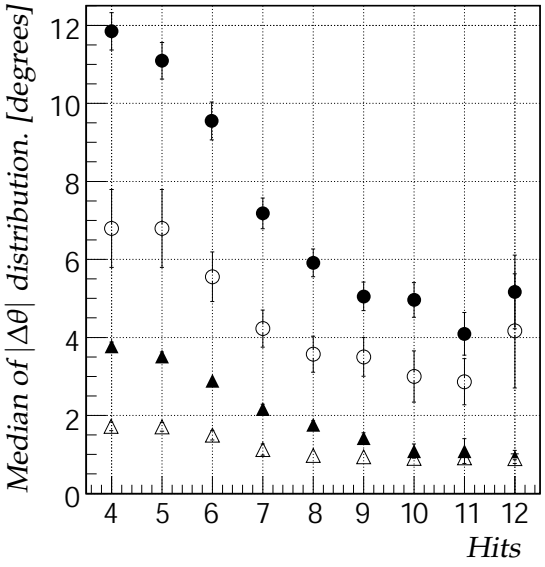

Figure 4.20: *Medians of the distributions of the angular residual ($|\Delta\theta_{A-B}|$) between the different reconstructions with the line split up in a top and bottom part (circles) or an even and odd part (triangles). Plotted as function of the minimum number of hits used in both lines. The open symbols have a cut on χ^2 probability of greater than one percent applied.*

R_{ij} becomes a 1 dimensional vector R_i and equation 4.14 reduces to

$$F_i = R_i \mathcal{F}_i \tag{4.15}$$

The flux can be determined if R_i is known by

$$\mathcal{F}_i = \frac{F_i}{R_i} \tag{4.16}$$

The values of R_i can be estimated from a simulation of the detector response to muons. From the simulation, the muon flux $\mathcal{F}_i^{sim}$ and the simulated rate F_i^{sim} are then known. The detector response R_i^{sim} can then be determined by the ratio of F_i^{sim} and $\mathcal{F}_i^{sim}$:

$$R_i^{sim} = \frac{F_i^{sim}}{\mathcal{F}_i^{sim}} \tag{4.17}$$

It should be noted here that R_i^{sim} is not an unbiased quantity and in general differs from the true detector response R_i. The reason for this is that it is derived from a simulation, which includes an assumed flux. Hence, R_i^{sim} can be considered as the detector acceptance for an *assumed flux*. This correction includes muons which are below detection threshold.

For this work, the muon flux is obtained with the parametric simulation MUPAGE, described in section 2.10.2. In figure 4.21 the values of R_i^{sim} for the different $\cos\theta$ bins are shown. The cross-bars on the errors indicate the systematic error due to the angular acceptance of the optical modules. With increasing $\cos(\theta)$, the values of R_i^{sim} change gradually with a maximum deviation between two consecutive bins of about a factor two. For values of $\cos(\theta)$ in excess of -0.5 the correction factor increases rapidly because of an overestimation of the true detected rate due to bin migration. The bins with $\cos(\theta) > -0.5$ are increasingly contaminated with wrongly reconstructed events due to showers and ghost solutions. For the estimation of the vertical muon flux the bins with $\cos(\theta) > -0.5$ are excluded. By replacing R_i by R_i^{sim} in equation 4.16, the muon flux for the different $\cos(\theta)$ bins can be determined. The result is shown in figure 4.22. Each value of the zenith angle corresponds to a certain slant depth through the water mass above the detector. The measured muon flux can also be given as a function of slant depth. In order to calculate the muon vertical intensity, the distribution of muons at sea level has to be taken into account. This distribution (see reference [79]) is given by

$$\frac{dN_\mu}{dE_\mu} \approx \frac{0.14 E_\mu^{-2.7}}{cm^2\ s\ sr\ GeV} \left(\frac{1}{1 + \frac{1.1 E_\mu \cos(\theta)}{115 GeV}} + \frac{1}{1 + \frac{1.1 E_\mu \cos(\theta)}{850 GeV}} \right) \tag{4.18}$$

For a given value of $\cos(\theta)$ formula 4.18 is integrated over the energy range from 2 TeV to 10 PeV and the relative values are used to correct the vertical muon intensity. The resulting depth-intensity relation of the vertical muon intensity is shown in figure 4.23. The results obtained in this analysis agree well with those obtained in other experiments.

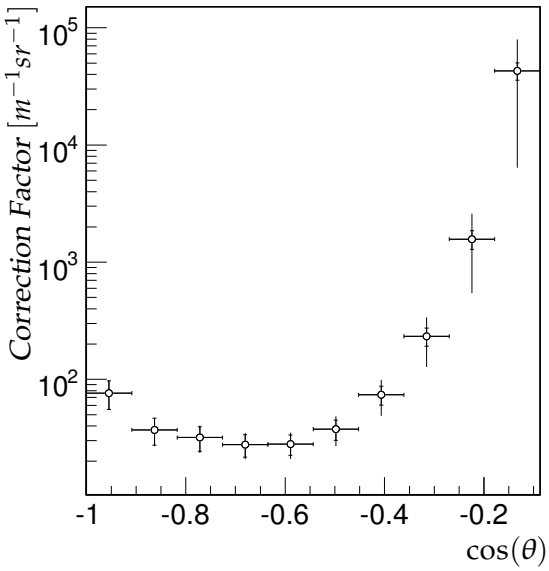

Figure 4.21: *Correction factor R_i^{sim} as function of the cosine of the reconstructed zenith angle. The vertical cross-bars indicate systematic errors. The horizontal cross-bars indicate the bin size.*

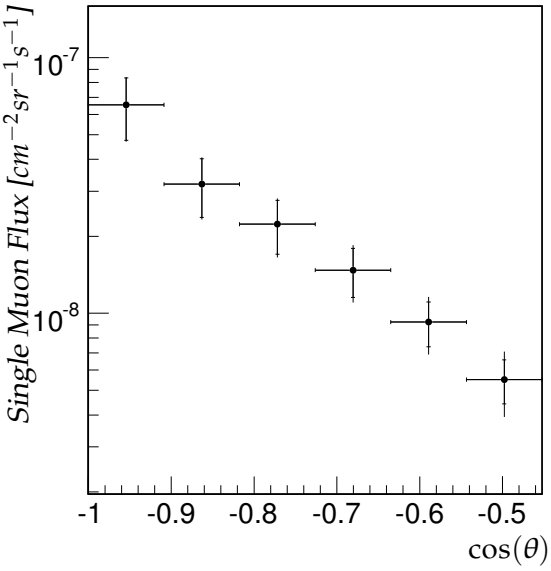

Figure 4.22: *Single muon flux as function of $\cos(\theta)$ corrected for the detector acceptance. The vertical cross-bars indicate the systematic errors. The horizontal cross-bars indicate the bin size.*

4.9 Neutrino candidates

From the simulation, it is expected that the reconstructed event sample should contain a small number (≈ 4) of upward atmospheric neutrino-induced events. However, there are 9515 upward reconstructed events. These events are dominated by mis-reconstructed atmospheric muon events (see section 4.7). There are two main quantities which give a handle on the angular resolution of the reconstructed events and the purity of the upward reconstructed events, namely the number of hits used in the reconstruction and the χ^2 probability of the final fit. From the data and simulation, events have been selected which are reconstructed as upward going and have a χ^2 probability greater than one percent. In figure 4.24

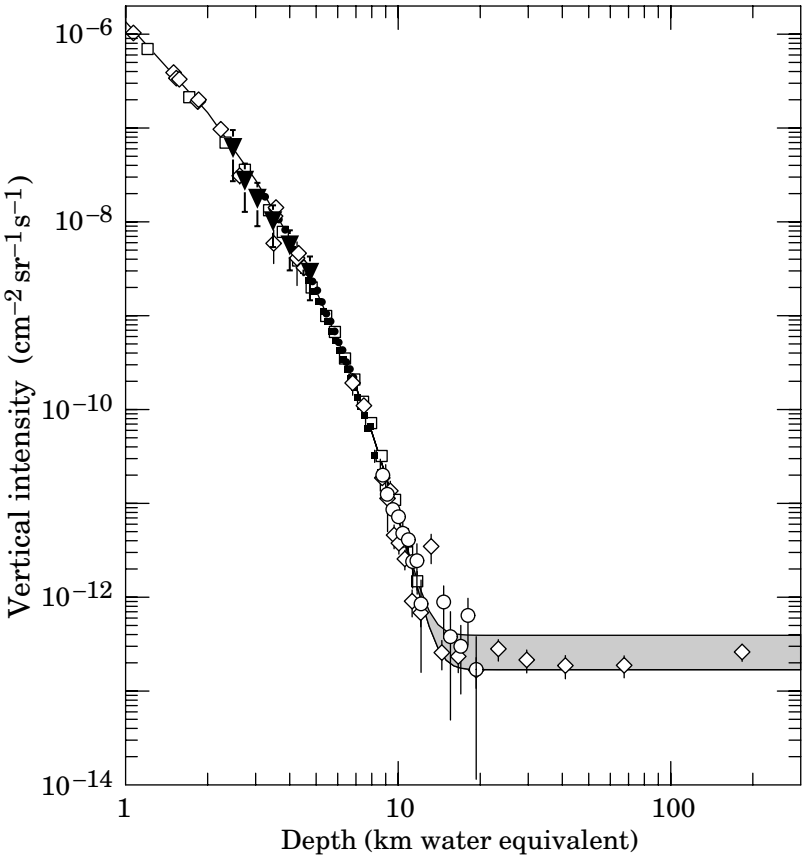

Figure 4.23: Vertical muon intensity versus depth. ▼ : This work. Plot taken from [14].

the number of remaining events is shown as a function of the minimal number of hits used in the final fit. The data agree reasonably well with the simulation of atmospheric muons. The simulation indicates that there are no atmospheric muons to be expected with more than 9 hits used in the reconstruction. The data contain one event that is reconstructed with 10 hits. This event is consistent with the predicted atmospheric neutrino flux. Figure 4.25 shows the display of this event. The hits used in the fit are found above and below the point of closest approach to the line, which are both L0 and L1 hits. There is no apparent signature of an electro-magnetic shower, confirming that this event can be considered as a neutrino induced muon.

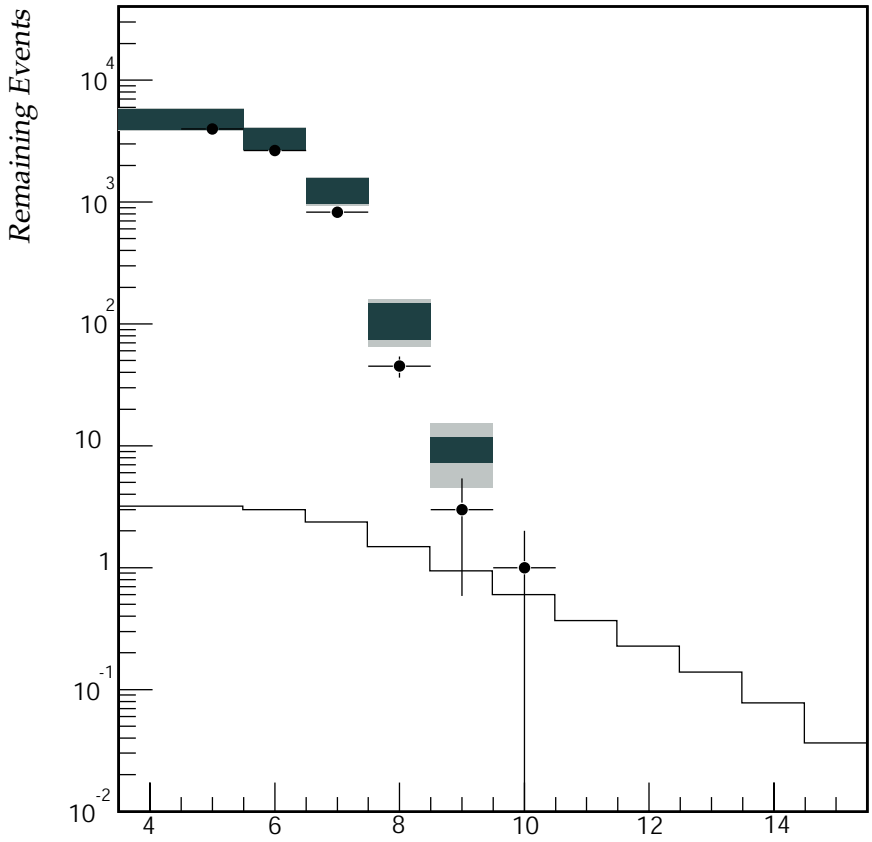

Figure 4.24: *Remaining number of events reconstructed as upward going as function of the minimum number of hits used in the fit. The points correspond to the data, the grey bands to the contribution from wrongly reconstructed atmospheric muons and the histogram to the contribution from genuine upward going atmospheric neutrino events. The height of the dark grey bands indicates the systematic error, the light grey bands correspond to the total error.*

4.10 Conclusions

An analysis was performed on the data of the first detector line of the Antares neutrino telescope. Monte-Carlo simulations were done to enable a confrontation with data and to evaluate the performance of the detector and track reconstruction. As the main signal consists of atmospheric muon tracks, the analysis was mainly focused on these events. After determining the detector response, the vertical muon intensity as function of depth in water could be constructed. The measured vertical muon intensity is consistent with other experiments (see for example [14]). Also, a search for neutrino candidates was done, resulting in

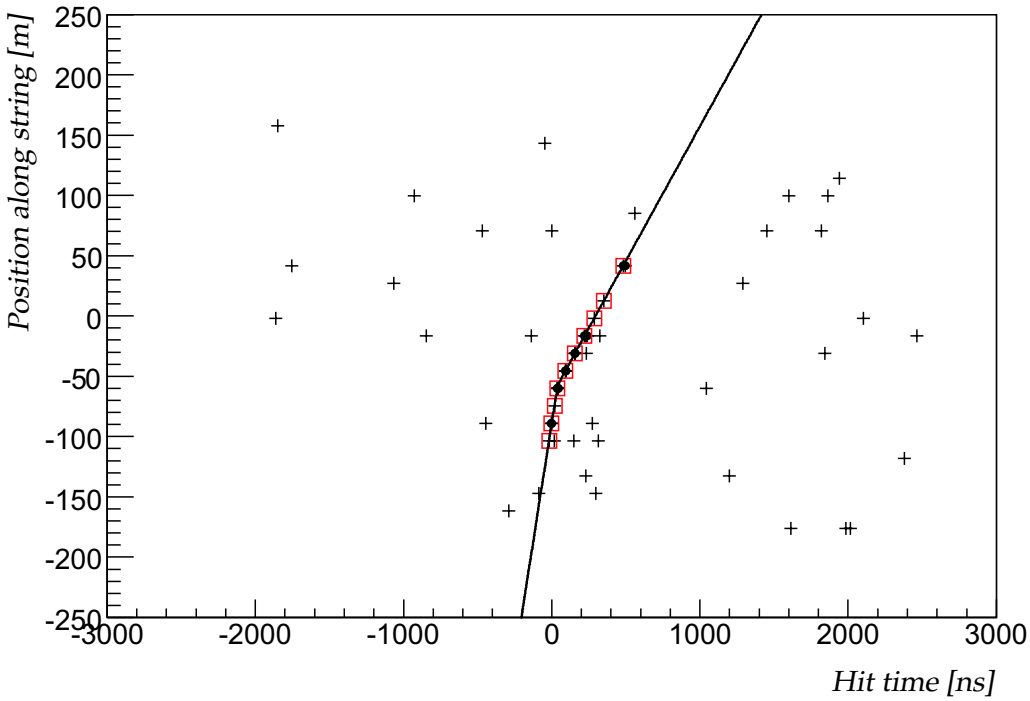

Figure 4.25: *Neutrino candidate event. The reconstructed zenith angle is* $\theta = 30°$.

one candidate.

The occurrence of electro-magnetic showers along muon tracks is the leading contribution to the error in the determination of the zenith angles of muon tracks. This is emphasized for atmospheric muons due to the orientation of the optical modules. A bias to more horizontal zenith angles is introduced when hits from electro-magnetic showers are included in the hit selection. This effect contributes to atmospheric muon events being falsely identified as upward going events. The resemblance of electro-magnetic shower dominated events to horizontal tracks leads also to an underestimation of the χ^2 error. The fraction of electro-magnetic shower events can be significantly reduced by requiring a minimum number of hits used in the fit due to the local nature of these events. The distribution of the residuals of hit times and its dependence on the number of hits used in the fit agree well between simulation and data. The contributions of electro-magnetic showers and muon bundles to the distributions of the hit time residuals were identified in simulation. These contributions were found to be significant at lower numbers of hits used in the track fit. While the simulation of photon arrival times seems to be in good shape, there is an uncertainty in the angular acceptance of the optical modules. This uncertainty introduces a systematic error in the estimation of event rates and detector acceptance. The measured rates are largely within

these errors.

The angular resolution of the detector line was studied by making use of the atmospheric muon data, without relying on simulation. A resolution of better than 1 degree for the zenith angle can be achieved without even utilizing the whole line. The estimate of the resolution of the complete detector ($< 0.3^\circ$, see chapters 3 and 5) seems realistic. Also because of the good agreement between the simulated measured distributions of the hit time residuals.

Chapter 5

Detector performance

The performance of the full 12 line detector in the presence of background from atmospheric muons and random noise has been evaluated. For this purpose, the track reconstruction algorithm developed in this work is used. Neutrinos are considered as the exclusive source of upward going muons. Atmospheric muons thus only pose a background when the track reconstruction wrongly identifies these events as upward going. As these tracks are wrongly reconstructed, this should be reflected in quantities correlated to the quality of the fit. Cosmic neutrinos are only distinguishable from atmospheric neutrinos by their energy (harder spectrum for cosmic) or by association of their direction with a cosmic source. The aim is thus to reduce the background from atmospheric muons and random noise to below the level of the atmospheric neutrinos. The influence of the rate of random background is studied in detail.

In chapter 4, an analysis of the data from the first Antares detector line was presented. In that analysis, the result from a χ^2 minimization procedure was used. This requires the minimum amount of knowledge of the detection medium and apparatus, as it assumes the light to be emitted at the Cherenkov angle. For the analysis presented in this chapter, a likelihood fit is applied after the χ^2 minimization (see chapter 3).

This chapter starts with an introduction to the Monte Carlo simulation. Several quantities are identified which can be used to reduce the background. Finally, the efficiency and accuracy of the detector are evaluated after applying various cuts.

5.1 Monte Carlo

The simulated data samples used in this study are generated as described in chapter 2. Three separate data-sets are used. These are upward going neutrinos, downward going atmospheric muons and events from random background. These sets were generated for three levels of random background, those being

Rate	60 kHz	120 kHz	240 kHz
Livetime	173015.70 s	144179.75 s	86507.85 s
Triggered	3	4041	1526612
Reconstructed	1	623	187817
$\cos(\theta) > 0$	0	266	84561

Table 5.1: *Sample of simulated random background events used in this study.*

Rate	60 kHz		120 kHz		240 kHz	
Type	ν_μ	$\bar{\nu}_\mu$	ν_μ	$\bar{\nu}_\mu$	ν_μ	$\bar{\nu}_\mu$
Generated	$13 \cdot 10^{10}$	$13 \cdot 10^{10}$	$13 \cdot 10^{10}$	$13 \cdot 10^{10}$	$13 \cdot 10^{10}$	$13 \cdot 10^{10}$
$N_{photons} \geq 10$	255340	269587	255238	269270	255340	269373
Triggered	150544	156916	151082	157602	203498	214318
Reconstructed	145125	151243	135515	140660	134185	139501

Table 5.2: *Sample of simulated neutrino events used in this study.*

60 kHz, 120 kHz and 240 kHz per photo-multiplier tube. The grid size used in the reconstruction of the events at 60 and 120 kHz is set to 5 degrees. This is the same as in chapter 3. For the events with a background of 240 kHz, this grid size would lead to a prohibitively long time needed for the reconstruction with respect to the data-taking. Therefore the grid size is set to 10 degrees. Also for 240 kHz, the maximum transverse distance between two hits is reduced from 90 to 75 meters, which increases the purity of the hits. The characteristics of the samples are listed in tables 5.1, 5.2 and 5.3. In these tables, the label 'Rate' corresponds to the random background rate. In table 5.1, the label 'Livetime' corresponds to the effective livetime of the sample. The label 'Generated' corresponds to the total number of events generated and the label '$N_{photons} \geq 10$' corresponds to the number of events causing 10 or more detected photons. The numbers of triggered and reconstructed events are given in the rows with label 'Triggered' and 'Reconstructed', respectively. The label '$\cos(\theta) > 0$' corresponds to the events that are (wrongly) reconstructed as upward going. Neutrino events are generated according to a spectrum proportional to $E_\nu^{-1.4}$. By applying different weights to the events (see section 2.10.1), the sample of neutrinos can represent the atmospheric neutrino flux as well as any other assumed signal flux. The standard signal flux is taken to be proportional to E^{-2}.

5.1.1 Angular acceptances

In section 2.6.1, three parameterisations of the angular acceptance of the optical modules were introduced. The differences between these three parameterisations

Rate	60 kHz	120 kHz	240 kHz
Generated	$2.8 \cdot 10^7$	$2.9 \cdot 10^7$	$3.0 \cdot 10^7$
$N_{photons} \geq 10$	4151150	4299453	4447521
Triggered	421813	559537	2095429
Reconstructed	228097	221007	212332
$\cos(\theta) > 0$	11718	13374	16743
Livetime	79735.9 s (0.923 day)	82594.7 s (0.956 day)	85439.2 s (0.989 day)

Table 5.3: *Sample of simulated atmospheric muon events used in this study.*

occur at large angles. This is important when considering the background of atmospheric muons. Consequently, the simulated rate of triggered events due to atmospheric background differs significantly between these parameterisations. One of these parameterisations has been used in the earlier Antares simulation software. This parameterisation was based on measurements of a different optical module design. The more recent parameterisations, which show an increased acceptance at large angles of incidence, were used in the study of the data from Line 1 in chapter 4. In this chapter, the parameterisation from [40] is used. This parameterisation corresponds to our current best knowledge. At 60 kHz background rate, the trigger rate due to atmospheric muons is a factor 2 higher than the rate using the older parameterisation. Previous analyses, for example in reference [74], were done with the old parameterisation and thus predict a lower event rate. The use of a different angular acceptance also has an effect on the rate of events due to upward going (atmospheric) neutrinos. The increase in rate is smaller than that of the atmospheric muons, as the difference between the parameterisations at small angles of incidence is limited to a few percent. Figure 5.1 shows the relative increase in reconstruction rate with the angular acceptance used in this study as function of neutrino energy. It can be seen that the increase is largest at lower energies and decreases towards higher energies. The total increase in rate from atmospheric muons is about 24 %, while for a signal flux proportional to E^{-2} it is 13 %.

5.2 Selections

After track reconstruction, several quantities are available which contain information on the quality and properties of the track. These quantities can be used as selection criteria to suppress the background. Events are selected by requiring a minimum or maximum value for a certain quantity related to the event. This is referred to as applying a cut. The first cut corresponds to the requirement that the event is reconstructed as upward going, thus $\cos(\theta) \geq 0$. In the following several other cuts will be presented.

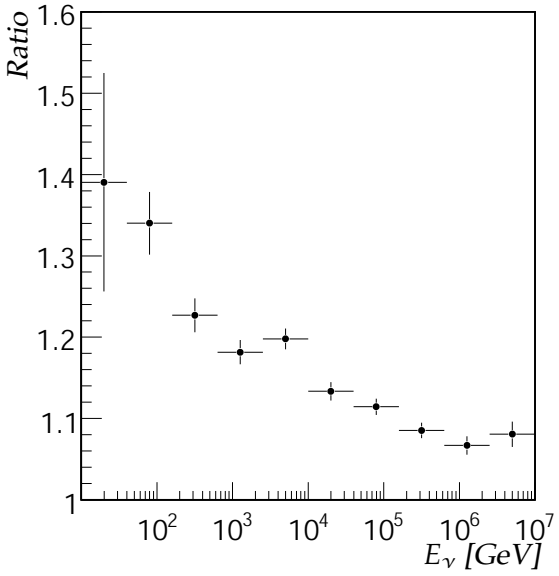

Figure 5.1: *Ratio of the rates of reconstructed neutrinos for different parameterisations of the angular acceptance of the optical modules. The ratio is plotted as function of neutrino energy and given by the rate for the parameterisation given in [40] over the rate for the 'old' (see section 2.6.1) parameterisation. The neutrinos are isotropically generated in upward directions.*

5.2.1 Track length

In section 3.6.7 the track length ($\Delta z'$) was introduced. This quantity is the largest distance between two hits measured along the reconstructed muon track. For this, the hits for the prefit with the smallest angular residual compared to the final likelihood fit are used. Only hits that are included in the selection based on the directional clustering criterion (see section 3.3) are considered. The value $\Delta z'$ can be used as a measure of the accuracy of the muon track reconstruction (see section 3.6.7 and figure 3.29). The distributions of $\Delta z'$ for atmospheric muons, neutrinos and random background events which are reconstructed as upward going are shown in figure 5.2. It can be seen from figure 5.2 that the distribution for atmospheric muons shows an excess of events at small track lengths compared to atmospheric neutrinos and random background events. A prominent feature of the $\Delta z'$ distribution for atmospheric muons is the triple peaked structure. These peaks can clearly be distinguished in figure 5.2 at around 70, 130 and 190 meters. The typical distances between two detector lines vary from about 60 to 70 meters (see figure 2.8). The three peaks correspond to hits on 2, 3 and 4 lines respectively. In the context of the analysis of the data of a single line, it was shown that electro-magnetic showers along a muon track can bias the reconstruction to horizontal directions (see section 4.5). This affects in particular the atmospheric muons due to the orientation of the optical modules. Two peaks can be seen in the distribution of atmospheric neutrinos. These peaks are shifted to higher values of $\Delta z'$ compared to the 3 and 4 line peaks of the atmospheric muons. The shifts are due to the angular distribution of the atmospheric neutrinos, which covers the complete upward going solid angle. The peak at $\Delta z' \simeq 200$ m which can also be seen in the distribution of random background events, corresponds to the typical

	60 kHz	120 kHz	240 kHz
Atmospheric ν	84.4 %	89.4 %	86.8 %
Atmospheric μ	49.9 %	59.7 %	56.8 %
Random background	–	94.0 %	90.5 %

Table 5.4: *Fractions of remaining events after requiring a minimum length of the reconstructed track ($\Delta z^{'}$) of 120 meters for different random background rates.*

length scale of the detector for an isotropic muon flux and a random background.

In order to reject a fraction of the background of wrongly reconstructed atmospheric muons, a cut on $\Delta z^{'}$ is applied. Only upward reconstructed tracks with $\Delta z^{'} > 120$ m are accepted. The remaining fractions of atmospheric muons, atmospheric neutrinos and random background events are given in table 5.4. As can be seen from table 5.4, the cut on $\Delta z^{'}$ is most effective on wrongly reconstructed atmospheric muons. Events due to random background are least affected.

5.2.2 Up/Down likelihood

The muon track reconstruction algorithm scans over 4π solid angle and produces in general a set of different track candidates. In section 3.6.5, the use of the relative values of the log-likelihood per degree of freedom was introduced as a way to select the best track candidate. The track candidate with the largest log-likelihood per degree of freedom is selected. As shown in chapter 3, it is possible that a solution which differs from the true track, has a higher log-likelihood per degree of freedom than the true track. This can happen when the processes that have led to the recorded hits are different from the assumed (muon) hypothesis or due to statistical fluctuations. It is possible to consider the best upward and the best downward reconstructed track separately. For this purpose, the largest value of the likelihood per degree of freedom given by L^{up}/N^{up}_{dof} and L^{down}/N^{down}_{dof} can be used, where the superscript up and down refer to the upward and downward directions. The difference of these values

$$\Delta L = L^{up}/N^{up}_{dof} - L^{down}/N^{down}_{dof} \tag{5.1}$$

can be used to reject background events which are wrongly reconstructed as upward going. In figure 5.3, the fraction of remaining events for a given minimum value of ΔL is shown for neutrinos, atmospheric muons and random background events. The plateau in figure 5.3 at large values of ΔL is due to events which have no downward going solution. Several features can be seen in figure 5.3 when comparing atmospheric muons, neutrinos and background events and considering different background rates. First, a larger fraction of the neutrinos has no downward solution at all compared to atmospheric muons. Whereas, almost 80

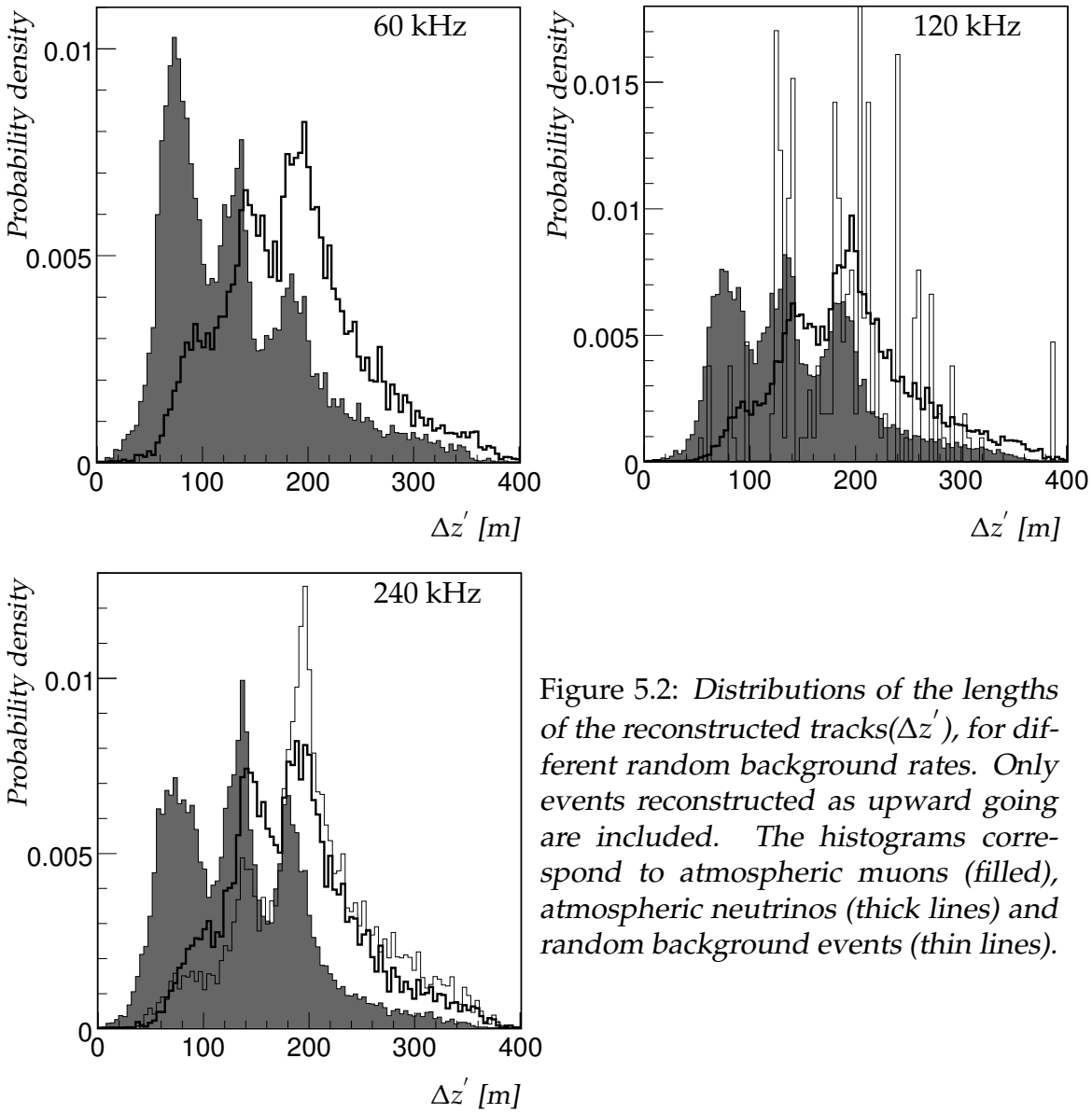

Figure 5.2: *Distributions of the lengths of the reconstructed tracks($\Delta z'$), for different random background rates. Only events reconstructed as upward going are included. The histograms correspond to atmospheric muons (filled), atmospheric neutrinos (thick lines) and random background events (thin lines).*

	60 kHz	120 kHz	240 kHz
Value of cut on ΔL	1.0	0.5	0.3
Remaining atmospheric ν	86.7 %	86.7 %	87.1 %
Remaining atmospheric μ	22.1 %	27.2 %	42.1 %
Remaining random background	– %	93.6 %	89.7 %

Table 5.5: *Values of the cut on ΔL (see text) for different background rates. The numbers correspond to the remaining fractions of events.*

% of the atmospheric muons have a possible downward going solution at 60 kHz, this fraction is 35 % for atmospheric neutrinos. The neutrinos which do have a downward solution have in general a larger value of ΔL compared to the atmospheric muons. This is reflected by the gradient of the distributions at small values of ΔL. The fraction of remaining events drops more steeply for atmospheric muons, than for neutrinos. Thus, a selection on a minimum value of ΔL can reduce the number of upward reconstructed atmospheric muons, whilst retaining a large fraction of the neutrinos. At high rates (120 and 240 kHz) few random background events ($<$ 10%) have a downward solution. Hence, these events show a plateau close to unity. With increasing random background rate, the relative contribution of direct hits from the atmospheric muons is suppressed. At the highest rates, the dead-time of the ARSs comes into play. As a result, the number of atmospheric muon events that are falsely identified as upward going increases. The suppression of muon hits also leads to a lower chance of having a (correct) downward going solution in the set of solutions. This is reflected in the increase of the level of the plateaus at large ΔL for atmospheric muons in figure 5.3 with increasing rate. The effect of increasing background rates is different for the neutrinos, depending on their energy. Increasing the rate from 60 to 120 kHz causes more events to have also a downward going solution. This is due to availability of additional hits. When increasing the rate further to 240 kHz, the contribution of muon hits gets suppressed due to ARS dead-time and random background hits can form a significant fraction of the hits in the events, especially at lower energies. This can even lead to the impossibility of finding enough L1 hits for a given direction in the prefit, and thus rejecting it. The effect on the hit selection can be seen in figure 3.9. So, while the fraction of events with a downward solution increases when increasing the rate from 60 kHz to 120 kHz, it decreases when increasing the rate further to 240 kHz. The crossing of the lines for atmospheric and 'signal' neutrinos in figure 5.3 for 240 kHz reflects that this effect is stronger at lower energies. For each rate, a minimum value for ΔL is determined in such way that the ratio between the fraction of atmospheric neutrinos and the fraction of atmospheric muons is maximal. In table 5.5, the values thus obtained are given, together with the remaining fractions of events.

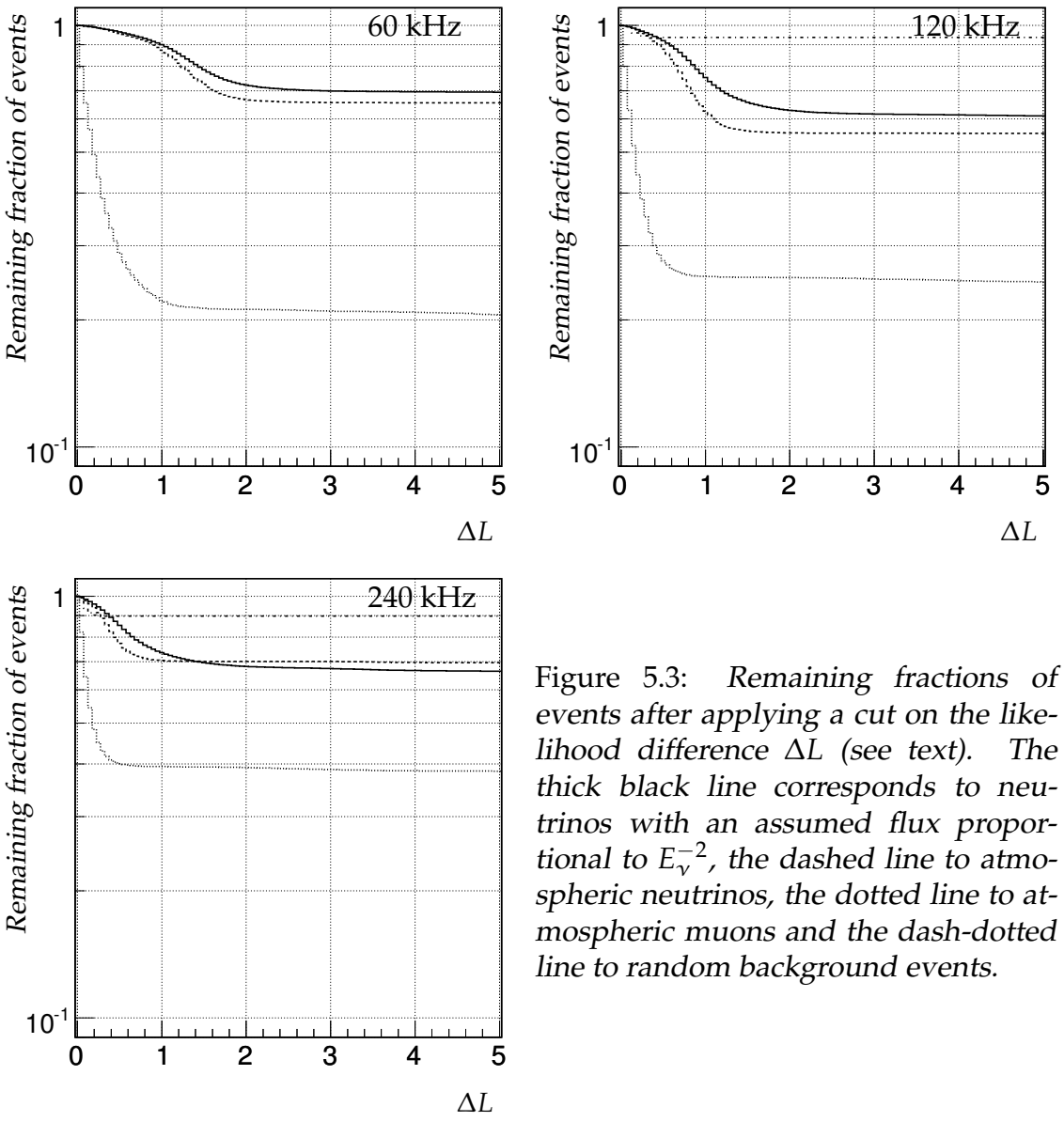

Figure 5.3: *Remaining fractions of events after applying a cut on the likelihood difference ΔL (see text). The thick black line corresponds to neutrinos with an assumed flux proportional to E_ν^{-2}, the dashed line to atmospheric neutrinos, the dotted line to atmospheric muons and the dash-dotted line to random background events.*

5.2.3 Likelihood and number of compatible solutions

The log-likelihood per degree of freedom can be combined with the number of compatible solutions (see section 3.6.8) to obtain a joint quantity, namely :

$$\Lambda = \ln(L)/N_{dof} + 0.1(N_{comp} - 1) \tag{5.2}$$

It was shown in reference [74] that cutting on a minimum value of Λ is very effective in reducing the background of atmospheric muons. The effect of a cut on the value of Λ, including the cuts discussed in the previous two sections, is shown in figure 5.4. In this figure, the remaining number of upward reconstructed events per day due to atmospheric muons, atmospheric neutrinos and random background events is shown as a function of Λ. The efficiencies for a neutrino flux proportional to E^{-2} are also shown. As can be seen from figure 5.4, the background due to atmospheric muons and random noise can be reduced significantly, whilst retaining the neutrino signal(s). For small values of Λ, the wrongly reconstructed atmospheric muons dominate. The contribution from atmospheric neutrinos starts to dominate at $\Lambda \simeq -6$. As was shown in section 3.6.4, an increase of the random background rate, shifts the log-likelihood per degree of freedom to smaller values. The value of N_{comp} also decreases with increasing rate, as shown in section 3.6.8. These two effects result in a shift of Λ to smaller values as can be seen in figure 5.4 for all types of events. The contribution of random background events also increases with increasing background rates, but remains smaller by at least a factor 10 than the contribution from atmospheric muons. As was shown in chapter 3, the angular resolution of reconstructed tracks is correlated with the likelihood per degree of freedom and the number of compatible solutions. The effect of the cut on Λ on the angular resolution is shown in figure 5.5. In this graph, the angular resolution for an atmospheric neutrino spectrum and a neutrino energy spectrum proportional to E^{-2} is shown for different random background rates. Several observations can be made when comparing the different neutrino spectra and considering the different random background rates. The values without a cut on Λ reflect the deterioration of the angular resolution with increasing random background rates (see also figure 3.26). The differences between the results for the two neutrino fluxes, reflect the dependence of the angular resolution on the muon energy (see also figure 3.26). The E^{-2} spectrum is harder than that of the atmospheric neutrinos. As the angular resolution improves with energy, the overall resolution for a E^{-2} spectrum is better. At larger values of the cut on Λ, the relative improvement of the angular resolution depends on the background rates. In short, the improvement of the angular resolution is larger for higher random background rates. Increasing Λ has a more severe effect on the angular resolution of the remaining events at higher background rates. This can be seen in figure 5.5 by the different gradients of the lines. This has to be considered together with the decreasing efficiency as shown in figure 5.4. For each background rate, the value of the cut on Λ is

Rate	cut value on Λ	Atmospheric neutrinos	Signal efficiency
60 kHz	-5.3	9.7/day	66.8 %
120 kHz	-5.5	6.2/day	61.6 %
240 kHz	-5.9	4.9/day	55.9 %

Table 5.6: *Values of the cut on Λ for different random background rates and the corresponding rates of atmospheric neutrinos and efficiencies for a neutrino signal with a flux proportional to E_ν^{-2}.*

chosen such that the remaining events due to atmospheric muons is 1 per day. The background is then dominated by atmospheric neutrinos. In order to reduce the uncertainty on the value of the cut due to the limited statistics, the value is determined from an exponential fit to the distributions. This fit is applied to the differential distributions of the data. The lower bound is chosen such that the uncertainty of the slope from the fit is less than 10 %. The values for the cut on Λ which result from these fits are shown in table 5.6, together with the fractions of remaining events.

5.3 Effective area

The detector efficiency is usually expressed as the neutrino effective area. The neutrino effective area A_ν^{eff} is defined as the ratio of the rate of reconstructed events and the incident neutrino flux :

$$A_\nu^{eff}(E_\nu, \theta, \phi) = \frac{R_{det}(E_\nu, \theta, \phi)}{\Phi_\nu(E_\nu, \theta, \phi)} \tag{5.3}$$

In this equation, R_{det} is the rate of reconstructed events and Φ_ν the neutrino flux arriving at the surface of the Earth. The effective area includes the neutrino cross section, the propagation of neutrinos through the Earth and the detection of the muons. The detection rate is determined by reconstruction and selection criteria defined previously. Thus, the neutrino effective area incorporates the reconstruction efficiency and the inefficiencies introduced by the selection cuts to reduce background. Using this definition, the rate of observed neutrino events can directly be determined for any given neutrino flux. The neutrino effective area depends on the neutrino energy and direction. In figure 5.6, the neutrino effective area is shown for upward directions and different ranges in zenith angle. The strong dependence of the neutrino effective area on the neutrino energy comes mainly from the energy dependence of the cross section (see figure 2.1) and the increase of the range of the muon. The reduction of the neutrino effective area for upward directions at very high energies is caused by the absorption of neutrinos

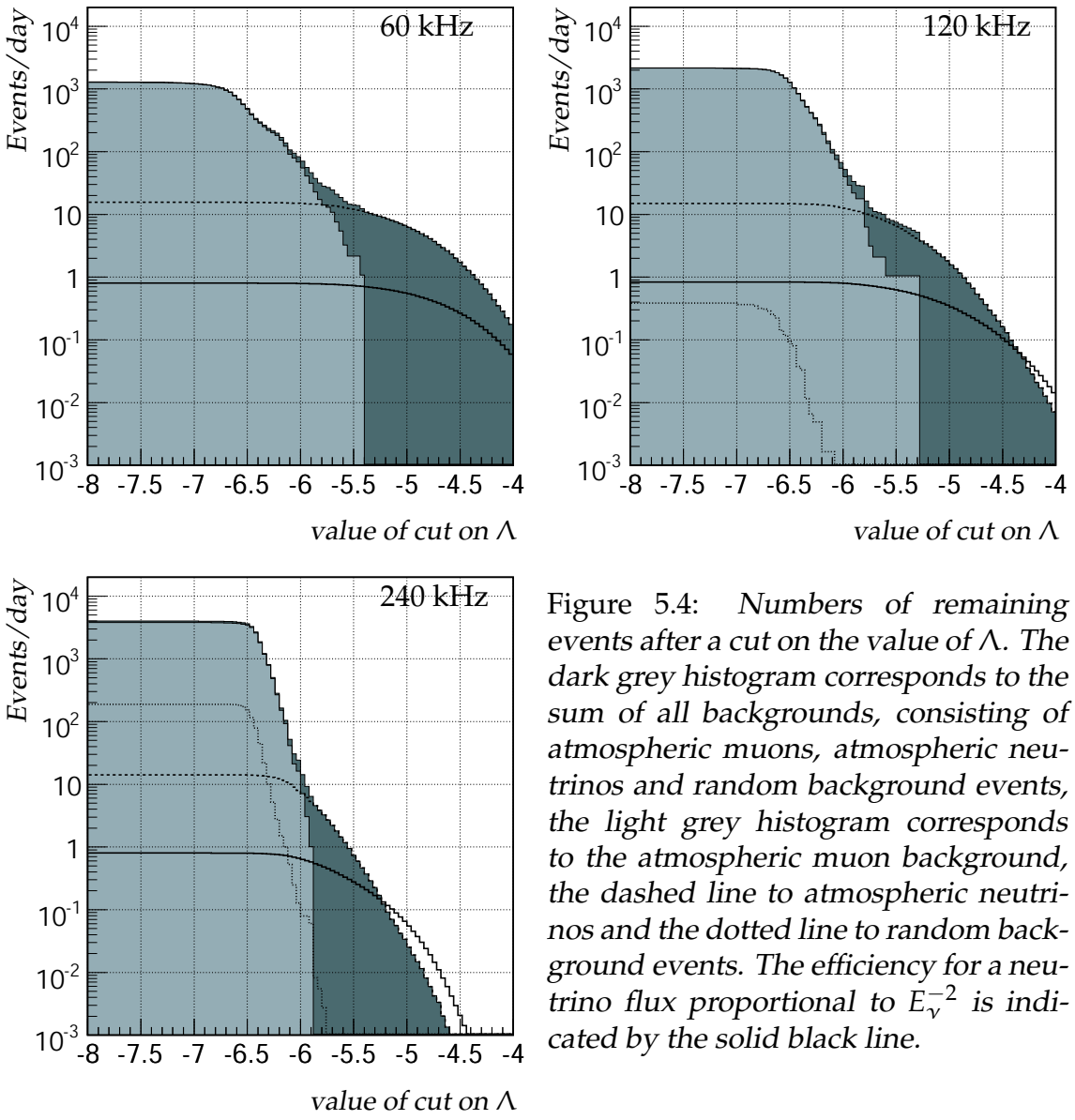

Figure 5.4: *Numbers of remaining events after a cut on the value of Λ. The dark grey histogram corresponds to the sum of all backgrounds, consisting of atmospheric muons, atmospheric neutrinos and random background events, the light grey histogram corresponds to the atmospheric muon background, the dashed line to atmospheric neutrinos and the dotted line to random background events. The efficiency for a neutrino flux proportional to E_ν^{-2} is indicated by the solid black line.*

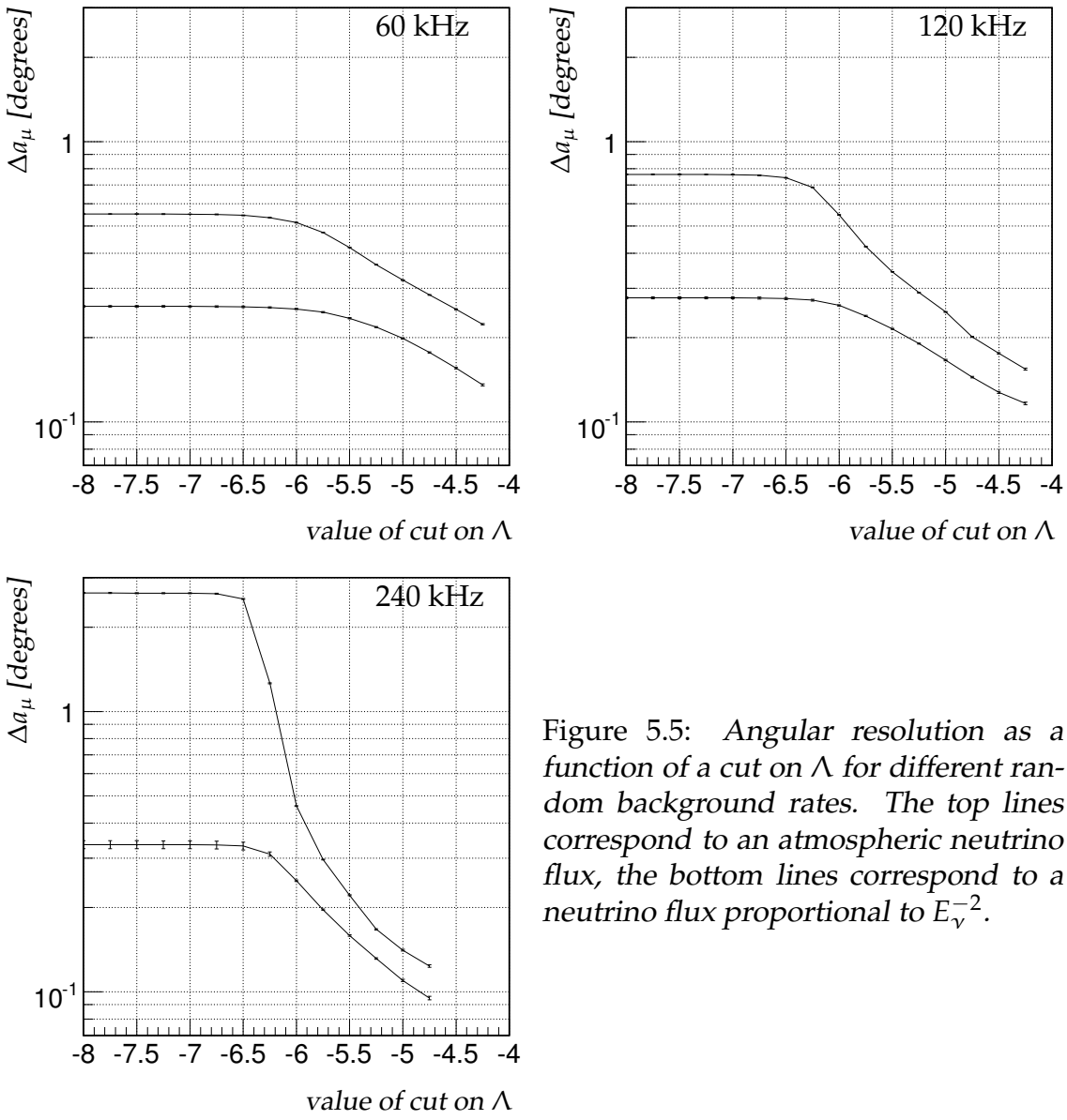

Figure 5.5: *Angular resolution as a function of a cut on Λ for different random background rates. The top lines correspond to an atmospheric neutrino flux, the bottom lines correspond to a neutrino flux proportional to E_ν^{-2}.*

in the Earth. In general, the neutrino effective area reduces with increasing random background rates. This effect is more prominent at lower energies. In figure 5.7, the ratios of the neutrino effective areas are shown as function of the energy integrated over all upward directions. The random background rate mostly affects the neutrino effective area at lower neutrino energies. Compared to the effective area at 60 kHz, the effective areas for 120 and 240 kHz differ up to a factor 2 between about 100 and 300 GeV. With increasing neutrino energy, the effective areas differ less. Compared to 60 kHz, the loss in effective area at 10^7 GeV is less than 5 % at 120 kHz and less than 10 % at 240 kHz.

5.4 Angular resolution

The median of the angular residual distributions is used to quantify the angular resolution of the detector. The resolution for the muon direction is presented in chapter 3. In this chapter, several cuts were introduced which are used to reduce the background. These cuts affect the efficiency of the detector as well as the angular resolution. The angular resolution for muons is shown as a function of the variable Λ in figure 5.5. The relevant quantity for the pointing accuracy of the telescope is the angular residual for neutrinos. The accuracy of the determination of the neutrino direction depends on the energy in two ways. The actual reconstruction is done on the muon, and the angular resolution of the reconstruction depends on the muon energy. In general, the angular resolution of the reconstruction improves with increasing energy due to the increase of the detectable photon yield. The neutrino direction is obtained by assuming the same direction as that of the muon. This introduces an additional error, as the muon and neutrino directions are related through the finite scattering angle. The average scattering angle decreases with the neutrino energy (see section 2.2). The resolutions for the muon and neutrino direction are studied after applying the cuts which were introduced earlier in this chapter. In figure 5.8, the angular resolution for muon and neutrino directions are shown as function of neutrino energy for different random background rates. As can be seen from figure 5.8, the resolution improves with energy. The angular resolution does not depend significantly on the random background rate. It can be seen from figure 5.8 that for neutrino energies in excess of 100 TeV the angular resolution for neutrinos is limited by the accuracy of the reconstruction.

5.5 Comparison

The detector performance using the muon track reconstruction and cuts developed in this work, can be compared to the performance when using the standard reconstruction [74]. The standard reconstruction was developed and evaluated

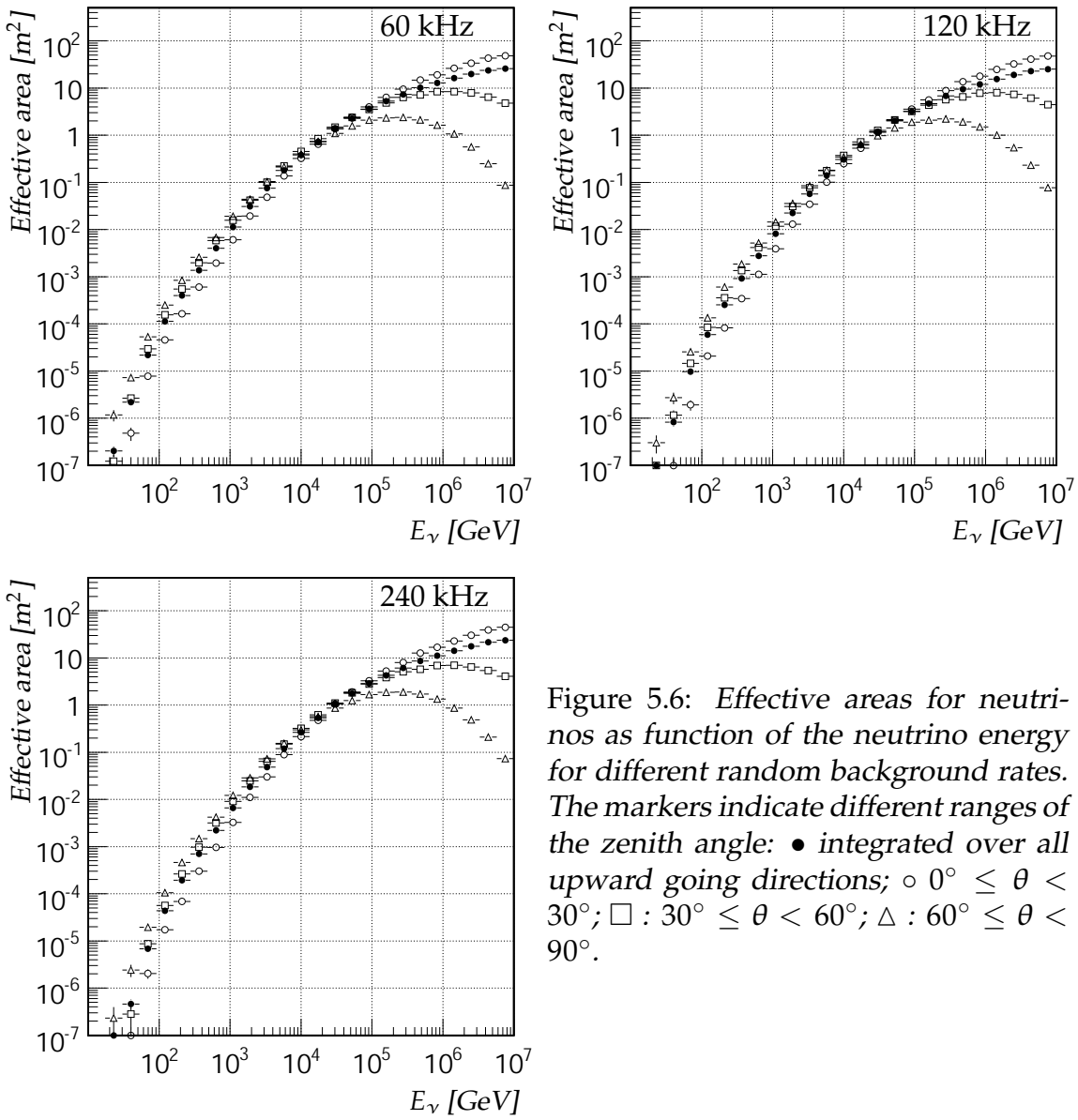

Figure 5.6: *Effective areas for neutrinos as function of the neutrino energy for different random background rates. The markers indicate different ranges of the zenith angle:* • *integrated over all upward going directions;* ∘ $0^\circ \leq \theta < 30^\circ$; □ : $30^\circ \leq \theta < 60^\circ$; △ : $60^\circ \leq \theta < 90^\circ$.

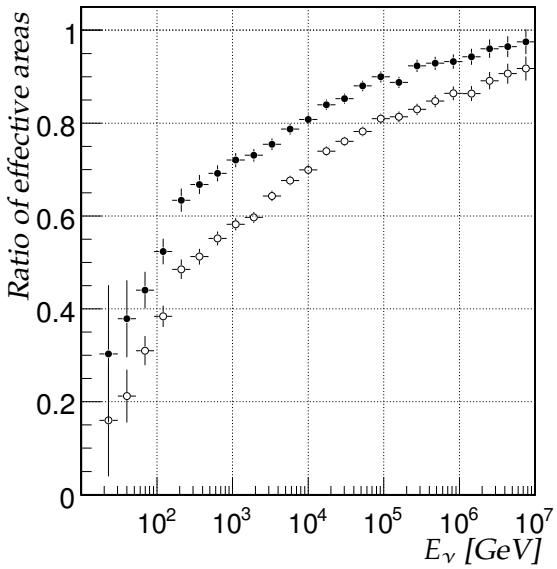

Figure 5.7: *Ratios of effective areas for different background rates as function neutrino energy. The filled dots indicate the ratio of the effective area at 120 kHz over the effective area at 60 kHz. The open dots indicate the ratio of the effective area at 240 kHz over the effective area at 60 kHz.*

under different conditions. These conditions were the absence of the current trigger algorithm and the use of an old parameterisation of the angular acceptance of the optical modules. As shown previously, the use of the current parameterisation leads to an increase in detected photons and event rates compared to the old parameterisation. The comparison is done at a random background rate of 60 kHz. In the standard reconstruction, the final cut to reduce background is similar to the one presented in this work. It is based on the quantity defined in equation 5.2. However, the PDF used in the final stage of the standard reconstruction differs from the one developed in this work. The cut value used in the standard reconstruction is referred to as Λ_s. The value for the cut on Λ_s which reduces the rate of atmospheric muons (neutrinos) to about 1/day (10/day) was previously [74] determined to be -5.3. This cut is re-evaluated, to take into account the new angular acceptance. In figure 5.9, the remaining number of atmospheric muons and neutrinos is shown as function of the value of the cut on Λ_s. Also shown is the efficiency for a signal proportional to E_ν^{-2}. From this figure, it can be seen that when a cut $\Lambda_s > -5.3$ is applied, the remaining rates of atmospheric muons and neutrinos are both about 10/day. In order to reduce the background of atmospheric muons to about 1/day using AartStrategy, the minimal value of Λ_s is set to -5. The rate of atmospheric neutrinos is then about 8/day. With this newly determined cut on the value of Λ_s, the effective area and angular resolution are compared with those presented in this work. In figure 5.10 both effective areas are shown. It can be seen that the effective area is increased at energies below about 4 TeV and above about 50 TeV. At 10 PeV, the increase in effective area reaches about a factor 2. This increase can be attributed to the better description of the PDF at these high energies (see section 3.5). At 100 GeV, the increase is about 40 %. The angular resolutions as function of neutrino energy are compared in figure 5.11. The angular resolutions are almost identical, with the standard

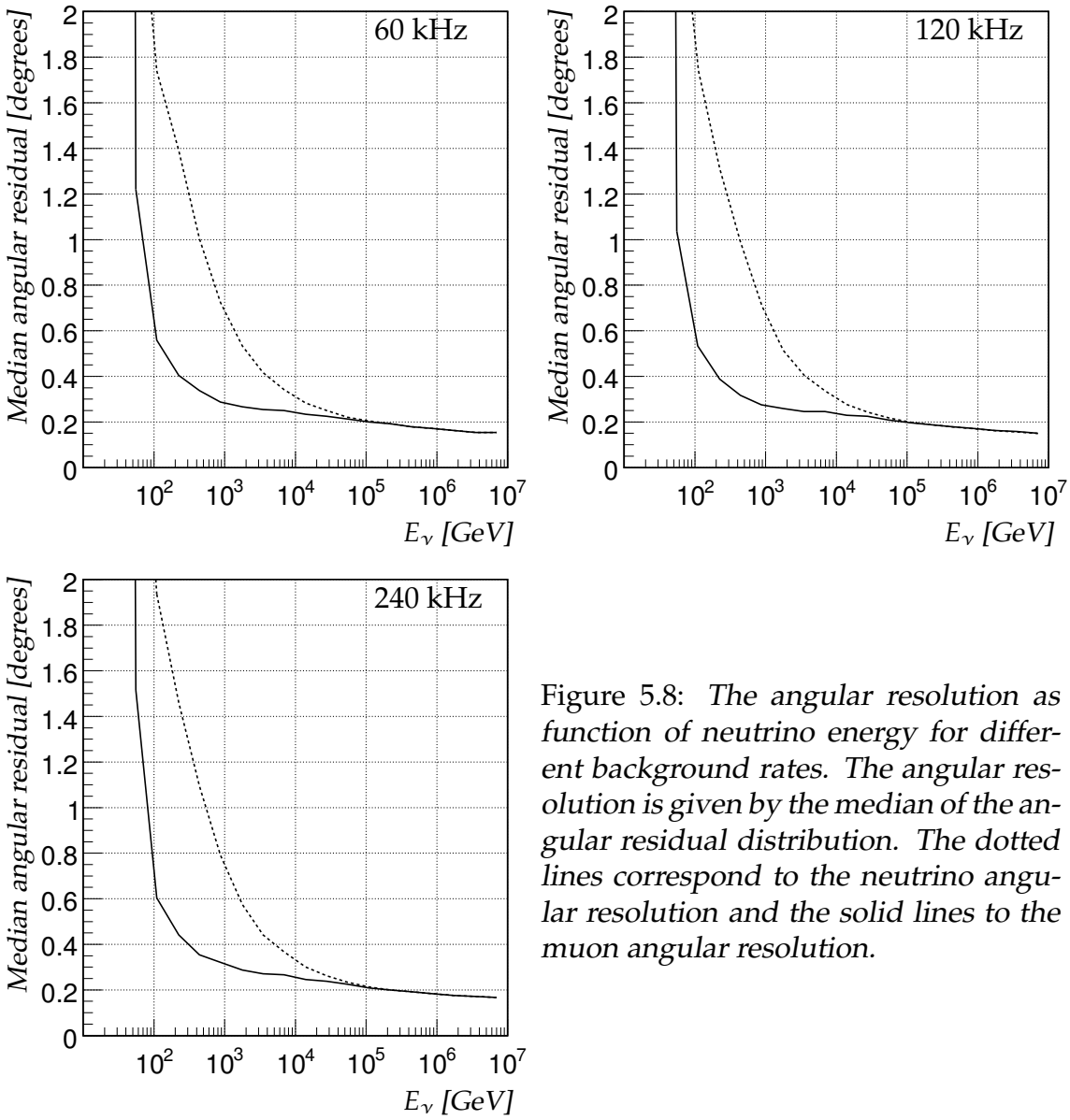

Figure 5.8: *The angular resolution as function of neutrino energy for different background rates. The angular resolution is given by the median of the angular residual distribution. The dotted lines correspond to the neutrino angular resolution and the solid lines to the muon angular resolution.*

reconstruction having a small advantage at lower energies and the new one at higher energies. When considering a neutrino flux proportional to E^{-2}, the median angular residual is about 0.26° for both the old and new methods.

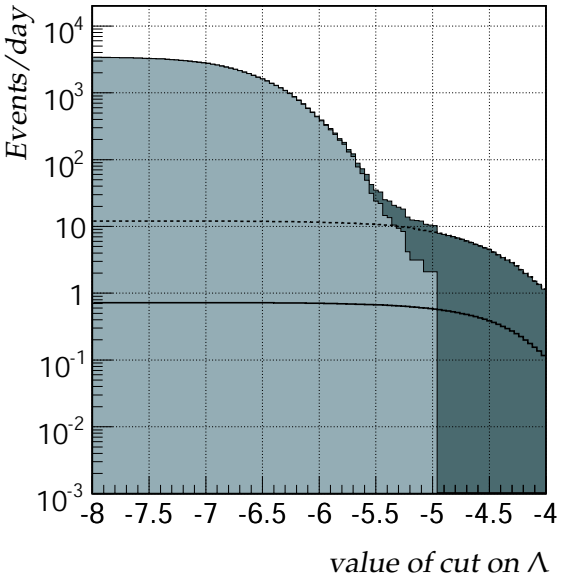

Figure 5.9: *Numbers of remaining events after a cut on the value of Λ, using the muon track reconstruction algorithm from [74]. The random background rate is 60 kHz. The dark grey histogram corresponds to the sum of all backgrounds, consisting of atmospheric muons, atmospheric neutrinos and random background events, the light grey histogram corresponds to the atmospheric muon background, the dashed line to atmospheric neutrinos and the dotted line to random background events. The efficiency for a neutrino flux proportional to E_ν^{-2} is indicated by the solid black line.*

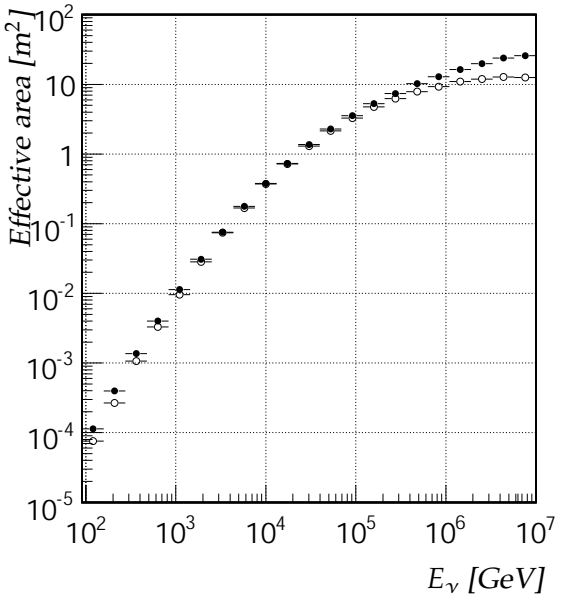

Figure 5.10: *Comparison of effective areas for neutrinos as function of the neutrino energy at a background rate of 60 kHz. The effective areas are integrated over all upward going directions. • : this work; ○ : using the muon track reconstruction algorithm and cuts from [74]*

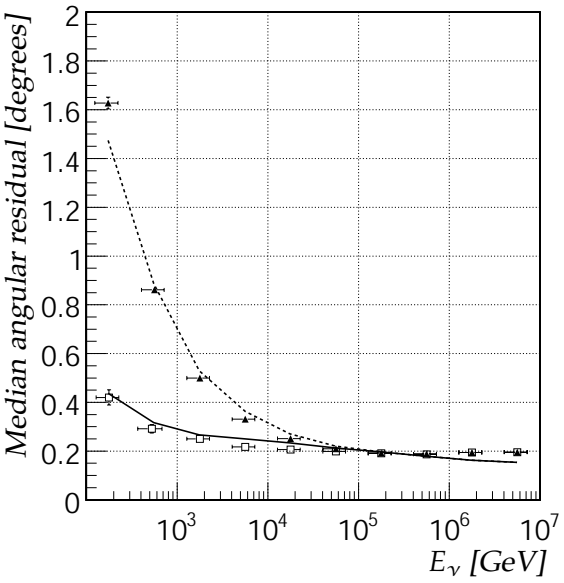

Figure 5.11: *The angular resolution as function of neutrino energy at a background rate of 60 kHz. The angular resolution is given by the median of the angular residual distribution. The lines correspond to the muon track algorithm developed in this work, the points to the algorithm and cuts from reference [74]. The dotted line and filled triangles correspond to the neutrino angular resolution and the solid line and open squares to the muon angular resolution.*

5.6 Conclusion

In this chapter the reconstruction method developed in this work was evaluated in the presence of backgrounds. The trigger algorithm and the new parameterisation of the angular acceptance have been taken into account. Several cuts have been presented that reduce the backgrounds from atmospheric muons and random background rate. The detector performance has been evaluated with these cuts applied. The resulting effective area and angular resolution have been presented. The effective area of the Antares detector depends on the random background rate. When the level of random background increases, the effective area is reduced. The reduction in effective area is stronger at lower neutrino energies. The angular resolution remains at the same level as the standard reconstruction, evaluated at 60 kHz random background rate. The effective area improves upon the previous effective area. Below 4 TeV and above 50 TeV neutrino energy, the effective area is increased up to a factor 2 at 10 PeV neutrino energy.

Chapter 6

Summary and conclusion

Earth's atmosphere is continuously being bombarded by energetic particles. Much is unknown about these cosmic rays. There are many uncertainties about the exact elemental composition and the origin of these high-energy particles. A well established experimental fact is the large range of energies measured. The highest energy cosmic rays which are measured have energies exceeding 10^{19} eV. As the cosmic rays are charged, they are deviated from their paths and thus cannot be used to trace their sources, except at the highest energies. Photons, the traditional probes for astronomy, have limited range at high energies due to interactions with background photons. Interactions of high-energy protons can lead to the production of neutrinos. This could also happen at the sites where the cosmic rays attain their energies. The Antares collaboration is building a telescope that can detect neutrinos. These particles, leptons, are neutral and only interact through the weak force with an extremely small cross section. Because of these properties, a neutrino is not deflected by galactic and extra-galactic magnetic fields and not easily absorbed by matter that makes up the universe. In short, neutrinos are a good probe for astrophysical research because they point straight to their source and can travel larger distances than high energy photons, as they are not easily absorbed or scattered. Measurements of neutrinos with an extra-terrestrial origin could shed light on the production processes of cosmic rays. The Antares neutrino telescope detects neutrinos by measuring the luminous products of neutrino interactions in sea-water or the Earth below it. In this thesis, the main focus is on muon-neutrinos. The interaction of a muon-neutrino can result in a muon. At sufficiently high energies, muons can travel large distances in rock or water and retain the information on the neutrino direction. When the velocity of a muon exceeds the speed of light in water, it emits Cherenkov light along its path. The use of sea-water as the detection medium caters for the need of a large detection volume which is required due to the small interaction cross section of neutrinos. Due to the transparency of sea-water, Cherenkov light can travel significant distances before being absorbed. The Antares neutrino telescope implements an array of light-sensitive photo-multiplier tubes to detect this light. The

photo-multiplier tubes are encased in pressure-resistant glass spheres, called optical modules. A triplet of optical modules makes up a storey, of which there are 25 along a vertical line. By attaching buoyant elements to the top of the line, they are kept upright. A total of 12 lines makes up the Antares detector, thus 900 optical modules. The lines are installed at about 2.5 km depth in the Mediterranean Sea. Each line has an active length of about 350 meters and the footprint of the detector on the seabed measures approximately 180×180 m^2. The signals from the photo-multiplier tubes are digitized and sent to shore through a 40 km long electro-optical cable. The data consists of the arrival times of photons on the photo-multiplier tubes together with the number of photo-electrons that were recorded, these are referred to as hits. On shore, a farm of commodity PC's filters the data by making use of causal relations between hits that originate from muons, this process is called triggering. From the filtered data, the parameters of the muon track that caused the photons can be estimated. This process is called muon track reconstruction, and is essential for neutrino astronomy, as it allows the association of a point in the sky to the potential muon. Unfortunately, astrophysical neutrinos are not the only source of light at the location of the detector. In the interactions of cosmic rays with the atmosphere, muons are produced. Despite the column of more than 2 km of water, some muons reach the detector and generate a detectable signal. A way of reducing this background is by only considering muons that travel upwards through the detector, as no muon makes it through the Earth. Signals from neutrinos generated in the interactions of cosmic rays cannot be distinguished from astrophysical neutrinos at the event level. Another form of background manifests itself as a continuous rate of detected photons by the photo-multiplier tubes. The two major causes of this are the decay of ^{40}K present in the sea-water and biological activity, called bioluminescence. The counting rate is characterized by a continuous component and a bursting component. The continuous component varies between 50 kHz and several hundred kHz, while the bursts can last from milliseconds to minutes. This continuous background can result in the false identification of a muon.

This thesis covers two subjects. The first is the development of a muon track reconstruction algorithm. The performance of the reconstruction algorithm is studied as is the resulting performance of the Antares detector under realistic conditions. This is done using simulations. This thesis further contains an analysis of the first data taken with the Antares neutrino telescope. For this analysis, the track reconstruction is essential.

Muon track reconstruction, besides being a non-linear problem, which makes it necessary to use iterative algorithms, is complicated by several factors. First are the stochastic processes via which a muon can lose its energy. Electro-magnetic showers occurring along the track cause detectable photons. Due to their stochastic nature, the number of showers, their positions along the track and energies are unknown, complicating the muon track reconstruction. Secondly, in order to achieve optimal angular resolution, the properties of the sea-water and the de-

tector should be known in detail. These include for example the scattering and absorption lengths of the sea-water. The algorithm described in this thesis is designed to have a minimal dependence on the model describing all the processes leading to recorded photons. The main assumption is that of a charged particle traveling at relativistic speed which emits Cherenkov light along its path through sea-water. By aiming to maximize the purity of the measured photons with respect to the assumed hypothesis, extensive modeling is avoided. This makes the algorithm particularly suitable for use during the initial phase of detector operation. A common problem with parameter estimation algorithms is that of local solutions. By implementing a scan over the solid angle, a maximum number of possible solutions is charted, from which an optimal is chosen. The scan over solid angle additionally allows for a hit selection procedure which makes use of pair-wise causal relations between hits caused by a muon. In the final stage of the fit, the χ^2 based on the differences between the estimated and measured photon arrival times (hits) is minimized. Due to the scanning, several track candidates are found for a given event. Depending on the subsequent analysis, either one or several track candidates can be chosen. In this work, the track with the largest number of hits, and, if necessary, the smallest χ^2 is used.

In order to study the full potential of the Antares neutrino detector, a maximum likelihood is added to the algorithm. For this procedure, a probability density function (PDF), describing the probability of photon arrival times is used. This PDF is derived from simulations. An existing PDF is modified to reduce the influence of correlations between hits. The new PDF shows a better behavior as a function of energy. Even when the likelihood fit with the full PDF is started at the true values of the muon track parameters, it can converge to estimates of the track parameters which differ significantly from the true ones. Among the causes for this are statistical fluctuations and electro-magnetic showers occurring along a muon track.

Operation of the Antares neutrino telescope began on the 2^{nd} of March 2006. On that date the first detector line was connected. The muon track reconstruction algorithm described in this work was used to reconstruct the first muons. On the 21^{st} of September, a second line was connected. In this work, an analysis of the data that was collected with the single line is described. The use of a single line introduces some limitations in reconstruction and analysis with respect to using multiple lines. As a single vertical line has a rotational symmetry, the azimuthal angle of the muons can not be determined. Also, when only part of the Cherenkov wave-front is sampled, the track fit problem allows for two equally likely solutions. These solutions differ in zenith angle by two times the Cherenkov angle and are called 'ghost'-solutions.

In order to ensure a good quality sample, a selection is made from the total available data. The main selection criteria are a random background rate below 120 kHz, and no more than 15 % bursts from bioluminescence. The total sample corresponds to 9.3 days, in which 75621 events were triggered, corresponding

to an average trigger rate of 0.094 Hz. The rate of events due to pure random background is estimated to be less than 0.01 Hz. No use is made of the dynamic alignment of the detector, as it was not consistently available yet. The analysis includes simulations of atmospheric muons, atmospheric neutrinos and random background.

The negative effect of electro-magnetic showers along muon tracks on the angular resolution is especially apparent when considering atmospheric muons. The downward orientation of the optical modules favors the detection of photons traveling in upward directions. In case of atmospheric muons, the direct Cherenkov light travels in downward directions, while the light from electro-magnetic showers can reach the optical modules in upward directions. So, there is a bias to detect photons from electro-magnetic showers on atmospheric muon tracks. Also, when considering a single line, the signal from an electro-magnetic shower can mimic the signal from a muon traveling in a (near) vertical direction. A way of dealing with electro-magnetic shower events is to require a minimum number of hits which are used to reconstruct a track. As the track reconstruction algorithm takes no more than one hit per floor, this requirement is translated in a length along the detector line. Due to the size of electro-magnetic showers, which is of the order of a few meters, compared to the muon track, these events are suppressed. While requiring a minimum χ^2 probability generally improves the angular resolution for neutrino events, it is less effective for atmospheric muon events. A robust method of improving the angular resolution, is requiring a minimum number of hits (thus floors) used in the track reconstruction.

The geometry of the detector allows it to be split up in almost identical sub-detectors. This is done in the analysis of the data from Line 1. By splitting the detector an estimate of the resolution on the zenith angle can be made using only data. The resolution found in this way can be better than 1°, which corresponds to about 0.5° for the complete line.

An important quantity in describing the detector response is the angular acceptance of the optical modules. The angular acceptance is the relative sensitivity of the optical module to photons arriving at different angles. In this work, three models of the angular acceptance are considered. Two of those are most relevant, as they are based on measurements on and simulations of the current optical module design. The third is based on measurements of an older optical module design. The main differences between the parameterisations of the angular acceptance lies in the backward region. This leads to different predictions in the rates of detected events for different parameterisations. The largest differences in rate are found for atmospheric muons. Due to the downward facing orientation of the optical modules and the downward going direction of the muons, most photons arrive at the optical modules from backward directions. When confronting the data from Line 1 with the simulation, the measured rates of reconstructed events lie within the uncertainties due to the angular acceptance.

A study of the residuals of the hit times shows a good agreement between

simulation of atmospheric muons and data. Thus, the simulation of the processes influencing the measured arrival times of photons is understood. At low numbers of hits used in the fit, the error on the hit time residual is underestimated.

Thus, a selection based on the χ^2 probability of the fit is less effective at low hit numbers. From the simulation it is found that the deterioration of the fit quality is due to both electro-magnetic showers and multiple muons from a cosmic ray interaction arriving simultaneously.

The rate of atmospheric muons as a function of vertical depth in water is calculated from the data of Line 1. Different zenith angle bins are converted to different depths. An acceptance correction is applied which is calculated from simulation. The depth range is limited by the divergence of the correction factor. This divergence is a result of the bias towards horizontal directions due to electro-magnetic showers. The measured depth-intensity relation agrees with that of other experiments within the uncertainties on the angular acceptance.

A search for neutrino candidates is presented. Background from atmospheric muon events that are reconstructed as upward is suppressed by requiring an increasing number of hits in the reconstruction. This search resulted in one neutrino candidate measured with Line 1 having 10 hits. This is consistent with the predictions.

The final part of the this thesis investigates the new track reconstruction algorithm for a full detector using simulation. Three main quantities are used to suppress the background events that are falsely reconstructed as upward going. These quantities are available through the newly developed reconstruction algorithm. In this study, several levels of random background are considered. The background from atmospheric muons is reduced to the same level of about 1 event per day for all levels of background. The numbers of remaining atmospheric neutrinos are about 10, 6 and 5 at background rates of 60 kHz, 120 kHz and 240 kHz, respectively.

Before this work, estimates of the effect of the backgrounds on the performance of the Antares detector were done with the old angular acceptance. This led to an underestimate of the backgrounds due to atmospheric muons and neutrinos. The predicted trigger rates due to atmospheric muons are about a factor 2 higher using the current parameterisation.

The length of the track is shown to be a good measure of the quality of the track in terms of angular resolution. The length is defined by the maximum distance between two hits, measured along the track. Only hits that are selected by the causality relation are considered to suppress background hits. When considering neutrino events, the angular resolution increases with track length. The maximum track length is limited by the dimensions of the detector. At this maximum value, the median angular residual is less than 0.1 degrees. Atmospheric muons that are reconstructed as going upward, show a particular distribution of track lengths. In this distribution, inter-line distances can clearly be seen. This is caused by the large contribution of tracks that are reconstructed with a bias

to horizontal directions. This bias is due to electro-magnetic showers along the tracks. There is an excess at low track lengths compared to neutrino events. By requiring at least 120 m of track length, at least 40 % of this background can be rejected.

The scanning of the solid angle leads in general to a number of possible solutions, from which one is selected. If the result of the reconstruction is an upward going track, and the collection of remaining solutions contains a downward going solution, they are compared. In case of an atmospheric muon event, the likelihood per degree of freedom for the upward and (best) downward going solutions are numerically close. By requiring a minimum difference in likelihood per degree of freedom, the number of falsely upward going reconstructed atmospheric muons can be reduced by 58 to 78 %, depending on random background rate. The efficiency for the detection of neutrinos drops by no more than 14 %. The final cut is based on the value of the likelihood per degree of freedom, combined with the number of starting directions that converged to the final solution.

With the cuts applied, the performance of the detector can be evaluated. The performance is compared to the performance using the standard reconstruction method and quality cuts. The standard cuts have been re-evaluated to take into account the trigger and new parameterisation of the angular acceptance. The angular resolution is described by the median of the distribution of the residuals on the angle. For a random background rate of 60 kHz, the resolution is about 0.26 degrees, assuming a flux proportional to E_ν^{-2} (E_ν is the neutrino energy). This is the same as found for the standard reconstruction. This is expected as the resolution is limited by the detector geometry and the width of the probability density of the hit time residuals. This width remained unchanged. The resolution as a function of energy, after applying the cuts, is found to be independent of background rate. The efficiency of the Antares detector can be expressed by the effective area for neutrinos, which is the ratio of the rate of detected events over the incident flux of neutrinos at Earth. The effective area at a background rate of 60 kHz is improved above 50 TeV and below 4 TeV. At 10 PeV, the improvement reaches about a factor 2 and at 100 GeV about 40 %. While an increase in efficiency is achieved, there is still room for improvement. The combined reconstruction of muon tracks and electro-magnetic showers occurring along the track should be pursued.

Bibliography

[1] The ANTARES Collaboration. Technical design report of the antares 0.1 km^2 project. Technical Report Version 1.0, July 2001.

[2] I. A. Belolaptikov et al. The Baikal underwater neutrino telescope: Design, performance, and first results. *Astropart. Phys.*, 7:263–282, 1997.

[3] E. Andres et al. The AMANDA neutrino telescope: Principle of operation and first results. *Astropart. Phys.*, 13:1–20, 2000.

[4] J. Ahrens et al. IceCube: The next generation neutrino telescope at the South Pole. *Nucl. Phys. Proc. Suppl.*, 118:388–395, 2003.

[5] K. Hirata et al. Observation of a Neutrino Burst from the Supernova SN 1987a. *Phys. Rev. Lett.*, 58:1490–1493, 1987.

[6] R. M. Bionta et al. Observation of a Neutrino Burst in Coincidence with Supernova SN 1987a in the Large Magellanic Cloud. *Phys. Rev. Lett.*, 58:1494, 1987.

[7] A. Cho. ASTROPHYSICS: Universe's Highest-Energy Particles Traced Back to Other Galaxies. *Science*, 318(5852):896–897, 2007.

[8] K. Greisen. End to the cosmic ray spectrum? *Phys. Rev. Lett.*, 16:748–750, 1966.

[9] F. Halzen and D. Hooper. High-energy neutrino astronomy: The cosmic ray connection. *Rept. Prog. Phys.*, 65:1025–1078, 2002.

[10] K. Zuber. *Neutrino physics*. Bristol, UK: IOP (2004) 438 p.

[11] T. Antoni et al. KASCADE measurements of energy spectra for elemental groups of cosmic rays: Results and open problems. *Astropart. Phys.*, 24:1–25, 2005.

[12] J. R. Hoerandel. On the knee in the energy spectrum of cosmic rays. *Astropart. Phys.*, 19:193–220, 2003.

[13] M. S. Longair. *High-energy astrophysics. Vol. 2: Stars, the galaxy and the interstellar medium*. Cambridge, UK: Univ. Pr. (1994) 393 p.

[14] W. M. Yao et al. Review of particle physics. *J. Phys.*, G33:1–1232, 2006.

[15] R. J. Protheroe. Origin and propagation of the highest energy cosmic rays. 1996. astro-ph/9612212.

[16] A. Kouchner. *Possiblité d'observation, par le télescope Antares de neutrinos de haute énergie associés aux sursauts gamma et validation des techniques de détection à l'aide d'un prototype*. PhD thesis, Universite Paris VII, 2001.

[17] http://cossc.gsfc.nasa.gov/docs/cgro/.

[18] G. Ingelman and M. Thunman. Particle production in the interstellar medium. 1996. hep-ph/9604286.

[19] D. Allard et al. Cosmogenic neutrinos from the propagation of ultra high energy nuclei. *JCAP*, 0609:005, 2006.

[20] W. Baade and F. Zwicky. Remarks on super-novae and cosmic rays. *Physical Review*, 46:76, 1934.

[21] F. Aharonian et al. A detailed spectral and morphological study of the gamma- ray supernova remnant RX J1713.7-3946 with HESS. *Astron. Astrophys.*, 449:223–242, 2006.

[22] F. Aharonian. Primary particle acceleration above 100-TeV in the shell- type supernova remnant RX J1713.7-3946 with deep HESS observations. *Astron. Astrophys.*, 464:235–243, 2007.

[23] J. Hjorth et al. A very energetic supernova associated with the gamma-ray burst of 29 march 2003. *Nature.*, 423:847–850, 2003.

[24] P. Meszaros and M. J. Rees. Relativistic fireballs and their impact on external matter - models for cosmological gamma-ray bursts. *Astrophys. J.*, 405:278, 1993.

[25] M. J. Rees and P. Meszaros. Unsteady outflow models for cosmological gamma-ray bursts. *Astrophys. J.*, 430:L93–L96, 1994.

[26] F. Aharonian et al. Discovery of very high energy gamma-rays associated with an X-ray binary. *Science*, 309:746–749, 2005.

[27] J. Albert et al. Variable very high energy gamma-ray emission from the microquasar LS I +61 303. *Science*, 312:1771–1773, 2006.

[28] F. A. Aharonian, L. A. Anchordoqui, Dmitry Khangulyan, and Teresa Montaruli. Microquasar LS 5039: A TeV gamma-ray emitter and a potential TeV neutrino source. *J. Phys. Conf. Ser.*, 39:408–415, 2006.

[29] G. E. Romero, H. R. Christiansen, and M. Orellana. Hadronic high-energy gamma-ray emission from the microquasar LS I +61 303. *Astrophys. J.*, 632:1093–1098, 2005.

[30] D. Horns, F. Aharonian, A. I. D. Hoffmann, and A. Santangelo. Nucleonic gamma-ray production in Pulsar Wind Nebulae. *Astrophys. Space Sci.*, 309:189–195, 2007.

[31] G. Lim. Indirect search for Dark Matter with the ANTARES neutrino telescope. 2007. arXiv:0710.3685 [astro-ph],To appear in the proceedings of 15th International Conference on Supersymmetry and the Unification of Fundamental Interactions (SUSY07), Karlsruhe, Germany, 26 Jul - 1 Aug 2007.

[32] F. Halzen and Alan D. Martin. Quarks and leptons: An introductory course in modern particle physics. New York, Usa: Wiley (1984) 396p.

[33] J. Pumplin et al. New generation of parton distributions with uncertainties from global QCD analysis. *JHEP*, 07:012, 2002.

[34] B.D. Hartmann. *Reconstruction of Neutrino-Induced Hadronic and Electromagnetic Showers with the ANTARES experiment*. PhD thesis, Friedrich-Alexander-Universität Erlangen-Nürnberg, 2006.

[35] J.D. Jackson. *Classical Electrodynamics*. John Wiley and Sons,Inc, 1998.

[36] J. Brunner. The Refraction Index at the ANTARES Site. October 2000. ANTARES-SITE-2000-001.

[37] J. A. Aguilar et al. Transmission of light in deep sea water at the site of the antares neutrino telescope. *Astropart. Phys.*, 23:131–155, 2005.

[38] L. A. Kuzmichev. On the velocity of light signals in the deep underwater neutrino experiments. *Nucl. Instrum. Meth.*, A482:304–306, 2002.

[39] D. Bailey. *Monte Carlo tools and analysis methods for understanding the ANTARES experiment and predicting its sensitivity to dark matter*. PhD thesis, Wolfson College, Oxford, 2002.

[40] P. Amram et al. The ANTARES optical module. *Nucl. Instrum. Meth.*, A484:369–383, 2002.

[41] Photonis. *Photomultiplier tubes, principles and applications*. Photonis, 2002.

[42] P.M.Kooijman. On the angular acceptance of the optical module. March 2007. ANTARES-PHYS-2007-002.

[43] Copyright IFREMER.

[44] J. A. Aguilar et al. The data acquisition system for the ANTARES neutrino telescope. *Nucl. Instrum. Meth.*, A570:107–116, 2007.

[45] F. Feinstein. The analogue ring sampler: A front-end chip for antares. *Nucl. Instrum. Meth.*, A504:258–261, 2003.

[46] P. J. Lucas. An object-oriented language system for implementing concurrent, hierarchical, finite state machines. Technical Report UIUCDCS-R-94-1868, University of Illinois at Urbana-Champaign, Urbana, Illinois, 1994.

[47] M.C. Bouwhuis. *Detection of neutrinos from gamma-ray bursts*. PhD thesis, Universiteit van Amsterdam, 2005.

[48] R. Gurin and A. Maslennikov. Controlhost: Distributed data handling package. Technical report, CASPUR Inter-University Computing Consortium Rome, 1995.

[49] R. Brun and F. Rademakers. ROOT: An object oriented data analysis framework. *Nucl. Instrum. Meth.*, A389:81–86, 1997.

[50] M. Ageron et al. The ANTARES optical beacon system. *Nucl. Instrum. Meth.*, A578:498–509, 2007.

[51] J.Brunner. Simulation of ^{40}K signals. June 1999. ANTARES-SITE-1999-002.

[52] D. Zaborov. Coincidence rate of potassium-40 seen with MILOM. February 2006. ANTARES-PHYS-2006-001.

[53] J. A. Aguilar et al. First results of the instrumentation line for the deep-sea antares neutrino telescope. *Astropart. Phys.*, 26:314–324, 2006.

[54] P. Amram et al. Background light in potential sites for the ANTARES undersea neutrino telescope. *Astropart. Phys.*, 13:127–136, 2000.

[55] G. de Vries-Uiterweerd. *Signal and background in the underwater neutrino telescope ANTARES*. PhD thesis, Universiteit Utrecht, 2007.

[56] B.A.P. van Rens. *Detection of Magnetic Monopoles below the Cherenkov Limit*. PhD thesis, Universiteit van Amsterdam, 2006.

[57] W.J. Metzger. *Statistical methods in data analysis*. Katholieke Universiteit Nijmegen, Nijmegen, The Netherlands, 2001. HEN-343.

[58] W.H. Press, S.A. Teukolsky, W.T. Vetterling, and B.P. Flannery. *Numerical recipes in C++*. Cambridge University Press, 2003.

[59] G. Carminati, A. Margiotta, and M. Spurio. MUPAGE user guide. May 2007. ANTARES-SOFT-2007-004.

[60] Y. Becherini, A. Margiotta, M. Sioli, and M. Spurio. A parameterisation of single and multiple muons in the deep water or ice. *Astropart. Phys.*, 25:1–13, 2006.

[61] C. Forti et al. Simulation of atmospheric cascades and deep underground muons. *Phys. Rev.*, D42:3668–3689, 1990.

[62] G. Battistoni, M. Carboni, C. Forti, and J. Ranft. Release of a new version (V.07-1) of the HEMAS-DPM Monte Carlo: Description and user manual. INFN-AE-99-07.

[63] J. Ranft. Dual parton model at cosmic ray energies. *Phys. Rev. D*, 51(1):64–84, Jan 1995.

[64] P. Antonioli, C. Ghetti, E. V. Korolkova, V. A. Kudryavtsev, and G. Sartorelli. A three-dimensional code for muon propagation through the rock: Music. *Astropart. Phys.*, 7:357–368, 1997.

[65] D. Bailey. Genhen v5r1 : Software Documentation. 2002. ANTARES-SOFT-2002-004.

[66] G. Ingelman, A. Edin, and J. Rathsman. Lepto 6.5 - a monte carlo generator for deep inelastic lepton-nucleon scattering. *Comput. Phys. Commun.*, 101:108–134, 1997.

[67] T. Sjostrand. High-energy physics event generation with PYTHIA 5.7 and JETSET 7.4. *Comput. Phys. Commun.*, 82:74–90, 1994.

[68] V. Agrawal, T. K. Gaisser, Paolo Lipari, and Todor Stanev. Atmospheric neutrino flux above 1 GeV. *Phys. Rev.*, D53:1314–1323, 1996.

[69] P. Gondolo, G. Ingelman, and M. Thunman. Charm production and high energy atmospheric muon and neutrino fluxes. *Astropart. Phys.*, 5:309–332, 1996.

[70] Application Software Group. Geant, detector description and simulation tool. 1993. CERN Program Library Long Writeup W5013.

[71] J.Brunner. Geasim. March 2000. http://antares.in2p3.fr/internal/software/geasim.html.

[72] M. de Jong. The ANTARES Trigger Software. May 2005. ANTARES-SOFT-2005-005.

[73] Y. Becherini, N. Cottini, and T. Stolarczyk. Offline reconstruction and analysis software. October 2006. ANTARES-SOFT-2006-003.

[74] A.J. Heijboer. *Track Reconstruction and Point Source Searches with ANTARES*. PhD thesis, Universiteit van Amsterdam, 2004.

[75] E. Carmona. *Study of the event reconstruction and expected performances for point-like sources of the future Antares neutrino telescope*. PhD thesis, Universitat de València - València, Spain, 2003.

[76] F. James. *CERN Program Library Long Writeup, MINUIT*, D506 edition, 1994.

[77] M. de Jong. Partial linearisation of the track fit problem. January 2007. ANTARES-SOFT-2007-001.

[78] Th. Stolarczyk and A. Romeyer. Reconstruction algorithms : a handbook for developers. January 2001. ANTARES-SOFT-2001-001.

[79] T. K. Gaisser. *Cosmic rays and particle physics*. Cambridge, UK: Univ. Pr. (1990) 279 p.

Samenvatting

Sterren kijken is niet iets nieuws. Sterren, oftewel de grote verscheidenheid aan processen en objecten in het heelal, worden sinds mensenheugenis bestudeerd aan de hand van het licht dat ze uitzenden. Echter, de verschillende kosmische processen zenden waarschijnlijk meer uit dan alleen fotonen (zichtbaar licht of andere golflengtes van electro-magnetische straling). De belangrijkste aanwijzing hiervoor is de waarneming van zogenaamde kosmische stralen. In het begin van de 20^e eeuw werd ontdekt dat de aarde bestookt wordt met geladen deeltjes van buitenaf. De kosmische stralen blijken ongelooflijk hoge energieën te kunnen hebben, tot wel 10^{20} eV. Er zijn veel vragen omtrent de kosmische stralen. De exacte samenstelling is onbekend, en bovenal hun oorsprong. Doordat de kosmische stralen elektrisch geladen zijn, worden ze afgebogen door (extra-)galactische magnetische velden. Hierdoor reizen ze niet langs een rechte lijn naar ons toe en gaat de informatie over hun oorsprong verloren, behalve bij de allerhoogste energieën. Fotonen behouden wel hun richting. Echter zij gaan reacties aan met de in het heelal aanwezige microgolf, radio en infra-rood achtergrond. Hierdoor zijn ze van beperkte waarde in het achterhalen van de oorsprong van hoog energetische kosmische stralen. Interacties van hoog energetische protonen kunnen leiden tot de productie van neutrinos, zo ook op de plaatsen waar kosmische stralen hun energie krijgen. Neutrinos zijn neutrale deeltjes welke alleen wisselwerken via de zwakke kernkracht met een zeer kleine werkzame doorsnede. Door deze eigenschappen worden neutrinos noch afgebogen door magnetische velden, noch makkelijk geabsorbeerd door de materie in het heelal. Kortom, neutrinos zijn goede sondes om astrofysische processen te bestuderen.

De Antares collaboratie bouwt een telescoop voor de waarneming van neutrinos. Om deze neutrinos te detecteren moeten ze een reactie aangaan. Wanneer een neutrino een interactie aangaat, kunnen er deeltjes geproduceerd worden die licht uitzenden in een transparant medium. Hiervoor is zeewater bij uitstek geschikt, omdat het mogelijk is een groot volume van dit doorzichtige medium met licht-gevoelige detectie apparatuur uit te rusten. Een groot volume is nodig omdat neutrinos een lage kans hebben om een reactie aan te gaan. De Antares telescoop richt zich in het bijzonder op neutrinos van het muon type. Wanneer een muon-neutrino wisselwerkt met materie, kan er een muon ontstaan. Bij hoge energieën, kan het muon lange afstanden door rots of zeewater afleggen. Het

muon, een geladen deeltje, zal licht uitzenden wanneer het zich sneller voortbeweegt dan de lichtsnelheid in het medium. Dit zogeheten *Cherenkov* licht kan zich ver voortplanten in het water voordat het geabsorbeerd wordt. De Antares telescoop maakt van deze eigenschappen gebruik en bestaat uit een rooster van licht-gevoelige fotomultiplicatoren in het zeewater om dit licht te detecteren. De volledige detector zal bestaan uit 12 verticale lijnen waarvan ongeveer 350 meter is uitgerust met fotomultiplicatoren. Op elke lijn bevindt zich om de 14.5 meter een verdieping met 3 fotomultiplicatoren, elk gehuisd in een drukbestendige glazen bol. Een complete lijn heeft 25 van deze verdiepingen. De twaalf lijnen zijn in totaal dus behangen met 900 fotomultiplicatoren. De detector bevindt zich op ongeveer 2.5 kilometer diepte in de Middellandse Zee, 40 km uit de kust van Toulon, Frankrijk. Het grondoppervlak van de detector beslaat ongeveer 180 bij 180 meter.

Het licht van een muon dat is geregistreerd door de fotomultiplicatoren verschaft informatie waaruit de richting van het muon kan worden bepaald. De richting van een muon is sterk gecorreleerd met dat van het oorspronkelijke neutrino. Dus wanneer de richting van het muon bepaald is, is de richting van het neutrino ook bekend. Dit is het principe van de neutrino telescoop. Eén van de onderwerpen beschreven in dit proefschrift is een methode om de richting van muonen, die door de detector passeren, te bepalen uit het gemeten licht. Dit proces wordt *muon spoor reconstructie* genoemd.

Helaas zijn muonen uit interacties van kosmische neutrinos is niet de enige bron van licht in de diepzee. Een fractie van de muonen die gecreëerd worden in de interacties van kosmische stralen met atomen in de atmosfeer bereikt de detector. Deze *atmosferische* muonen vormen een belangrijke achtergrond voor de waarneming van muonen geproduceerd door interacties van *kosmische* neutrinos. Aangezien muonen niet door de aarde kunnen komen, worden atmosferische muonen alleen van boven verwacht. Zodoende kunnen ze onderscheiden worden van neutrinos. Hiervoor is het wel nodig dat ze wel herkend worden als neergaand. Door verscheidene verstorende invloeden is het namelijk ook mogelijk dat een neergaand muon ten onrechte voor opgaand wordt aangezien. In de interacties van kosmische stralen in de atmosfeer worden ook neutrinos gemaakt. Gebeurtenissen veroorzaakt door deze *atmosferische* neutrinos kunnen niet van gebeurtenissen door kosmische neutrinos onderscheiden worden en vormen een achtergrond bij het zoeken naar kosmische neutrinos. Daarnaast zorgt de (natuurlijke) aanwezigheid van radioactief kalium en biologische activiteit in het zeewater voor een andere achtergrond. Zowel het verval van het kalium als de biologische activiteit zorgen ervoor dat er continu licht door de fotomultiplicatoren wordt gedetecteerd dat gescheiden moet worden van het licht van muonen. Daarvoor wordt een filter gebruikt dat volledig in software is geimplementeerd. Verder kan dit licht het signaal van muonen vervuilen. Hier moet tijdens de muon spoor reconstructie rekening mee worden gehouden.

Het reconstrueren van een muon spoor wordt niet alleen bemoeilijkt door het

achtergrond licht. Naast het continu uitgezonden Cherenkov licht worden er ook nog via andere processen fotonen uitgezonden. Een hoog-energetisch muon ($>$ 1 TeV) verliest een deel van zijn energie door stochastische processen. Dit manifesteert zich onder andere door electro-magnetische cascades. Deze cascades lijken op puntbronnen van licht langs het spoor. Door de stochastische aard van de cascades is het moeilijk deze in rekening te nemen. Het reconstrueren van muon sporen kan op verschillende manieren worden aangepakt. Een methode is om de voortbeweging van muonen zo volledig mogelijk te modelleren. Hierbij worden cascades en bijvoorbeeld de eigenschappen van de detector en het medium in rekening gebracht. Een nadeel hiervan is de afhankelijkheid van de nauwkeurigheid van het model. Een andere methode is om het muon te benaderen door een deeltje waarvan alleen direct Cherenkov licht wordt gemeten. In dit geval is het noodzakelijk dat er een selectie plaatsvindt van de geregistreerde fotonen die waarschijnlijk direct van het muon afkomstig zijn. Deze methode is minimaal afhankelijk van de parameters die de detector respons beschrijven. Zodoende is deze methode in het bijzonder geschikt voor de beginperiode van de telescoop. De spoor reconstructie methode beschreven in dit proefschrift combineert de twee verschillende manieren van aanpak.

Op 2 maart 2006 werd de eerste lijn van de Antares detector aangesloten. Dit luidde het begin in van neutrino astronomie met de Antares telescoop. Het muon spoor reconstructie algorithme zoals beschreven in dit proefschrift, werd gebruikt om de eerste muon sporen te reconstrueren. Inmiddels zijn er al 10 lijnen geïnstalleerd. Eén van de onderwerpen in dit proefschrift is een uitgebreide analyse van de data vergaard in de periode dat de eerste lijn alleen opereerde. Uit deze periode werd een totaal van 9.3 dagen aan gegevens geselecteerd, waarin 75621 gebeurtenissen waren gevonden. Muon spoor reconstructie en analyse met een enkele lijn heeft zijn eigen beperkingen. Door de rotatie-symmetrie rond de lijn is het niet mogelijk om de azimuth hoek te bepalen. Ook kan er een ambiguiteit optreden wanneer slechts een deel van het Cherenkov licht van een muon wordt gezien. Dit leidt tot zogenaamde 'spook' oplossingen, die twee keer de Cherenkov hoek (de hoek waaronder het Cherenkov licht wordt uitgezonden) van de juiste oplossing verschillen. Een analyse met een enkele lijn is in het bijzonder gevoelig voor de verstorende werking van electro-magnetische cascades die langs een muon spoor kunnen optreden. Deze cascades kunnen gezien worden als puntbronnen van licht en lijken daarmee op muonen die zich horizontaal langs de lijn voortbewegen. Een aantal resultaten worden gepresenteerd. De simulatie blijkt de aankomsttijden van fotonen goed te beschrijven. De telsnelheid van muonen als functie van de gereconstrueerde zenith hoek is bepaald. Deze verdeling komt binnen de onzekerheden over een met de verdeling zoals verwacht van simulatie. De voornaamste onzekerheid komt van relatieve acceptantie van de fotomultiplicatoren als functie van de hoek van inval van de fotonen. Na bepaling van de acceptantie van de detector, kan de afhankelijkheid van de muon intensiteit van de diepte in water bepaald worden.

Deze komt overeen met gepubliceerde resultaten van andere experimenten. De nauwkeurigheid waarmee de richting van muon bepaald kan worden is bestudeerd met gebruik van die gegevens, welke voornamelijk toe te schrijven zijn aan atmosferische muonen. De bepaling is gedaan door de lijn op te delen in subdetectoren. Het blijkt dat de nauwkeurigheid waarmee de zenith hoek kan worden bepaald beter kan zijn dan 0.5° voor een enkele lijn. Om neutrinos te vinden worden alleen gebeurtenissen gebruikt waarvan is bepaald dat het muon opwaarts beweegt. De voornaamste achtergrond komt van atmosferische muonen die foutief worden gereconstrueerd als omhoog gaand. Door onder andere een eis te stellen op het minimale aantal verdiepingen van de lijn waarop fotonen zijn geregistreerd, kan deze achtergrond onderdrukt worden. De zoektocht resulteert in één neutrino, wat overeenkomt met de voorspelling door middel van simulatie.

Het laatste onderwerp van dit proefschrift betreft een studie van de prestaties van de Antares telescoop wanneer deze compleet is. Bij deze studie is gebruik gemaakt van de in dit proefschrift beschreven muon spoor reconstructie. Deze studie is gedaan aan de hand van simulaties. Een aspect van de studie is het onderdrukken van de achtergronden van voornamelijk verkeerd gereconstrueerde atmosferische muonen. Om deze achtergrond te onderdrukken wordt gebruik gemaakt van snedes op verschillende parameters, die zijn gebaseerd op de geschatte lengte van het muon spoor en de waarschijnlijkheids waarde die door de spoor reconstructie methode berekend wordt. De waardes van de snedes hangen af van de telsnelheid veroorzaakt door achtergrond. De achtergrond van verkeerd gereconstrueerde atmosferische muonen kan gereduceerd worden tot ongeveer 1 per dag (vóór de snedes worden per seconde ongeveer 3 atmosferische muonen gereconstrueerd, waarvan ongeveer 5 % onjuist als opgaand). Twee grootheden welke belangrijk zijn voor neutrino astronomie zijn bestudeerd, deze zijn het oplossend vermogen en de efficientie van de detector. De hoekresolutie wordt uitgedrukt in de mediaan van de verdeling van de hoek residuen. Bij een telsnelheid van 60 kHz, wat een realistische waarde is, door de achtergrond, is de hoekresolutie 0.26°. De hoekresolutie als functie van neutrino-energie is onafhankelijk van de achtergrond-telsnelheid. De effectiviteit van de detector om neutrinos te detecteren kan uitgedrukt worden door het *effectieve oppervlak* voor neutrinos. Dit is gedefiniëerd als de grootte van een oppervlak dat honderd procent efficient is voor de detectie van neutrinos. De in dit proefschrift ontwikkelde muon spoor reconstructie, samen met de gekozen snedes om de achtergrond te onderdrukken leiden tot een verbetering van het effectieve oppervlak van de Antares detector. Bij een achtergrond telsnelheid van 60 kHz is de verbetering bijna een factor 2 bij 10 TeV neutrino energie en 40 % bij 100 GeV neutrino energie.

Dankwoord

Tsja, en dan is het af... of toch ook niet helemaal. Dit proefschrift zou namelijk niet compleet zijn zonder iedereen, collega's, familie en vrienden, te bedanken die aan de totstandkoming ervan op zijn of haar manier, vaak zonder het te weten, hebben bijgedragen. Een aantal noem ik in het bijzonder.

Maarten, jou zou ik graag als eerst en het meest willen bedanken. Ik had me geen betere begeleiding kunnen wensen. Jouw vele ideeën, briljante inzichten en hulp zijn absoluut onmisbaar geweest voor het werk en dit boekje. Je aanstekelijke enthousiasme, betrokkenheid en aanmoediging zijn belangrijk geweest voor de motivatie en het plezier dat ik er al die tijd in had. Ik heb heel veel van je geleerd, en je zag problemen altijd al zitten voordat ik ze helemaal uitgelegd had. Ik ben blij dat je idee voor een feedback systeem voor de begeleiding van een promovendus (nog) geen werkelijkheid is. Het zou me namelijk een aardige duit gekost hebben !

Paul, ik ben heel blij dat je de taak van promotor hebt willen overnemen. Je wijsheid, kennis over bijna alles, inzichten en de bedachtzaamheid waarmee je ze uit, hebben niet alleen dit werk beter gemaakt, ze hebben me ook veelvuldig vermaakt.

During my time in the Antares experiment, I was lucky to experience a working detector. It has been an enormous thrill to actually see the first data coming from the sea ! I would like to thank the members of the Antares collaboration for their (continued) efforts in making this happen and for their help. I would like to thank Jürgen for answering all the questions I put on the mail.

I would like to thank the members of my reading-committee for their useful comments.

De NIKHEF-Antares groep is in de jaren wat uitgedijt, en zoals het gaat, mensen komen en sommigen gaan weg. Zowel de 'nieuwe' lichting : Gordon (Shiftmeister-G, the master himself !), Guus (chocolate-chip koekjes), Salvatore (chocolates), Eleonora (the italian chef), Andrea, als de 'oude' : Aart, Bram (fibre-tray-assembly-line) en Mieke (jammer dat de konijntjes ook meegingen toen je van kamer verhuisde) wil ik bedanken voor de goede atmosfeer, hulp en vriendschap. Aart, jou wil ik speciaal bedanken omdat je me als student en beginnend aio goed op weg heb geholpen door altijd bereid te zijn m'n vragen te beantwoorden. Claudine, my room-mate for the largest part, though I was not always quite sure if you were 'hungry' or 'angry', thanks for your good company ! I wish

you all the 'good courage' with finishing your own thesis. The (relative) newcomers, Dimitri(o)s and Ana, I wish you good luck in this great group. Dat geldt natuurlijk ook voor Jos en Patrick. Els, je begeleiding bij mijn doctoraal-scriptie was een belangrijk begin en bedankt voor het idee om mee te doen aan de UvA scriptie prijs. Gerard, ook bedankt voor het in goede banen leiden van soms wat praktischere zaken, adviezen en aanmoediging. Jos Engelen wil ik bedanken omdat hij me als student bij Antares betrok en als promovendus, naar later bleek tijdelijk, aannam. Henk, bedankt voor je hulp met die fotobuizen. Verder wil ik de groep aio's,oio's, post-docs en anderen die NIKHEF zo een geweldige plek maken daarvoor bedanken. Patrick en Gabriel, bedankt voor de last-minute tips.

Ook buiten het NIKHEF hebben vrienden en familie, elk op hun eigen manier, bijgedragen. Vooral in de laatste periode heb ik aan jullie toch iets minder tijd kunnen besteden dan ik gewild had. Maar ik ben jullie buitengewoon dankbaar voor alle warmte, vriendschap, interesse en afleiding die jullie me geboden hebben. In het bijzonder wil ik Stefan en Wouter, mijn paranimfen (of : para-troopers zoals Stefan zegt), bedanken. Dat is nummer twee ! Dank aan Leo en Daniella, Robert en Suzette, Michael en Davinia, Erno, Michiel, Ruben, de leden van UvO en de heren en dame van Heeren 3. Mijn uitgebreide familie en 'schoon' familie wil ik bedanken voor alle interesse en gezellige momenten.

Demelza, bedankt voor alle dingen die het leuk maken een grote broer te zijn !

Pap en Mam, het is niet mogelijk uit te drukken hoeveel ik aan jullie te danken heb. Bedankt voor het scheppen van de mogelijkheden om mijn eigen weg te vinden, het volledige vertrouwen en een warm thuis.

Mijn jaren bij de Antares groep op het NIKHEF hebben niet alleen dit proefschrift gebracht. Het allermooiste dat ik er aan heb overgehouden, en dat al vrij snel in het begin, is mijn liefste, mijn vriendin Nadja. Je hebt het van het begin tot het eind meegemaakt. Je bijdrage is echt groter dan je denkt en heeft het oneindig leuker gemaakt ! Bedankt !